SEARCHING FOR NEW MILLISECOND PULSARS WITH THE GBT IN FERMI UNASSOCIATED SOURCES

Siraprapa Sanpa-arsa
Khon Kaen, Thailand

B.A. Physics, Kasetsart University, 2009

M.S. Astronomy, University of Virginia, 2011

A Dissertation Presented to the Graduate
Faculty of the University of Virginia
in Candidacy for the Degree of
Doctor of Philosophy

Department of Astronomy

University of Virginia
July 2016

Committee Members:

Prof. Scott M. Ransom
Vanderbilt Prof. Craig Sarazin
VITA Assoc. Prof. Phil Arras
Prof. Brad Cox

Abstract

The launch of the *Fermi* satellite in 2008 revolutionized γ-ray pulsar astronomy by enabling the discovery of many new millisecond pulsars (MSPs). The *Fermi* Pulsar Search Consortium (PSC) has organized hundreds of radio observations of pulsar-like Large Area Telescope (LAT) unassociated sources. Over the past seven years, the PSC has discovered more than 70 new MSPs, compared to the 75 MSPs found in the 25 years prior to *Fermi*. The National Radio Astronomy Observatory's Robert C. Byrd Green Bank Telescope (GBT) has played the key role in the project by discovering almost half (34) of the new MSPs. In this thesis, I present the discovery and analysis of 16 new MSPs, 10 of which were uncovered by me personally. The pulsars were found in GBT searches within the positional error boxes of 266 *Fermi* LAT sources, both at high Galactic latitudes and closer to the Galactic plane. All new pulsars have phase-connected radio timing solutions, and for 12 of them, γ-ray pulsations were detected. Twelve MSPs have Helium white dwarf (He-WD) companions and the other four are in so-called "spider" systems with compact orbits and non-degenerate companions. We investigated the relationship between radio and γ-ray flux densities for all MSPs, confirming that there is almost no correlation between the two. We also investigated the orbital period vs. companion mass relation for MSPs with He-WD companions using a simple Monte Carlo technique, and found that the distribution of binary inclination angles is not random but possibly leans towards lower inclinations. For the four MSPs in compact orbits, we examined flux density variability, as well as their optical light curves. We found that all four MSPs are eclipsing and that two of them exhibit strong diffractive scintillation. Finally, we found optical counterparts for two MSPs, one of which shows ellipsoidal modulations in its light curve, suggesting that the companion is filling its Roche lobe.

Acknowledgements

I owe my deepest gratitude to my advisor, Prof. Scott Ransom. He is not only a rock climber, a socializer or a hyper pulsar-enthusiastic scientist, he is my very first mentor. Without his guidance, encouragement and support, this thesis would not have been complete. I am deeply thankful to my *Fermi* colleagues and collaborators who have been doing incredible science and inspired me to do great science like they do. I would like to express my gratitude to Tyrel Johnson who wrote the γ-ray analysis in Section 2.3.4, 2.4.2, 2.4.3, and provided Figure 2.2 in Chapter 2. Scott Ransom who wrote the joint γ-ray and radio timing and the $P_b - M_c$ relation in Section 2.3.5, 2.5.5 ,and provided Figure 2.7 in Chapter 2. Anna Bilous who wrote the single-pulse search in Section 3.3.3, and provided Figure 3.10 and 3.11 in Chapter 3. Paul Ray who provided Figure 3.7 in Chapter 3. Jules Halpern who provided Figure 3.3, 3.5 and 3.8 in Chapter 3

I would like to thank my second family in UVA and friends who have been with me through the ups and downs in this journey. I love you guys more than words can ever express. Yes, that was very cliché. Lastly, this thesis and my life would not have existed without my family. They give me support, unconditional love and spread their wings to catch me whenever I fall. I could never ask for a better family.

Table of contents

Abstract **ii**

1 Introduction **1**
1.1 Pulsars . . . 1
1.1.1 Pulsar Overview . . . 1
1.1.2 Pulsar properties . . . 4
1.1.3 Millisecond pulsars . . . 9
1.1.4 Pulsar timing . . . 11
1.2 Searching for New Pulsars . . . 19
1.2.1 RFI removal . . . 20
1.2.2 Dispersion Measure trials . . . 21
1.2.3 Periodic Searches . . . 21
1.2.4 Acceleration Search . . . 22
1.2.5 Candidate selection . . . 23
1.2.6 Single-pulse search . . . 23
1.3 *Fermi* Unassociated Sources . . . 25
1.3.1 *Fermi* satellite . . . 25
1.3.2 *Fermi* "Treasure Map" . . . 27
1.3.3 The Pulsar Search Consortium (PSC) . . . 28
1.4 Pulsar Search with the Green Bank Telescope (GBT) . . . 31

2 Discovery of Twelve New Millisecond Pulsars in *Fermi* LAT Sources with the Green Bank Telescope **33**
2.1 Introduction . . . 33
2.2 Source Selection . . . 35
2.3 Observation and Data Analysis . . . 38
2.3.1 Observation Method and Sensitivity . . . 38
2.3.2 Pulsar Search Method . . . 39
2.3.3 Pulsar Timing . . . 42
2.3.4 LAT Data Analysis . . . 45
2.3.5 Joint γ-ray and Radio Timing . . . 46
2.4 Results . . . 48

2.4.1 The New MSPs . . . 48
2.4.2 Radio and Gamma-ray Light Curves . . . 53
2.4.3 Gamma-ray Pulsations . . . 56
2.5 Discussion . . . 59
2.5.1 Radio and γ-ray Flux Densities . . . 59
2.5.2 Galactic Plane Searches with S-band . . . 60
2.5.3 Single-Pulse Searches . . . 62
2.5.4 LAT γ-ray Detection Threshold . . . 62
2.5.5 Orbital Period and Companion Mass Relation . . . 65
2.6 Conclusion . . . 70

3 Four New Pulsars in Tight Orbits 73
3.1 "Spider" Pulsars . . . 73
3.2 Observation and data analysis . . . 75
3.3 Results . . . 77
3.3.1 Pulsar timing . . . 77
3.3.2 The new MSPs . . . 78
3.3.3 Single-pulse search . . . 81
3.4 Discussion . . . 82
3.4.1 Flux variations . . . 82
3.4.2 Optical, X-ray and γ-ray counterparts . . . 83
3.5 Conclusion . . . 84

4 Conclusions and Future Work 101

5 Appendix: Tables 104

Chapter 1

Introduction

1.1 Pulsars

1.1.1 Pulsar Overview

The prediction of the existence of neutron stars, the smallest and densest stars, had been made before they were actually discovered. In 1934, the two astronomers, Walter Baade and Fritz Zwicky, wrote in Baade & Zwicky (1934) that: "With all reserve we advance the view that a super-nova represents the transition of an ordinary star into a neutron star, consisting mainly of neutrons. Such a star may possess a very small radius and an extremely high density." More than 30 years later, in 1967, graduate student Jocelyn Bell recognized regular fluctuations of a signal from a radio source. Together with her advisor, Antony Hewish, they found that the signals peaked every 1.34 seconds and reappeared once every sidereal day, which suggested a celestial (outside the Solar System) origin. In 1968 they announced that the repeated radio signals likely came from a rotating neutron star, the pulsar B1919+21 (Hewish et al. 1968). See Fig. 1.1.

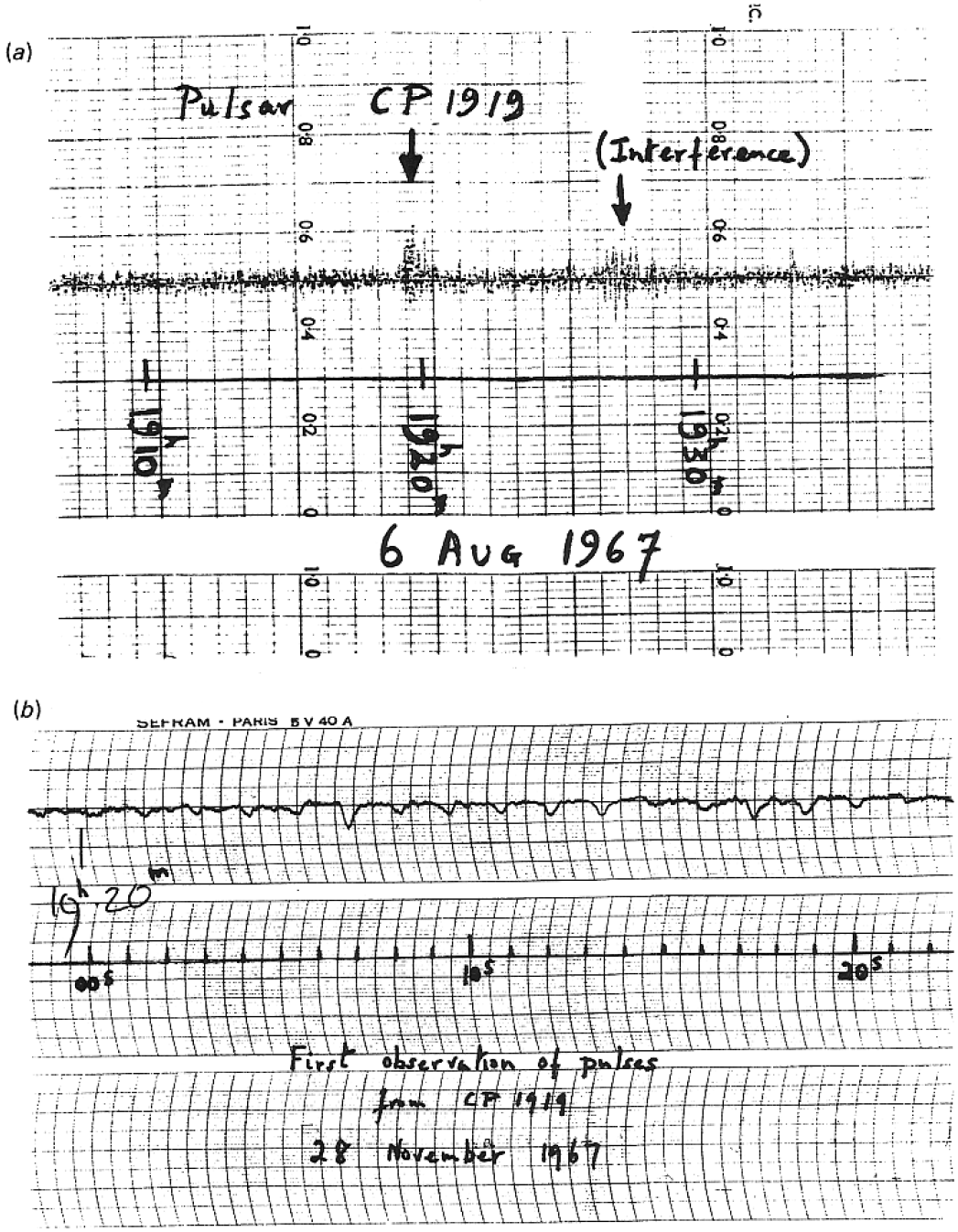

Fig. 1.1.—: The discovery of the first pulsar B1919+21. (a) The radio signals first appeared with the characteristics of radio interference. (b) Fast chart recordings showed repeated individual pulses at every 1.34 s (Hewish et al. 1968).

Pulsars are highly magnetized, rapidly rotating, neutron stars, the final products of the supernovae of massive stars ($\sim$8$-$20 times the mass of our sun, $M_\odot$). As these incredibly dense objects ($\sim$1$-$2 $M_\odot$, but only about 20 km in diameter) rotate, they emit beams of radiation, producing pulses each time the beams sweep across an observer's line of sight, in a type of "light house effect". The precision and stability of pulsar rotations are incredible, due to their density, and they are therefore often called the clocks of the Universe.

In many aspects, pulsars are a "physicist's dream come true" (Lorimer & Kramer 2005). They can be used to study physics under extreme conditions which do not exist on Earth such as theories of gravity in deep gravitational potentials and the exotic solid state and nuclear physics in the interiors ultra-dense neutron stars. Pulsars can furthermore be used to study the gravitational potential and magnetic field of the Galaxy, the interstellar medium (ISM), and binary systems and their often complex evolution. Pulsar timing allows us to precisely measure pulsar spins, astrometric parameters, and the effects of the ISM between the pulsar and the observer. The fast-rotating population, millisecond pulsars (MSPs), however, are much preferred and more useful for pulsar timing than the slow population of normal pulsars. MSP signals can be measured more precisely and they do not exhibit rotational instabilities which are common in normal pulsars. These properties make MSPs much better clocks which are more useful for exotic pulsar timing applications. This thesis deals primarily with MSPs.

1.1.2 Pulsar properties

$P - \dot{P}$ diagram

As a pulsar evolves, its spin period (P) gradually increases with time corresponding to a rate of "spin-down" ($\dot{P}$). This spin-down is a result of its loss of rotational kinetic energy which it emits in electromagnetic radiation and particles. The characteristic age ($\tau \propto P/\dot{P}$), the magnetic field strength ($B \propto \sqrt{P\dot{P}}$) and the rate of loss of rotational kinetic energy or "spin-down luminosity" ($\dot{E} \propto \dot{P}/P^3$) of the pulsar can be determined with only the two observable parameters, P and $\dot{P}$. The "$P - \dot{P}$ diagram" of pulsars shown in Fig. 1.2 therefore provides insight into the spin evolution of neutron stars. Note that P and $\dot{P}$ of a pulsar can be obtained precisely via pulsar timing (see Section 1.1.4).

The $P - \dot{P}$ diagram clearly shows two distinct populations of pulsars: "normal pulsars" ($P \sim 0.5\,\mathrm{s}$ and $\dot{P} \sim 10^{-15}\,\mathrm{s\,s^{-1}}$) and "millisecond pulsars" ($P \sim 30\,\mathrm{ms}$ and $\dot{P} \sim 10^{-20}\,\mathrm{s\,s^{-1}}$). The lines of constant τ, B and $\dot{E}$ are also shown on the $P - \dot{P}$ diagram. A plausible evolutionary track for normal pulsars starts with their birth in supernovae in the middle and upper left region of the diagram. Assuming a constant B, pulsars gradually move down and right along the lines of constant B, crossing the lines of constant age as P increases. On a timescale of $\sim 10^7$ years, either old pulsars' magnetic fields or spin rates are too low to produce radio emission, and they eventually become too faint to detect. However, through the "recycling process", an old (or dead) pulsar in a binary system can be spun-up by accreting mass and angular momentum from its companion and become detectable again. These recycled pulsars are the MSPs in the lower left of the $P - \dot{P}$ diagram.

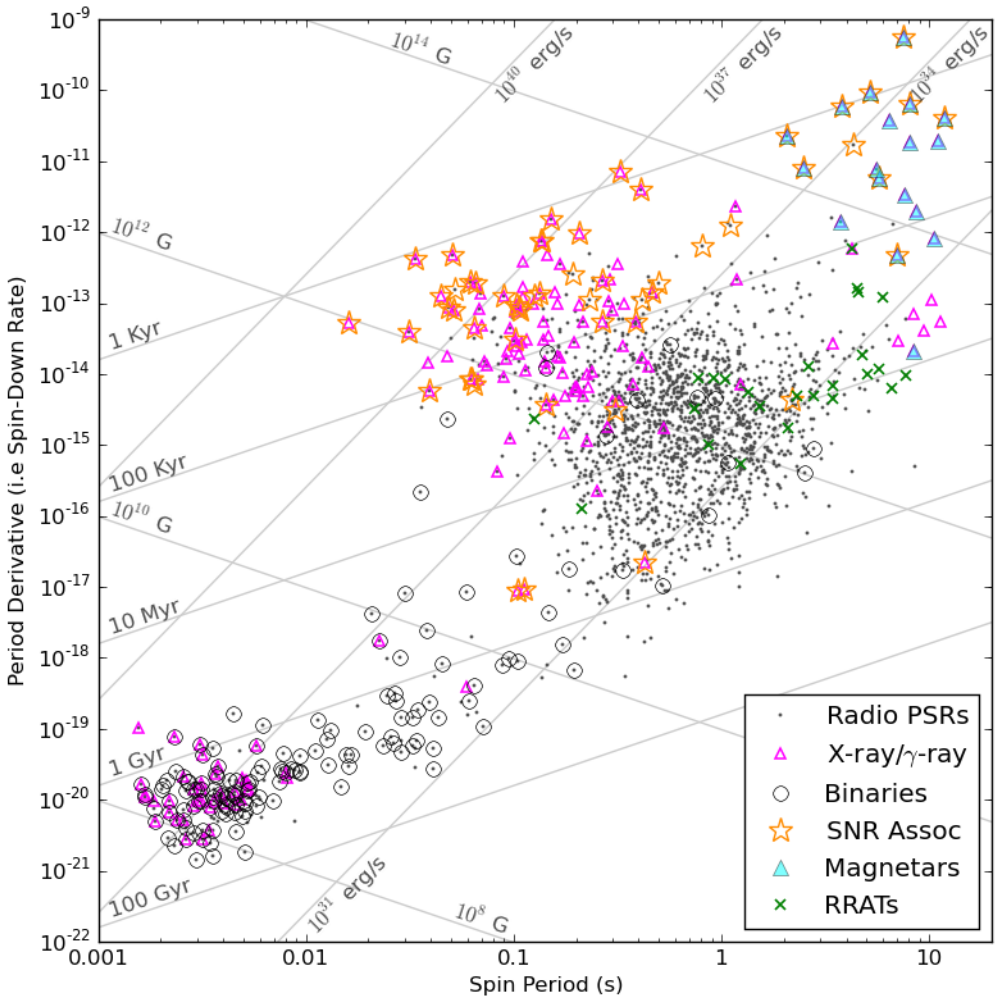

Fig. 1.2.—: The $P - \dot{P}$ diagram of over 2,200 pulsars. The majority of the pulsars, the "normal" pulsars, have spin period more than 0.3 s and appear on the middle right of the diagram. The millisecond pulsars have spin period less than 0.3 s and locate on the bottom left of the diagram. *Image credit: Scott Ransom*

Dispersion measure (DM) and de-dispersion

As radio waves from pulsars travel through the ionized plasma in the interstellar medium (ISM), the radiation experiences a frequency-dependent dispersive effect — pulses at lower frequencies travel through a plasma slower than the ones at higher frequencies. The time delay from the dispersion between two frequencies (Δt) of the radio waves can be described by

$$\left(\frac{\Delta t}{\mathrm{s}}\right) \approx 4.15 \times 10^3 \times \left[\left(\frac{f_1^{-2}}{\mathrm{MHz}}\right) - \left(\frac{f_2^{-2}}{\mathrm{MHz}}\right)\right] \times \left(\frac{\mathrm{DM}}{\mathrm{pc \cdot cm^{-3}}}\right), \tag{1.1}$$

and

$$\mathrm{DM} \equiv \int_0^d n_e \, dl, \tag{1.2}$$

where f is the frequency of the radio wave, DM is the "dispersion measure", d is the distance to the pulsar, and n_e is the electron number density. A known DM can be used to estimate the distance of the pulsar using the model of the electron density distribution in the Galaxy (e.g. NE2001 by Cordes & Lazio 2002).

"Incoherent de-dispersion" is the simplest way to compensate for the dispersion of pulses. The observing frequency band is split into numerous independent frequency channels, and each channel is shifted in time by the delay calculated with Eq. 1.1 using the correct value of DM (See Fig. 1.3). As a result the pulses from each channel are made to arrive at the same time. Most of the observations in this thesis were processed using incoherent de-dispersion.

Magnetic field strength

A core-collapse supernova dramatically amplifies the magnetic field strength (B) in the core of the collapsing star, making that in the resulting neutron star incredibly

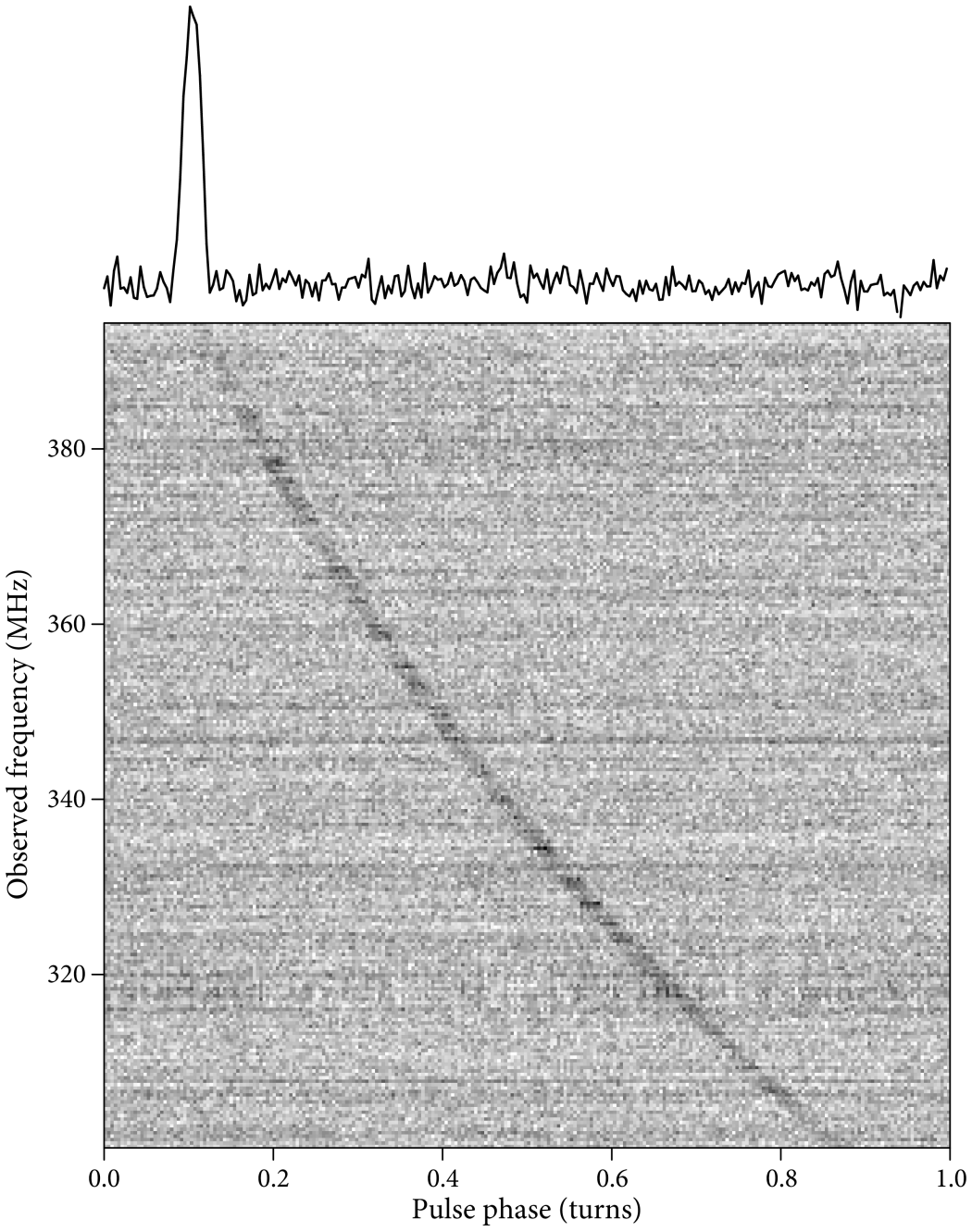

Fig. 1.3.—: The diagram shows pulse dispersion due to the ionized interstellar medium. The grey scale shows dispersive pulse delays of PSR J1400+50. The de-dispersed integrated pulse profile in shown at the top of the diagram. *Image credit: Scott Ransom*

large. From the conservation of magnetic flux ($\Phi \equiv \int \vec{B} \cdot \hat{n}\, da$ where $\hat{n}$ is a unit vector and a is the surface area), a decrease in the radius of a star, for example, by a factor of 10 after collapsing, would decrease the surface area and therefore increase the magnetic strength by a factor of 100. Pulsars therefore have strong dipole magnetic fields.

The surface magnetic field strength (B_s) of a radio pulsar, however, cannot be measured directly, but can be estimated by assuming a neutron star moment of inertia (I) of $10^{45}\,\mathrm{g\,cm^2}$, a radius of 10 km, that the magnetic moment and spin axis are perpendicular, and that the spin-down process is dominated by dipole braking:

$$B_s \simeq 10^{12}\ \mathrm{G}\ \sqrt{\frac{\dot{P}}{10^{-15}} \cdot \frac{P}{\mathrm{s}}}. \tag{1.3}$$

Note that this is the magnetic strength at the equator not at the poles.

Spin-down luminosity

The pulsar spin period decreases with time as a result of the loss of rotational kinetic energy (E_{rot}). The rate of rotational kinetic energy or the "spin-down luminosity" ($\dot{E}$) can be estimated by assuming the canonical, I, of 10^{45} g cm^2

$$\dot{E} \equiv -\frac{\mathrm{d}E_{\mathrm{rot}}}{\mathrm{d}t} = -\frac{\mathrm{d}(I\Omega^2/2)}{\mathrm{d}t}\ \text{, where } \Omega = 2\pi/P, \tag{1.4}$$

and with constants evaluated, and in useful units,

$$\dot{E} \simeq 3.95 \times 10^{31}\ \mathrm{erg\ s^{-1}}\ \left(\frac{\dot{P}}{10^{-15}}\right)\left(\frac{P}{\mathrm{s}}\right)^{-3}. \tag{1.5}$$

Characteristic age

The pulsar age can be approximated with only two observables, P and $\dot{P}$. Under the assumption that magnetic dipole radiation causes the spin-down and that the birth spin period is much smaller than the present one,

$$\tau \equiv \frac{P}{2\dot{P}}, \tag{1.6}$$

where τ is the "characteristic age" of the pulsar.

1.1.3 Millisecond pulsars

Distinct population

Millisecond pulsars (MSPs), those pulsars with spin periods less than $\sim$30 ms, spin much faster and live much longer than the more common "normal" (i.e. $\sim$1-sec) pulsars, and they are thought to have been produced by a more complex evolutionary process. MSPs originate from the interaction between normal (or most likely, long-dead) pulsars and their binary companions. This interaction leads to a transfer of mass and angular momentum which"spins up" (i.e. increases the rotation speed of) the pulsar to many hundreds of rotations per second. In the non-interacting case the luminosity of a pulsar decays as rotational energy is lost, and eventually the pulsar becomes unobservable. However, if the spin-up process takes place after a pulsar has "died", it will rejuvenate the pulsar and cause the pulsar to become a radio emitter once again. The spin-up process is thus often referred to as "recycling".

The recycling process not only changes the spin period of the pulsar, but also its magnetic field strength, and correspondingly, its spin period derivative ($\dot{P}$) and subsequent evolution. The period derivatives of MSPs are smaller by four to five

orders of magnitude than those of normal pulsars, and given the much more rapid spin rates, implies that MSPs live far longer than normal pulsars. The surface magnetic fields of the MSPs are approximately four orders of magnitude smaller than those of most pulsars due to unknown mechanisms during the spin-up process (probably related to field burial by the accreted ionized gas).

Properties of MSP emission

Many studies have shown that the radio emission properties of MSPs and normal pulsars are similar (e.g. Kramer et al. 1999). A comparison of the radio flux densities (S_ν), where ν is the observing frequency, and the spectral indices (α) between MSPs and normal pulsars indicates that their emissions are not notably different. The pulsar radio flux density can typically be described by a single power law, $S_\nu \propto \nu^\alpha$, and from a recent study (Bates et al. 2013) the mean spectral index is -1.4. However, MSP spectral indices may be slightly steeper than those of the normal pulsars (Kramer et al. 1998).

The origin of the radio emission however could be substantially different between MSPs and normal pulsars. The basic radio emission process comes from accelerated charged particles (electrons and positrons) moving relativistically along open but curved magnetic field lines and generating emission and other particles via a cascade process. The charged particles emit radio photons coherently, and as such, the emission is highly non-thermal. The details of these coherent processes are not well understood.

The location of the radio beam for normal pulsars is likely above the surface near the magnetic poles whereas the origin of the MSP radio emission is in the outer magnetosphere, likely near the outermost closed magnetic field lines. *Fermi*

has shown definitively that MSP radio beams are significantly larger than those of normal pulsars, resulting in pulsations from each MSP over nearly a full 4π steradians. This large beaming fraction supports the idea that MSP radio beams originate in the outer magnetosphere, in contrast to those from normal pulsars, which would be much narrower and lighthouse-like, from deeper in the dipolar field near the poles.

For the energetic pulsars (i.e. pulsars detected in gamma-rays) several emission models have been proposed. Polar cap models, which assume that gamma-ray photons come from near the surface above the magnetic polar caps, have been disfavored by *Fermi* LAT (see Section 1.3.1 for more details about the *Fermi* LAT) observations (Abdo et al. 2010b). The more favored models are the outer-magnetospheric emission models such as outer-gap, slot-gap, two-pole caustic, and pair-starved polar cap models; see Johnson et al. (2014) for a review of these gamma-ray emission models. However, the best-fitted gamma-ray emission models seem to vary from pulsar to pulsar. *Fermi* has opened a new era in high-energy pulsar studies with a phenomenal 205 gamma-ray pulsars detected in the past 7 years. These discoveries should lead to many additional insights into the complex pulsar emissions processes.

1.1.4 Pulsar timing

Pulsar timing monitors neutron star rotations by tracking the arrival times of individual (or averaged) pulses from pulsars. The main point in pulsar timing is that every single rotation is unambiguously accounted for over a long period of time (decades for some pulsars). Due to the clock-like rotational stability of pulsars, the observed rotational phases from pulsations can be precisely tracked. The unambiguity and precision of pulsar timing allows astronomers to make very accurate astrometric and spin measurements of the pulsar, high-precision determinations of orbital parameters,

and unique measurements of the intervening interstellar medium (ISM). The applications of pulsar timing are various and astonishing, and include testing gravitational theories in the strong field regime, studying the dense interiors of neutron stars, and possibly directly detecting gravitational waves (GWs).

Times of Arrival (TOAs)

After a new pulsar is discovered, a series of initially densely (but progressively less so) sampled observations are made of the pulsar in order to unambiguously track the rotational phase of the pulsar. Once that phase is established, the pulsar is regularly observed once or twice per month for at least a year to establish a "pulsar timing solution". During these observations, the data receive a time stamp from a reference clock at the telescope (which itself is referenced to GPS). With the time stamp and a stable frequency reference (typically a Hydrogen maser) tracking time during the observation, one can determine an accurate time at any point of the observation.

To create a TOA, the data are "folded" modulo the predicted spin period at the observatory and integrated over many pulses to yield averaged pulse profiles as a function of observing frequency. The dispersed folded pulses in frequency are then corrected for the dispersive interstellar delay (see section 1.1.2 for details on dispersion) and partially or completely integrated over frequency. The resulting pulse profiles are cross-correlated with a noise-free template profile which is based on an averaged pulse profile of high signal-to noise. The cross-correlation measures the time (or phase) difference between the profile and the template. Since the absolute reference time of the data, at the beginning or the middle of the folded integration, is known, the absolute time-of-arrival of the averaged pulse profile can be measured. Fig. 1.4 summarizes the steps in generating TOAs (Lorimer & Kramer 2005).

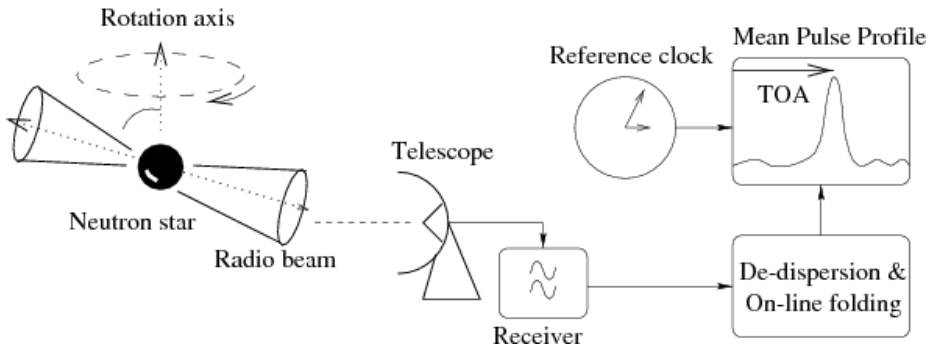

Fig. 1.4.—: Stages of pulsar timing: beginning with observing a pulsar, dedispersion, folding the data to establish an integrated pulse profile, and generating TOAs by cross-correlating the pulse profiles with a template profile. *Image credit: Lorimer & Kramer (2005)*

The uncertainty of the TOA ($\sigma_{\rm TOA}$) is roughly proportional to the ratio of the pulse profile's width (W) and its signal-to-noise (S/N),

$$\sigma_{\rm TOA} \simeq \frac{W}{S/N}. \tag{1.7}$$

High S/N MSPs with narrower pulse profiles are therefore preferable for high-precision pulsar timing than normal pulsars. Moreover, the old MSPs are more stable rotators and show much less intrinsic timing noise than young pulsars.

Timing models and timing residuals

To a good approximation, the Solar System center-of-mass (or barycenter, SSB) is an inertial frame where time advances as a constant rate. In the SSB frame, we can predict the arrival times of pulses observed via TOAs with a simple Taylor expansion of the time-dependent phase of a pulsar, $\phi(t)$, where

$$\phi(t) = \phi_0 \; + \; f(t - t_0) \; + \; \frac{1}{2}\dot{f}(t - t_0)^2 \; + \; \ldots, \tag{1.8}$$

ϕ_0 and t_0 are the reference phase and time, and f and $\dot{f}$ are the pulsar's spin frequency and frequency derivative (i.e. spin-down, due to losses of energy to particle and electromagnetic radiation).

Since a telescope is in the frame of a rotating Earth orbiting the Sun, the observed (topocentric) TOAs need to be transformed into the SSB (barycentric) frame. To transform the topocentric TOAs ($t_{\rm topo}$) to barycentric TOAs (t), many time corrections needed to be applied,

$$t = t_{\rm topo} \; - \; t_0 \; + \Delta t_{\rm clock} \; - \Delta t_{\rm DM} \; + \Delta t_{\rm R} \; + \Delta t_{\rm rel} \, , \tag{1.9}$$

where t_0 is the reference time, $\Delta t_{\rm clock}$ corrects the observatory clock to an international atomic time standard, $\Delta t_{\rm DM}$ is the time delay from the dispersion, $\Delta t_{\rm R}$ is the Römer time delay (projected light travel time from the telescope to the SSB) and $\Delta t_{\rm rel}$ comprises the Einstein and Shapiro time delays due to general relativistic propagation or clock rate corrections in the Solar System.

We use the program TEMPO to barycenter the TOAs and create a timing model which fits the TOAs via least-squares. The model fitting is performed in an iterative manner by starting the fit with initial pulsar parameters (like the spin period and sky location during the time of discovery) and improving those parameters, and adding others as necessary, as additional observed TOAs and longer timing baselines are accumulated.

The timing residuals (i.e. the difference between the observed TOAs and the timing model) of the best-fit model should optimally show a Gaussian distribution around zero (i.e. flat, white-noise residuals) if the model is appropriate. Whereas errors in timing model parameters cause systematic signatures in timing residuals. Fig. 1.5 shows how timing residuals can be affected by various timing parameter errors.

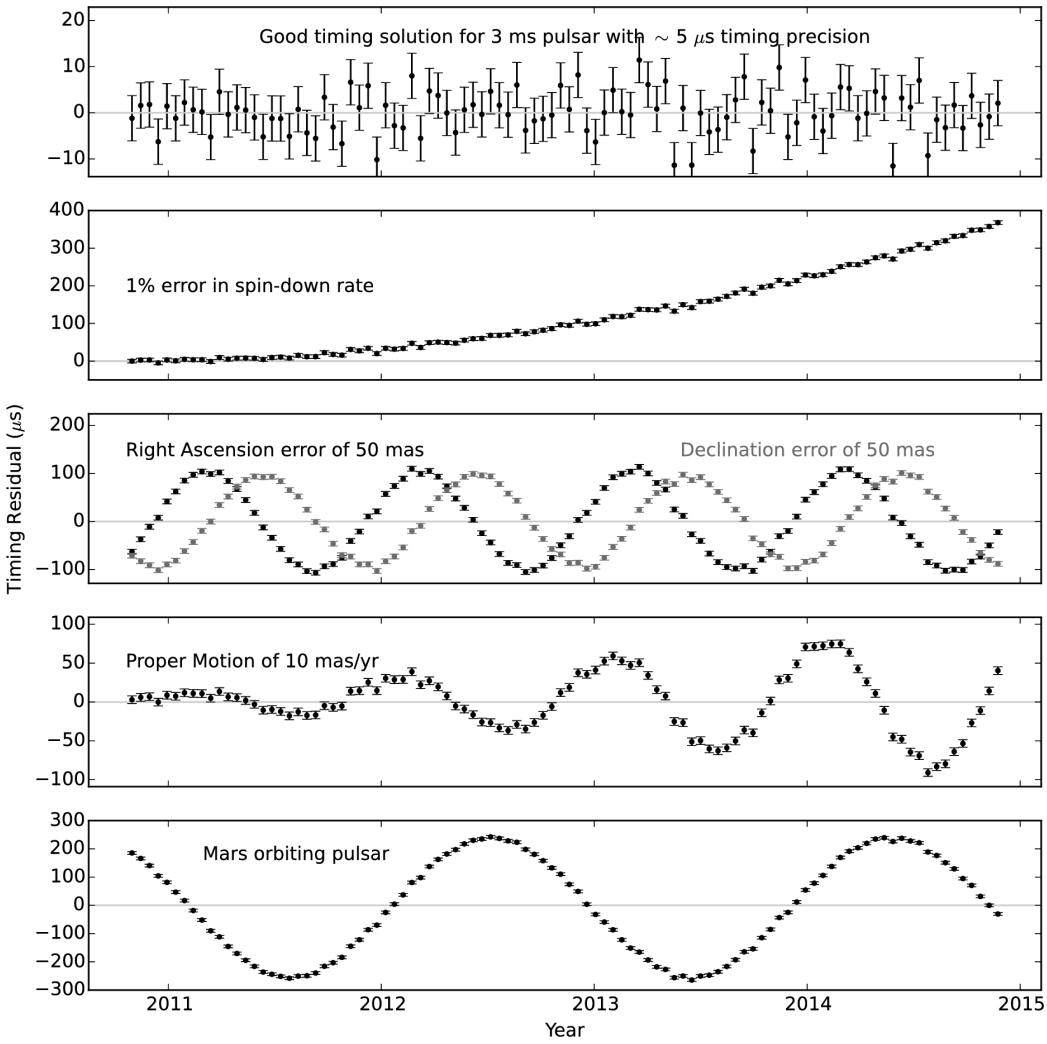

Fig. 1.5.—: Examples of five different sets of pulsar timing residuals. From top to bottom, "good" timing parameters (showing flat residuals), an error of 1% in spin-down rate (showing a quadratic drift in pulse phase), errors in positions by 50 mas (resulting in annual sinusoids), an error of 10 mas/yr in proper motion (showing an annual sinusoid which grows with time), and the presence of a Mars-like planet around the pulsar. *Image credit: Scott Ransom*

Timing binary pulsars

To time binary pulsars, the timing model needs to incorporate additional parameters to compensate for orbital motion. That motion can typically be described using five "Keplerian parameters", including the orbital period ($P_{\rm b}$), projected semi-major axis of the elliptical orbit ($x \equiv a \sin i/c$), orbital eccentricity (e), longitude of periastron (ω) and the epoch of periastron passage (T_0).

When x and $P_{\rm b}$ are measured from pulsar timing, the mass function ($f_{\rm m}$) of the pulsar mass ($m_{\rm p}$), companion mass ($m_{\rm c}$), and orbital inclination (i) can be obtained,

$$f_{\rm m} = \frac{4\pi^2}{G}\frac{x^3}{P_{\rm b}^2} = \frac{(m_{\rm c}\sin i)^3}{(m_{\rm p}+m_{\rm c})^2}\,, \tag{1.10}$$

where G is the Newton's gravitational constant. In practice, the orbital inclination is unknown, therefore a lower limit of the companion mass can be estimated by assuming $i = 90^\circ$ and $m_{\rm p} = 1.35\,M_\odot$.

For the pulsars in compact binary orbits which are more likely to be relativistic, an additional set of "post-Keplerian" (PK) parameters are possibly required in order to achieve high-precision timing solutions. Potentially observable PK parameters include the relativistic advance of periastron ($\dot{\omega}$), a combination of time dilation and gravitational redshift (γ), the rate of orbital decay due to gravitational radiation ($\dot{P}_{\rm b}$), and the two Shapiro delay parameters r and s. In general relativity, all five of the PK parameters are functions of only the well-measured Keplerian orbital parameters and $m_{\rm p}$ and $m_{\rm c}$. By measuring some or all of the PK parameters, one can measure the masses of the pulsar and companion star and potentially test general relativity or other gravitational theories. Since the majority of MSPs are in binaries and can be timed more precisely than normal pulsars, MSPs are ideal for exploring exotic physics

via pulsar timing.

The *Fermi* LAT has assisted in the discovery of many rare types of binary MSPs in compact (orbital period of <1 day) orbits with low-mass companions ($\lesssim 0.3\,M_\odot$) and which typically show eclipses of the radio pulsations. These so-called "spider" systems are known as "black widows" (if the companions are very low mass, $\lesssim 0.08\,M_\odot$) or "redbacks" (strongly eclipsing binary pulsars with low-mass main sequence companions). Black widows and redbacks were traditionally found in globular clusters where stars are densely packed and stellar interactions can exchange in new companions to the MSPs. The new *Fermi* identified Galactic black widows and redbacks are therefore fascinating systems to study since they may have different evolutionary origins than those found in globular clusters. They seem to be the "missing links" in pulsar evolution (e.g. Archibald et al. 2009; Papitto et al. 2013) from low-mass x-ray binaries (LMXBs) to MSPs.

Eclipsing pulsars in tight orbits however, are more challenging to time. In some systems the eclipses last more than half of the orbit and ionized gas from the companion star additionally delays the radio pulses. As a result, the TOAs from these systems can be of poor quality. Classical effects from the bloated companion stars randomly perturb the orbits on month and year timescales as well, potentially causing pulse rotational ambiguities if the observation cadence is not dense enough.

Pulsar timing applications

As mentioned earlier, pulsar timing is a powerful tool which allows astronomers to measure parameters of the pulsar, its possible orbits, and the ISM very accurately. There are various applications from the precisely measured parameters namely:

- By measuring variations in the DM from the pulsar, one can probe the properties

of the ISM between the pulsar and the observer.

- For binary pulsars in eccentric orbits, like the first binary pulsar B1913+16, the PK parameters $\dot{\omega}$ and γ can be measured precisely. That allows astronomers to accurately determine the mass of pulsar and the companion. For B1913+16, $\dot{P}_{\rm b}$ was eventually detected, which implied the existence of the orbital decay due to the emission of gravitational radiation as predicted by GR (Weisberg & Taylor 2005).

- For the double pulsar system, J0737−3039, all five PK parameters have been precisely measured. These measurements show that GR is correct to better than 0.05% and precisely provided the masses of both pulsars with fractional uncertainties of 10^{-4} (Kramer et al. 2006).

- The detection of the general relativistic Shapiro delay from pulsar timing of the binary pulsar PSR J1614−2230 allowed us to infer the mass of both the pulsar and the companion very precisely. The pulsar mass is 1.97 ± 0.04 which was the heaviest high-precision pulsar mass known to date (Demorest et al. 2010). Its measurement has provided a very strong constraint on the physics of matter at supra-nuclear densities, and in particular, the so-called neutron star Equation of State (EOS).

Over the last decade, the direct detection of gravitational waves (GWs), the distortions of space-time caused by the motions of exotic and massive compact objects, has become a major goal of pulsar studies. By timing arrays of MSPs distributed over the whole sky for many years, so-called pulsar timing arrays (PTAs) are looking for correlated distortions in the timing residuals from nanoHertz frequency GWs passing through our galaxy. The sources of the GWs are likely to be supermassive black hole

binaries scattered throughout the universe. The International Pulsar Timing Array (IPTA) is the collaboration of three PTA organizations: NANOGrav in North America, and the Parkes (in Australia) and European PTAs. Given the improvement in pulsar timing from the IPTA, the GWs could possibly be detected within five to ten years. A crucial improvement in GW sensitivity comes from adding new MSPs to PTAs and the recent search successes, especially aided by *Fermi* have dramatically contributed to PTA science.

1.2 Searching for New Pulsars

The periodic signals from the first pulsar, PSR B1919+21, were discovered in 1967 by visually inspecting the total power output from a radio telescope in Cambridge, England and directly seeing individual pulses. However, the majority of known pulsars to date are much too weak to be found by searching for individual pulses and therefore require more sophisticated methods in order to search for their faint pulsations. Currently, "standard" radio pulsar search procedures are performed in both the time and frequency domains via de-dispersion of channelized data and then Fourier analysis of the resulting time series. Additionally, more advanced techniques, namely acceleration searches and single-pulse searches, increase our sensitivity to exotic pulsars in binary systems as well as rare but bright giant pulses from certain pulsars, respectively.

The standard procedure used in searching for the unknown spin period and dispersion measure (DM), an integral of the *a priori* unknown free electron number density along the line of sight between a pulsar and an observer, is briefly summarized as follows. The data are de-dispersed and integrated over observing frequency at a wide range of trial DMs resulting in a number of time series. Each time series is Fourier

transformed, then typically squared to make a power spectrum, and then possible harmonic information is summed in various combinations to near-optimally recover all the power from pulsations. The results of the periodic search process are saved and are then human-inspected and/or processed by machine learning programs in order to find good pulsar candidates. For the best candidates, the raw data folded at the fundamental frequency found in the Fourier analysis in order to further investigate whether the candidates are real pulsars. The processes is repeated for each trial DM.

1.2.1 RFI removal

Radio Frequency Interference (RFI) is interference from terrestrial (or satellite) radio transmitters that can significantly contaminate the data and reduce our sensitivity to detect new pulsars. Some RFI imitates the signature produced by periodic signals from pulsars. If RFI is not treated properly, it can overpower the pulsar signals, causing them to be only weakly detected or even missed all together. RFI must therefore be carefully removed before starting the pulsar searches.

The potential sources RFI are many, from electrical storms, to nearby electrical devices (microwaves, laptops etc.), and much further transmitters such as radars, aircraft, and satellites. The worst RFI for pulsar searching are those with pulsing broadband signals which are therefore similar to the periodic signals from pulsars. Fortunately, these sources are terrestrial and therefore are not dispersed in the same manner as those from pulsars which traveled through the ionized ISM. The majority of RFI instances have apparent DMs of zero. We attempt to remove interference at several different stages of the search pipeline, from initial data processing and dedispersion, to "zapping" of known periodic signals from the Fourier power spectra, to post-facto discarding of folded candidates with non-pulsar-like characteristics.

1.2.2 Dispersion Measure trials

As the DM towards a pulsar is unknown prior to discovery, many DM trials must be searched. To save time and computer power, the step sizes over DM must be optimized. The steps must not be so large that the true DM value falls well between two trial DMs, nor so small that computations are wasted. Determining an ideal DM step size is especially crucial when it comes to detecting pulsars with short spin periods, because the S/N of a detection reduces strongly as the error in DM increases, in a manner proportional to the spin frequency of the pulsar. The optimal DM step size also depends on many observing factors, namely the full range of trial DMs, the central observing frequency, the observing bandwidth, and the sample time.

We used `DDplan.py` from `PRESTO` to determine the DM step sizes for each observation. The optimal DM range for searching can be estimated from the maximum DM value from a model of the electron density distribution in the galaxy (e.g. NE2001 (Cordes & Lazio 2002)) multiplied by a factor of two (to account for the uncertainty in the model). In general, a maximum DM of more than $1000\,cm^{-3}\,pc$ is expected for surveys along the Galactic Plane and less than $\sim 50\,cm^{-3}\,pc$ for high-galactic-latitude surveys. After determining the DM step size and range, we incoherently de-disperse the raw search data into time series at each trial DM value, by shifting the arrival times of each frequency channel according to the DM and summing across the observing band.

1.2.3 Periodic Searches

The most widely used technique for periodicity searching is to Fourier transform the de-dispersed time series and examine them in the frequency domain. Since the time series are formed from independently, and typically uniformly, sampled data points,

we use the Fast Fourier Transform and then convert the Fourier amplitudes to powers to make a power spectrum.

The periodic signals from pulsars typically have small duty cycles (the pulse width divided by the spin period). As a result, the signals appear in the Fourier domain as numerous evenly-spaced narrow peaks, comprising the fundamental frequency and a number of harmonics (each separated by the spin frequency of the pulsar). To increase the detection significance for pulsars with such narrow pulses, the fundamental frequency power and up to 32 harmonics are summed together. This technique is called "harmonic summing". The smaller the duty cycle, the more harmonics are able to be summed to reach the optimal gain. The best fundamental frequency as determined from harmonic summing (and which includes Fourier interpolation) is then converted to a best spin period in the time domain. The best periods from each time series are saved for further investigation.

1.2.4 Acceleration Search

For pulsars in binary systems, the binary motion causes a slight change in the observed spin period due to the Doppler effect. This results in a distribution of pulsation power over multiple Fourier bins in the frequency domain, which dramatically reduces the search sensitivity. To mitigate this effect, we performed "acceleration searches".

The Doppler equation of an observed pulsar frequency as a function of time, $\nu(t)$ = 1/spin period, is

$$\nu(t) \;=\; \nu_0(\,1 \;-\; \frac{V_l(t)}{c}\,) \tag{1.11}$$

$$V_l(t) \;=\; a_l t \;+\; V_l(0), \tag{1.12}$$

where ν_0 is the intrinsic frequency, $V_l(t)$ is the line of sight velocity of a pulsar, c is the

speed of light and a_l is the line of sight acceleration of a pulsar. The acceleration is simply assumed to be constant during the observation, and is an additional parameter to search for during the periodic searching process.

We used `PRESTO`'s routine `accelsearch` to account for the signal drifting over Fourier bins due to orbital acceleration and to perform a periodic search using Fourier interpolation and harmonic summing of 1, 2, 4, 8 or 16 harmonics. The acceleration search is a crucial part of the full search process here as we expect most MSPs to be in binary systems.

1.2.5 Candidate selection

For each observation, the result after RFI removal, de-dispersion, and acceleration searching are candidate periodic signals with a spin period and a DM value. The time series are then folded at the spin period and either visually inspected or passed to machine learning software to find pulsar-like signals. After some good candidates are found in the time series, the raw data are folded (a much more time-consuming process) to see if the candidate's peak at non-zero DMs and otherwise appear to be real pulsars. The key features of a real pulsar on a candidate plot are a continuous signal (straight line) in both time-phase and frequency-phase plots and a sharp peak (at non-zero DM) on the DM plot. Fig. 1.6 shows a plot of the de-dispersed and folded raw data of the pulsar, PSR J2042+0249.

1.2.6 Single-pulse search

Besides periodic pulses, pulsar emission may occasionally vary greatly in amplitude and result in apparent sporadic signals. Some pulsars, for example, exhibit nulling behaviour which means that the pulsations "turn off" and then "turn on" at some

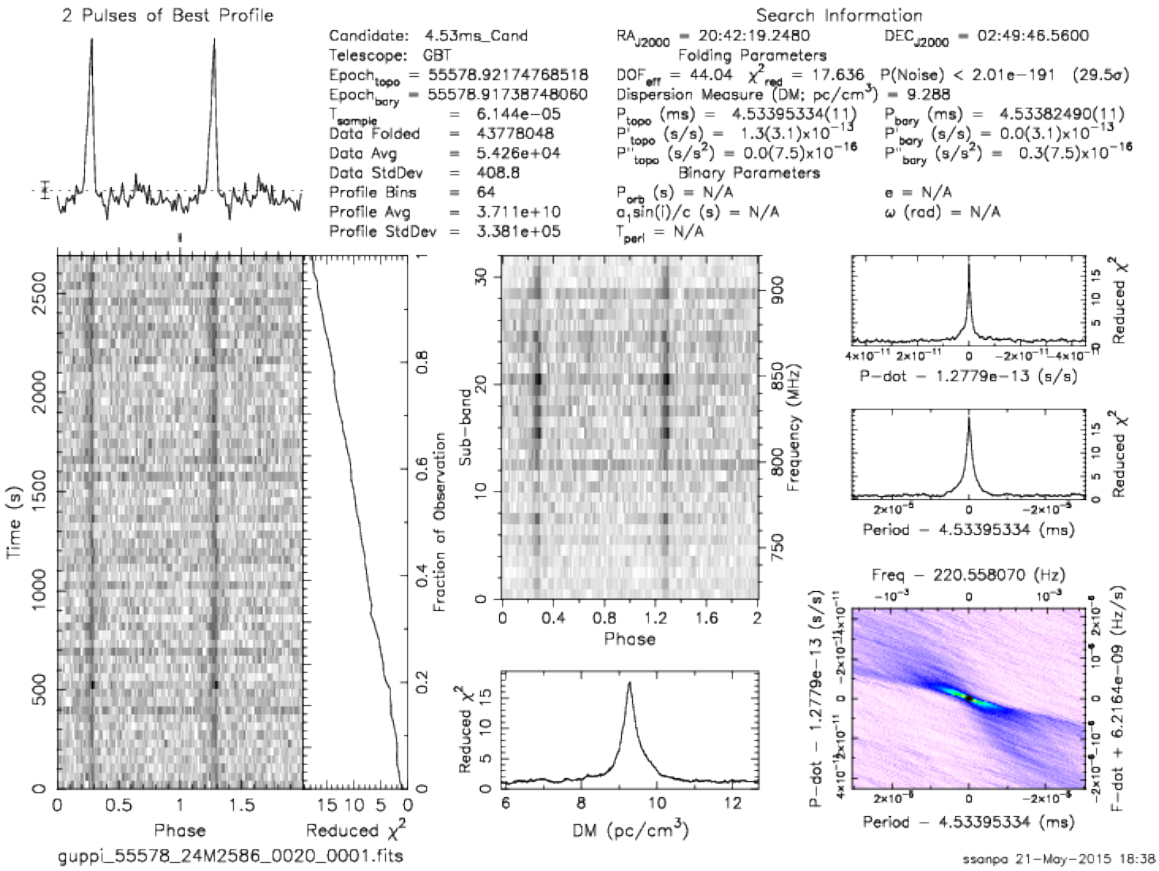

Fig. 1.6.—: This is a raw-data-folded plot of PSR J2042+0249. It shows all the features of true pulsar signals.

later time interval. Other examples include the rotating radio transients (RRATs) (McLaughlin et al. 2006) which are thought to be old rotating neutron stars which only rarely emit a pulse of radio emission. The periodicity search in the Fourier domain is not sensitive to this type of radiation from pulsars; therefore the "single-pulse search" technique has to be applied.

The concept of single-pulse searches is simple. Instead of searching for periodic signals for each trial DM, each time series is examined for large individual pulses. If a pulsar is a sporadic emitter, or emits giant pulses, those events can be detected in a correctly de-dispersed time series using simple matched-filtering with a boxcar signal.

Searching for single pulses in time series is essentially finding events in the time series which deviate from the mean by several standard deviations (given that the time series has Gaussian noise with known mean and standard deviation). We used `PRESTO`'s `single_pulse_search.py` to search for single pulses in the time series. Fig. 1.7 shows a result from the single-pulse searches.

1.3 *Fermi* Unassociated Sources

1.3.1 *Fermi* satellite

The *Fermi* Gamma-ray Space Telescope was launched in 2008 with two main instruments on board: the Gamma-ray Burst Monitor (GBM) and the Large Area Telescope (LAT). This thesis focuses on sources detected with the LAT. The LAT's field of view is about 2.4 sr, and the main operational mode is a sky survey mode which covers the entire sky every three hours. The LAT detects gamma-ray photons with energies ranging from 20 MeV up to over 300 GeV, and is the most sensitive gamma-ray telescope to date.

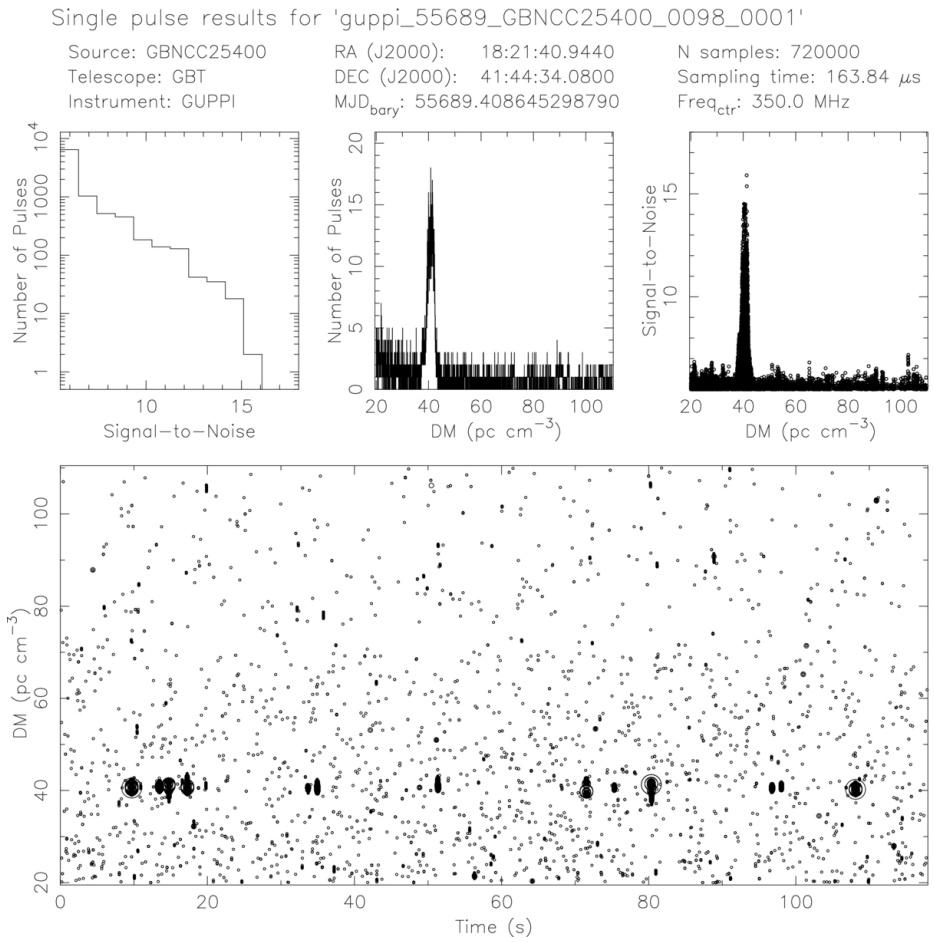

Fig. 1.7.—: Single-pulse search results for pulsar J1821+41. The top left panel shows S/N versus number of detected pulses. The middle and right panels show DM versus number of pulses and DM versus S/N, respectively, which both peak at DM of $\sim 40\,\mathrm{pc\,cm^{-1}}$. The bottom panel shows integration time versus DM: the darker the dots (or the bigger the circles), the higher the S/N of the pulses detected. All panels suggest that this pulsar emits single pulses sparsely at a DM of $\sim 40\,\mathrm{pc\,cm^{-1}}$.

In this thesis I used data from all three *Fermi* source catalogs, 1FGL (Abdo et al. 2010a), 2FGL (Nolan et al. 2012) and 3FGL (Acero et al. 2015), which are based on 11 months, 2 years and 4 years of LAT data, respectively.

1.3.2 *Fermi* "Treasure Map"

After years of continuously mapping the gamma-ray sky, the LAT has revealed thousands of gamma-ray sources. The third *Fermi* LAT source catalog (3FGL), for example, includes 3033 gamma-ray sources above 4σ significance, and 1010 of them are unassociated with other astrophysical sources.

There are three techniques typically used to determine whether any of these unassociated sources are pulsars. The first and most straight forward technique is to temporally fold the gamma-ray data with known pulsar ephemerides if the source position is consistent with a known pulsar location; this technique has revealed 6 gamma-ray pulsars (Abdo et al. 2009a). The second technique is to blindly search for pulsations in the LAT data. Though this is a very algorithmically and computationally difficult task, it has resulted in the discovery of over 37 new gamma-ray pulsars (e.g. Abdo et al. 2009a; Saz Parkinson et al. 2010; Pletsch et al. 2012a,b)

The last and the most promising technique is to observe the unassociated sources in the radio, and search for radio pulsations. This technique was used on unidentified sources found by the previous generation gamma-ray telescope, *Energetic Gamma Ray Experiment Telescope (EGRET)*, where it was unsuccessful in finding any new gamma-ray pulsars (Thompson 2008). The main reason for the poor success in the past was *EGRET*'s large positional uncertainty of typically several degrees. The lack of a precise location necessitates multiple telescope pointings to cover the whole error box, and therefore makes deep radio searches on each source very inefficient.

The localizations for the LAT unassociated sources are much better than those from *EGRET*, typically 10−30 arcmin in size, and so most can be covered by a single pointing with a radio telescope like the GBT. Our target lists for the pulsar searches use gamma-ray criteria laid out by the *Fermi* team: namely, that they be unassociated sources with exponential spectral cutoffs and low variability (see Fig. 1.8 and 1.9).

1.3.3 The Pulsar Search Consortium (PSC)

The Pulsar Search Consortium (PSC) is an international collaborators of radio astronomers from all over the world (Ray et al. 2012). The goal is to search for new pulsars in the *Fermi* LAT unassociated sources and to perform follow-up observations on any new pulsars.

The *Fermi* LAT and the PSC have provided a breakthrough in the pulsar search community by discovering 70 new millisecond pulsars among the *Fermi* unassociated sources (e.g. Ransom et al. 2011; Keith et al. 2011; Bhattacharyya et al. 2013; Camilo et al. 2015). One of the interesting results from the *Fermi LAT* is that 70 out of 72 new pulsars are MSPs in the Galactic disk (those outside globular clusters), and 54 of them are already confirmed as gamma-ray emitters (the remaining ones will likely be proven so with longer timing). Given that it took over 27 years to find 60 Galactic MSPs prior to the the launch of Fermi, the discovery of 70 Galactic MSPs in 8 years is fascinating. In addition to the successful rate of discovery, among these 70 new MSPs at least 28 of them are black widows or redbacks, previously rare and exotic interacting pulsar binary systems. Only 3 black widows and 1 redback were known in the Galactic plane at the time of the *Fermi* launch.

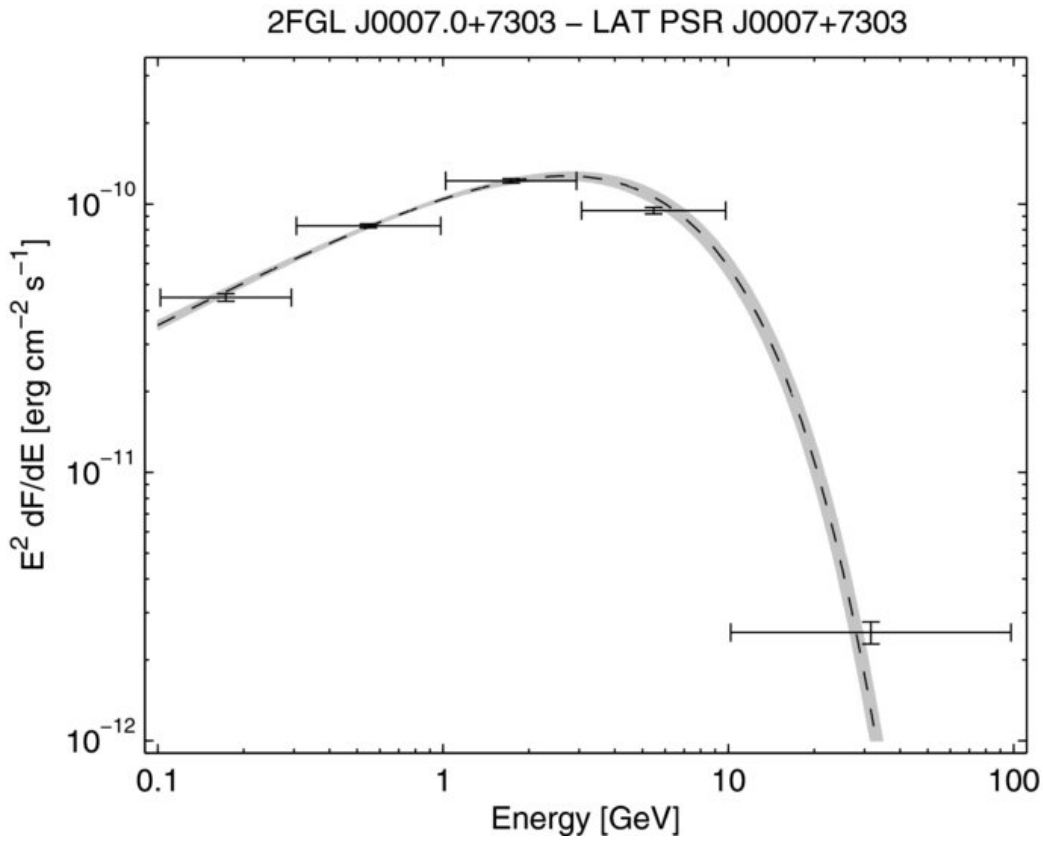

Fig. 1.8.—: An example plot of a gamma-ray spectrum with an exponential cut-off within a few GeV range (Abdo et al. 2013). This spectral shape is one of the characteristics of gamma-ray pulsars.

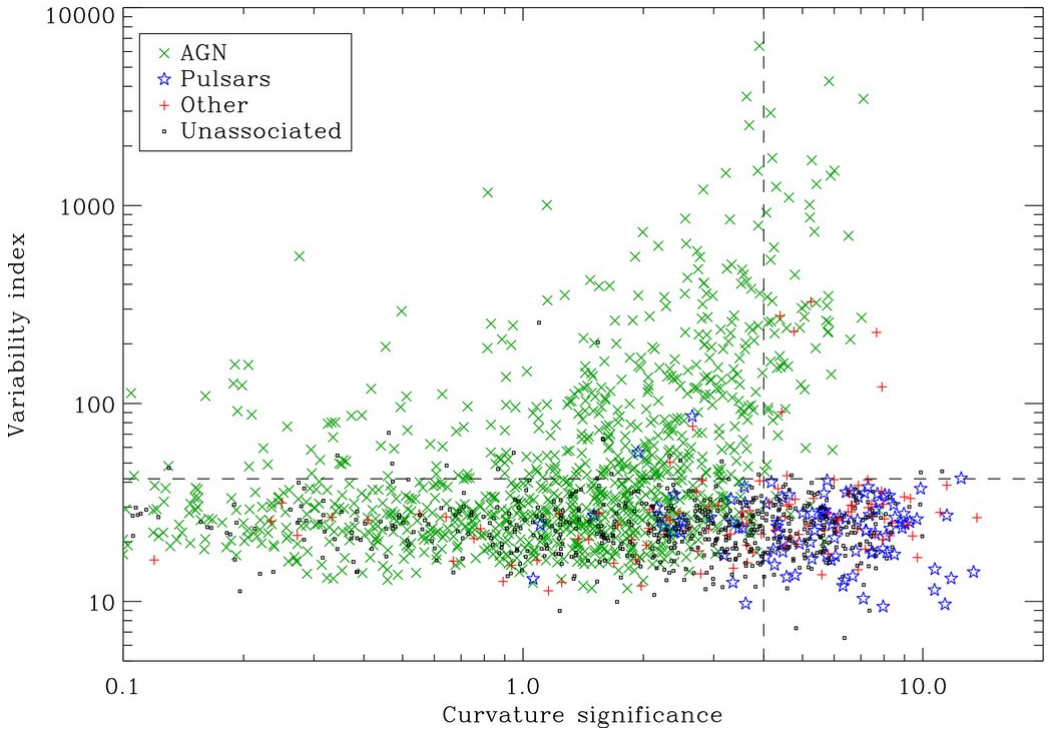

Fig. 1.9.—: Variability and Curvature (i.e. the probability of having a cutoff spectra) statistics of 2FGL sources (Abdo et al. 2013). The known pulsars (blue stars) fall into the region of low variability and high curvature. Therefore, the unassociated sources which fall into the same region are likely to be pulsars as well.

1.4 Pulsar Search with the Green Bank Telescope (GBT)

The Robert C. Byrd Green Bank Telescope (GBT) is the world largest fully steerable single-dish radio telescope. The GBT's 100-meter diameter dish, unblocked aperture and outstanding surface accuracy provide excellent sensitivity across the telescope operation wavelength range from 0.1 to 116 GHz (3.0 m to 2.6 mm). It is also located in the National Radio Quiet Zone, where radio transmitters are under control by the government in order to provide the most "quiet" radio environment for the GBT.

Fig. 1.10.—: The Robert C. Byrd Green Bank Telescope (GBT). *Image creit: NRAO*

The GBT is one of most successful telescopes for pulsar searches as a result of its excellent sensitivity and the Green Bank Ultimate Pulsar Processing Instrument (GUPPI), which is the backend designed specifically for high-performance and wide-band pulsar observations. The GBT has found over 250 new pulsars through large-area surveys, such as the GBT 350 MHz Drift-scan survey and the Green Bank North

Celestial Cap survey (GBNCC) (e.g. Lynch & Bank North Celestial Cap Survey Collaborations 2013), and deep observations of special targets like supernova remnants, globular clusters (e.g. Ransom et al. 2005), and now, *Fermi* unassociated sources.

For the targeted pulsar searches of the *Fermi* unassociated sources, the GBT has played a very major role, discovering 34 of the 70 new MSPs uncovered by the PSC. The discovery of twelve new MSPs with the GBT is discussed in Chapter 2.

For this thesis, we observed more than 100 *Fermi* unassociated sources with the GBT at three different observing frequencies, and are reporting the discovery and timing solutions of 16 of them, including 4 rare "spider" pulsars. The author discovered 10 of these pulsars herself, conducting large-scale acceleration searches on a computer cluster located at NRAO in Charlottesville, VA.

Chapter 2

Discovery of Twelve New Millisecond Pulsars in *Fermi* LAT Sources with the Green Bank Telescope

2.1 Introduction

After seven years of operation, the Large Area Telescope (LAT) on board the *Fermi* γ-ray Space Telescope (Atwood et al. 2009) has revolutionized pulsar astronomy by enabling the discovery of many new radio millisecond pulsars (MSPs). Prior to the launch of *Fermi*, radio telescopes searched for pulsars in the error boxes of unassociated γ-ray sources from EGRET (Energetic Gamma Ray Experiment Telescope) on board the Compton Gamma Ray Observatory (CGRO) (e.g. Roberts 2002; Champion et al. 2005; Crawford et al. 2006; Keith et al. 2008). However, the relatively large positional uncertainty of EGRET sources (approximately 1 degree) exceeded the size

of the typical primary beams of large radio telescopes, thereby requiring multiple pointings to cover the gamma-ray sources. This decreased both the sensitivity of the searches and the number of sources which could be observed, and therefore no new pulsars were found, with the possible exception of MSP J1614−2230 (Crawford et al. 2006).

The *Fermi* LAT has much better sensitivity and spatial resolution from 100 MeV to 100 GeV compared to EGRET, resulting in more γ-ray sources in general, and more with source sizes comparable to those of typical radio beams. Single radio pointings can cover the entire error region providing longer observing times and better sensitivity for pulsar searches. To conduct the radio follow-up observations of LAT sources, the *Fermi* Pulsar Search Consortium (PSC), an international collaboration of LAT members and pulsar experts associated with single dish radio telescopes, was established (Ray et al. 2012). After performing a number of radio observations on non-variable and unassociated sources from the first series of LAT external and internal source catalogs, Bright Source List (BSL), 1FGL, 2FGL and 3FGL (Abdo et al. 2009b, 2010a; Nolan et al. 2012; Acero et al. 2015, respectively), 71 new MSPs have been discovered. Given that it took nearly 25 years to find 75 MSPs in the Galactic disk prior to *Fermi*, the discovery of over 70 new Galactic MSPs in seven years is phenomenal.

The National Radio Astronomy Observatory's Robert C. Byrd Green Bank Telescope (GBT) has played a key role in these searches by discovering the first three radio MSPs from the LAT unassociated sources (Ransom et al. 2011), and since then an additional 34 MSPs to date. The first new MSPs triggered the global discoveries of 15 MSPs with the Parkes telescope (e.g. Keith et al. 2011; Kerr et al. 2012), 8 MSPs with the Giant Metrewave Radio Telescope (GMRT) (e.g. Bhattacharyya et al.

2013), 9 MSPs with the Arecibo telescope (e.g. Camilo et al. 2015; Cromartie et al. 2016), 3 MSPs with the Nançay telescope (e.g. Cognard et al. 2011), 1 MSP with the Effelsberg (Barr et al. 2013) and 1 MSP with the Low Frequency Array (LOFAR) (Pleunis et al. in prep.)

This chapter presents 12 new MSPs discovered in *Fermi* LAT unassociated sources with the Green Bank Telescope (GBT). We also present radio timing, γ-ray analyses, and single-pulse searches of the pulsars.

2.2 Source Selection

The process of selecting targets to search for pulsations has been an ongoing effort as the *Fermi* mission has continued to collect data. At the same time, the LAT Collaboration has refined their all-sky analysis methods to account for an improved understanding of the Galactic diffuse emission, as well as the discovery of new and/or unexpected components in the analysis. This study has used inputs from both the 1FGL (Abdo et al. 2010a) and 2FGL (Nolan et al. 2012). catalogs, as well as a preliminary 4-year source list provided through the Pulsar Search Consortium memorandum of understanding (Ray et al. 2012). The γ-ray sources selected for investigation in this program fall into three distinct categories: new unassociated sources, previously searched bright pulsar-like sources, and non-pulsar associated sources with pulsar-like γ-ray spectra.

With each release of a new catalog from the *Fermi*-LAT collaboration, a large and increasing number of unassociated γ-ray sources have been detected: 630, 1,171, and 3,033 from the 1FGL, 2FGL and 3FGL catalogs respectively. These are previously unknown sources whose positions are not strongly associated with a known γ-ray emitting counterpart (probability of association $< 80\%$) when compared against cat-

alogs of known gamma-ray source classes, and taking local source density of each catalog into consideration. We considered all sources at Galactic latitudes above $|b|$ of 2°. This category makes up the majority of the sources we searched. We prioritized sources with little or no γ-ray variability and spectra with exponential cut-offs at a few GeV.

A subset of the bright sources had clearly pulsar-like spectra and are almost certainly pulsars. These sources have been searched multiple times by various radio telescopes at several different frequencies. The non-detections may have resulted from unfavorable diffractive scintillation in the ionized interstellar medium (ISM), or from absorption or scattering in so-called black-widow andor redback systems, which have significant amounts of ionized material escaping from their companion stars.

Finally, we searched a small set of non-varying γ-ray sources that have non-pulsar associations, but that have γ-ray spectra that appear clearly pulsar-like. The *Fermi*-LAT catalog association process invariably includes some false positive associations. In order to select good pulsar candidates from the associated source population, we required first that all sources be non-varying and have significant curvature in their γ-ray spectra. In addition, sources with significant emission above 10 GeV were eliminated from the list, as the cutoff in γ-ray pulsar spectra makes such high-energy emission unlikely for all but the most powerful pulsars.

For all categories, we considered only sources visible from the GBT (i.e. with Dec $> -40°$). In all, we observed 198 unique *Fermi* γ-ray sources. The names of the sources, the positions observed, and the durations and frequencies of the observations are given in Tables 5.6 and 5.7.

Table 2.1. Observation setup

Band name[♯]	Center freq (MHz)	Bandwidth (MHz)	Number of channels	Time res (μs)	Gain (Jy K^{-1})	$T_{\rm sys}$ (K)	$T_{\rm sky}$ (K)	Detection threshold (mJy)[♭]
UHF	350	100	4096	81.92	2	20	50	0.12
UHF	820	200	2048	61.44	2	20	8	0.03
S	2000	800	2048	61.44	1.9	20	3	0.15

Note. — ♯ Following the standard IEEE (Institute of Electrical and Electronics Engineers) radio frequency naming convention.

Note. — ♭ For 50-minute observing session.

2.3 Observation and Data Analysis

2.3.1 Observation Method and Sensitivity

According to the selection criteria described in the previous section, we selected 198 sources from 1FGL, 2FGL, internal LAT 3-year, and 4-year source lists. From 2010 December to 2013 April, we observed these sources for approximately 40−50 minutes each, using the prime focus receiver of the GBT centered at either 350 MHz, 820 MHz or 2 GHz depending on the size of the 95% *Fermi* error regions and the Galactic location (particularly latitude) of the sources.

The majority of high Galactic latitude ($|b| > 2^\circ$) sources have error boxes of approximately $13'$, thus each source was covered by a single pointing of the GBT at 820 MHz (with a beam FWHM of $16'$). For sources with error regions larger than $13'$ and $|b| > 5^\circ$, we used the 350-MHz receiver (with a beam FWHM of $36'$). In order to observe Galactic plane sources ($|b| < 2^\circ$), we used the S-band receiver which is centered at a much higher frequency of 2 GHz. Moving to higher frequencies reduces the contribution of the Galactic synchrotron background ($\propto f^{-2.6}$, steeper than the typical pulsar flux density spectrum which scales as $\propto f^{-1.41}$ (Bates et al. 2013)). However, the GBT's S-band has a FWHM of only $6.2'$, thus, in order to cover the 95% error regions for most of the low-latitude sources, the observations used multiple pointings (typically 7) arranged in a hexagonal grid ($\sim$ 10 minutes per pointing).

For all three observing bands the total intensity signal was recorded with the Green Bank Ultimate Pulsar Processing Instrument (GUPPI) backend in search mode (DuPlain et al. 2008). Bandwidth, number of channels per band and sampling time are given in Table 2.1. The raw data were recorded to hard drives and processed offline.

To determine the minimum detectable flux density ($S_{\rm min}$) of the observation, we used the radiometer equation (Lorimer & Kramer 2005)

$$S_{\rm min} = \frac{({\rm S/N})_{\rm min}(T_{\rm sys} + T_{\rm sky})}{G\sqrt{n_{\rm p} t_{\rm obs} \Delta f}} \sqrt{\frac{P_{\rm cycle}}{1 - P_{\rm cycle}}} \tag{2.1}$$

where the signal to noise ratio threshold $({\rm S/N})_{\rm min} = 8$; the number of summed polarisations $n_p = 2$; and expected pulse duty cycle (pulse width over the spin period) $P_{\rm cycle} = 0.1$. Table 2.1 lists the rest of the parameters used: telescope gain G, system temperature of the GBT $T_{\rm sys}$, and sky temperature $T_{\rm sky}$. The resulting detection thresholds $S_{\rm min}$ are 0.12, 0.03 and 0.015 mJy for $t_{\rm obs}$ =50 min observations at 350 MHz, 820 MHz and 2 GHz respectively. The multiple pointing observations yield $S_{\rm min}$ of 0.03 mJy for a 10-minute integration time at 2 GHz.

2.3.2 Pulsar Search Method

RFI Removal

The data were processed on a 20-node computer cluster at NRAO in Charlottesville, Virginia using standard tools in the `PRESTO` pulsar software package[1] (Ransom 2001). Radio frequency interference (RFI) can contaminate pulsar signals, so we searched for both prominent narrow-band and persistent short-duration broadband RFI. We used the routine `rfifind` to examine the prominent RFI. For persistent low-level RFI, we searched for periodic signals in a total-power time series de-dispersed at DM of 0.0. Then, we created an RFI mask to replace those "bad" data with channel running median values during de-dispersion. We also removed a "zap list" of known periodic signals from the Fourier power spectra of the de-dispersed time series.

[1] http://www.cv.nrao.edu/∼sransom/presto/

Dispersion Removal

As the electromagnetic radiation from a pulsar propagates through the cold and ionized plasma in the Interstellar Medium (ISM), it experiences a frequency-dependent propagation time delay $\Delta t \propto \mathrm{DM} \cdot f^{-2}$,where Δt is the time delay, DM or dispersion measure is the integrated free electron column density along the observer's line of sight, and f is the observing frequency. The time delay causes the pulses observed at higher frequencies to arrive earlier than the ones observed at lower frequencies and potentially smears pulsar signals in time.

In order to compensate for this effect, the data were incoherently de-dispersed (i.e. time-shifted and summed) using the `PRESTO` routine `mpiprepsubband`. The DM trials ranged from 0 to 350 $\mathrm{pc\,cm^{-3}}$ for 350 MHz and 820 MHz observations, and from 0 to 1000 $\mathrm{pc\,cm^{-3}}$ for the 2 GHz observations. This range encompass the predicted DM in the observed directions according to the NE2001 model of the Galactic distribution of free electrons (Cordes & Lazio 2002). The step sizes of the DM trials were near-optimally spaced using the routine `DDplan.py` such that they are small enough to maintain sensitivity to MSP signals at any DM, but large enough to not waste CPU time (see Magro et al. 2011). The de-dispersed time series were Fourier transformed and then searched for periodic signals from pulsars.

Acceleration Searches

Since most MSPs are in binary systems, neglecting the Doppler effect caused by orbital motion might result in missing MSPs during the search. The effect of binary motion causes a change in the apparent pulse frequency and spreads pulsar signal's power over a number of Fourier bins. As a result, the sensitivity of the search is significantly reduced. The number of Fourier bins which we allow a harmonic to drift

during the observation, z, can be determined as described in Ransom et al. (2001)

$$z = \frac{A t_{\rm obs}^2}{cP} \tag{2.2}$$

where A is the corresponding acceleration caused by the binary orbit, P is the spin period of the pulsar, c is the speed of light, and $t_{\rm obs}$ is the observing time. We used the routine `accelsearch` to perform acceleration searches with a maximum z, $z_{\rm max}$, of 50. `accelsearch` performed incoherent harmonic summing of the powers of up to 8 harmonics (in powers-of-two) to increase sensitivity to pulsar signals with narrow pulses and also used inter-binning to partially compensate for the scalloped frequency response of FFTs (Ransom et al. 2002).

For highly accelerated pulsars (e.g. pulsars in compact orbits with short orbital periods, such as relativistic binaries and "spider" systems like redbacks and black widows (Roberts 2013)), the drifting in Fourier bins due to acceleration can dramatically smear a pulsar signal over a long observation time. In this case, the pulsar may only be found in searches of short portions of a longer observation, where the Fourier drifting is substantially less (since $z \propto t_{\rm obs}^2$). To acquire more sensitivity for these pulsars, we searched all the data in both 5-minute and full-duration searches. All the MSPs in this chapter were found in 5-minute and full-time search or full-time search only, which is not unexpected since all of them are not in tight orbits.

Single-Pulse Searches

Searching for individual bright pulses provides an approach which is complementary to Fourier methods, since single-pulse searches can identifypulsars which are too faint "on average", but which have a large intensity variations on short (i.e. comparable to the spin period) timescales. Examples of pulsars discovered with single-pulse searches

are Rotating Radio Transients (RRATs, McLaughlin et al. 2006) and pulsars with so-called giant pulses (Johnston & Romani 2003).

For all our sources we performed single-pulse searches on the de-dispersed time series using `single_pulse_search.py` from `PRESTO`. This routine performs matched-filtering on the time-series data using boxcars of various widths as templates. All pulse candidates above $(\mathrm{S/N})_{\mathrm{min}} = 5$ threshold were saved for further inspection. The actual flux sensitivity depended on the template width n_{box} (usually from 1 to 30 samples) and was calculated as follows:

$$S^{\mathrm{sp}}_{\mathrm{min}} = \frac{(\mathrm{S/N})_{\mathrm{min}}(T_{\mathrm{sys}} + T_{\mathrm{sky}})}{G\sqrt{n_{\mathrm{p}} n_{\mathrm{box}} t_{\mathrm{res}} \Delta f}}. \tag{2.3}$$

The resulting pulse sensitivities were $S^{\mathrm{sp}}_{\mathrm{min}} \times \sqrt{n_{\mathrm{box}}}$, or 1.4, 0.4 and 0.2 Jy for 350, 820 and 2000 MHz respectively. No single pulses were detected (see Section 2.5.3).

2.3.3 Pulsar Timing

The idea of pulsar timing is to create a model of the neutron star rotational behaviour which can precisely predict the arrival times of every pulse from the pulsar. The standard procedure to achieve a pulsar timing model is to iterate and bootstrap a simple initial model based on measured times of arrival (TOAs) using a series of follow-up observations. This iterative process usually results in a "full" timing model (meaning at least an accurate astrometric position, spin frequency, frequency derivative, and Keplerian orbital parameters, if in a binary), within a year.

Following their discovery, each new MSP was part of follow-up timing observations with the GBT using GUPPI in search-mode. The observations were typically at 820 MHz, with 2048 channels over 200 MHz of bandwidth and sampled every 61.44 μs. Occasionally, observations were made at 350 MHz with 100 MHz of bandwidth split

into 4096 channels and using 81.92 μs sampling. For each observation, we generated one or more TOAs by cross correlating the pulse profiles, as integrated across observing frequency and time after folding modulo the predicted topocentric pulse period, with a noiseless pulse template based on gaussian fits to the discovery pulse profile, or a subsequently measured one with high S/N. For some pulsars, after preliminary phase-connected timing solutions were acquired, we switched to using GUPPI in incoherent fold-mode. Those observations, made at 820 MHz, had 2048 frequency channels over 200 MHz of bandwidth, but with 40.96 μs sampling.

For PSRs J1142+0119 and J1312+0051, we acquired extended timing observations with the Nançay telescope at 1.48 MHz using the NUPPI backend with 1024 channels over 512 MHz bandwidth.

We used the `TEMPO`[2] and `TEMPO2`[3] software packages to fit the measured TOAs to timing models which contain astrometric, spin, and binary parameters. For most binary pulsars the DD model (Damour & Deruelle 1986) is well-suited to describe the orbital parameters. However, for pulsars in highly circular orbits, such that

$$\frac{a \sin i}{c} e^2 \ll \frac{T_{\rm res}}{\sqrt{N_{\rm TOA}}}, \tag{2.4}$$

where a is the semi-major axis, i is the inclination angle of the binary, e is the eccentricity, c is the speed of light, $T_{\rm res}$ is the RMS timing precision, and $N_{\rm TOA}$ is the number of TOAs, we used the ELL1 timing model (Lange et al. 2001). In that model, the parameters $\epsilon_1 \equiv e \sin\omega$ and $\epsilon_2 \equiv e \cos\omega$ are defined, where ω is the longitude of periastron, and which are much less covariant than T_0 and ω in the DD model for circular systems. The orbital phase in the ELL1 model is referenced to the time of

[2] `http://tempo.sourceforge.net`
[3] `http://www.sf.net/projects/tempo2`

the ascending node, $T_{asc} \equiv T_0 - \omega P_b/(2\pi)$, where T_0 is the epoch of periastron passage and P_b is the orbital period.

The observed period derivatives ($\dot{P}_{obs}$) are usually contaminated by an apparent acceleration from a transverse motion of the pulsar (known as the Shklovskii effect (Shklovskii 1970)) and an acceleration because of the Galactic potential towards the Galactic center. These effects cause an underestimation of the intrinsic period derivative ($\dot{P}_{int}$) since

$$\dot{P}_{\rm int} = \dot{P}_{\rm obs} - \dot{P}_{\rm Shk} - \dot{P}_{\rm Gal}, \tag{2.5}$$

and

$$\dot{P}_{\rm Shk} = \left(\frac{P}{c}\right) d\mu^2, \tag{2.6}$$

where $\dot{P}_{\rm Shk}$ is a period derivative term from the Shklovskii effect, $\dot{P}_{\rm Gal}$ is a period derivative term resulting from the Galactic gravitational potential, P is the pulsar spin period, c is the speed of light, d is the pulsar distance (estimated by the NE2001 Galactic electron density model (Cordes & Lazio 2002)) and μ is the proper motion of the pulsar. To calculate $\dot{P}_{\rm Gal}$, we adopted the Galactic potential model described in Reid et al. (2009). Without these corrections, the underestimated $\dot{P}_{\rm int}$ leads to the underestimation of physical properties such as spin-down luminosity ($\dot{E} \propto \dot{P}/P^3$) and surface magnetic field strength ($B_s \propto \sqrt{P \cdot \dot{P}}$).

Unfortunately, the proper motion is rather difficult to measure from pulsar timing, especially without extended timing baselines. We therefore calculated proper motion upper limits ($\mu_{\rm up}$) for all new MSPs assuming that $\dot{P}_{\rm Shk,max} = \dot{P}_{\rm obs}$, where $\dot{P}_{\rm Shk,max}$ is the maximum $\dot{P}_{\rm Shk}$. From equation (2.6), the upper limit proper motion, $\mu_{\rm up}$, is

$$\mu_{\rm up} = \sqrt{\frac{\dot{P}_{\rm obs} c}{P d}} \tag{2.7}$$

The values of $\mu_{\rm up}$, compared to μ measured by pulsar timing when possible ($\mu_{\rm timing}$), are shown on Table 2.2.

2.3.4 LAT Data Analysis

This section is contributed by Tyrel Johnson

The LAT is a pair-conversion telescope sensitive to γ-ray with energies from 20 MeV to $>$ 300 GeV with a 2.4 sr field of view (Atwood et al. 2009). The accuracy with which incoming event directions are reconstructed, or point-spread function (PSF), is dependent on the energy (E), interaction point within the instrument, and angle with respect to the spacecraft z axis[4] (θ). For an event belonging to the `SOURCE` class converting in the front of the instrument, the 68% confidence-level PSF radius, averaged over the acceptance, can be approximated as $\Theta_{68}(E) = \sqrt{(0.^{\circ}66(E/1\ {\rm GeV})^{-0.76})^2 + (0.^{\circ}08)^2}$. The total effective area for a near on-axis, 1 GeV, `SOURCE` class γ-ray is $\sim$7000 cm^2. Events triggering the LAT are time stamped using an on-board GPS receiver that is accurate to within $<$1 μs relative to UTC (Abdo et al. 2009c).

For each MSP, we selected LAT P7REP data (Bregeon et al. 2013) corresponding to the `SOURCE` class recorded between 2008 August 4 and 2013 December 4 within 15° of the radio position, sufficient to accommodate the tails of the PSF at low energy; energies from 0.1 to 100 GeV, the lower limit is that recommended for analysis of P7REP data and the upper limit adequately covers the range of known pulsar cutoff energies; and zenith angles $\leq$100°, to reduce contamination of γ-ray from the limb of the Earth. Good time intervals were then selected corresponding to when the

[4]For more details see
`http://www.slac.stanford.edu/exp/glast/groups/canda/lat_Performance.htm`
and Ackermann et al. (2012).

instrument was in nominal science operations mode, the data were flagged as good, and the rocking angle of the spacecraft did not exceed 52°. These good time interval selections allowed us to construct one all-sky exposure cube and binned exposure map for all the MSPs, similar to what was done by (Acero et al. 2015), for example. All LAT analyses were performed using the *Fermi* Science Tools v9r32p5[5].

2.3.5 Joint γ-ray and Radio Timing

This section is contributed by Scott Ransom

For each of the MSPs, we used the radio timing ephemerides as well as the `fermi` plugin for `TEMPO2` to assign each LAT event to the appropriate rotational phase of the pulsar. This resulted in γ-ray-pulsation detections for each MSP. For PSRs J0533+6759. J1630+3734, J1858−2216, J2310−0555, and J2042+0246, the γ-ray pulsations are quite strong, relatively "sharp", and persist for over seven years, significantly longer than our radio timing baselines. For these pulsars, we conducted an MCMC timing analysis using individual gamma-rays to better refine the apparent frequency derivative, and potentially to constrain or measure proper motion.

We applied a likelihood calculation via MCMC for each and every photon over the full *Fermi* mission and optimized the resulting pulse profile in an iterative manner, similar to that described in Pletsch & Clark (2015). As in Abdo et al. (2013) we calculate the log likelihood $\mathcal{L}$ for all N photons (numbered as j and arriving at times t_j), based on an assumed timing model $\mathbf{u}$ comprising many parameters, and an assumed stable gamma-ray pulse profile $F(\phi)$, where ϕ is the rotational phase of the pulsar. The area-normalized pulse profile is treated as a probability density function for arriving photons. The known LAT response as functions of energy and position,

[5]Available for download at `http://fermi.gsfc.nasa.gov/ssc/data/analysis/software/`.

in combination with a model gamma-ray sky and model pulsar spectrum, allow us to assign weights w_j for each photon, indicating their likelihood of coming from the pulsar in question.

Together, we have

$$\log \mathcal{L}(\mathbf{u}) = \sum_{j=1}^{N} \log \left[w_j \, F(\phi_j(t_j, \mathbf{u})) + (1 - w_j) \right] ,$$

which we can then maximize via MCMC techniques while varying the timing parameters in $\mathbf{u}$. Our current implementation is based on `emcee` (Foreman-Mackey et al. 2013) which uses affine transforms to efficiently explore high-dimensional parameter spaces (like $\mathbf{u}$) and map out parameter confidence regions, even when they are highly correlated. The timing model calculations, including relativistic corrections, are performed using the new high-precision timing software `PINT`[6], a next-generation high-precision pulsar timing code being developed as independent checks of, and modern improvements upon, the traditional timing packages `TEMPO` and `TEMPO2`. The *Fermi* tools process the photons and transform their time stamps from the location of the spacecraft to the geocenter so that `PINT` can fit for a variety of astrometric parameters. These single-photon Bayesian MCMC techniques, coupled with `PINT`, allow us to extract all the useful timing information from each LAT photon.

Our preliminary implementation of this technique, called `event_optimize.py`, is available as part of `PINT`. We used it to determine improved spin frequency derivatives (due to the much-longer γ-ray timing baseline) for the five MSPs J0533+6759, J1630+3734, J1858−2216, J2042+0246, and J2310−0555, whose frequency derivative from the MCMC analysis deviated by more than $1\,\sigma$ from, and was more precise than, the radio timing results.

[6] `https://github.com/nanograv/PINT`

2.4 Results

2.4.1 The New MSPs

We have phase-connected timing solutions for all twelve MSPs spanning over 7.2 years of observations. One of the MSPs is isolated (J0533+6759), and the remaining MSPs are all "normal" binary MSPs with likely He-WD companions. With our radio timing ephemerides, we folded γ-ray photons from 7.2 years of *Fermi* LAT data and found that each of the MSPs exhibits γ-ray pulsations. We were able to measure proper motions from four MSPs: PSRs J1142+0119, J1312+0051, J1630+3734 and J2042+0246 (see Table. 2.2). The timing residuals for each pulsar are shown in Fig. 2.1 and timing parameters are in Tables 5.1, 5.2, 5.3, 5.4, and 5.5.

The newly discovered pulsars have spin periods in the range of 2.38−5.06 ms with DMs between 9.3−109.2 pc cm^{-3}. PSRs J2024+0246 and J2310−0555 exhibit strong scintillations at our observing frequency of 820 MHz making them often difficult to detect. All 12 MSPs have rather sharp radio profiles with one to eight components.

PSR J0533+6759

PSR J0533+6759 is the only isolated MSP in this chapter. It has a spin period of 4.39 ms and DM of 57.30 pc cm^{-3}. We determined the $\dot{P}$ of 12.61×10^{-21} from the MCMC γ-ray analysis.

The long integration times used for this survey cause reduced sensitivity to binary pulsars due to their orbital accelerations. While acceleration searches partially mitigate these effects (see section 2.3.2), we are still biased against finding pulsars in compact binaries, and are therefore relatively more sensitive to isolated pulsars. This effect can be seen in the population of MSPs in Globular clusters, which is $\sim$ 42 %

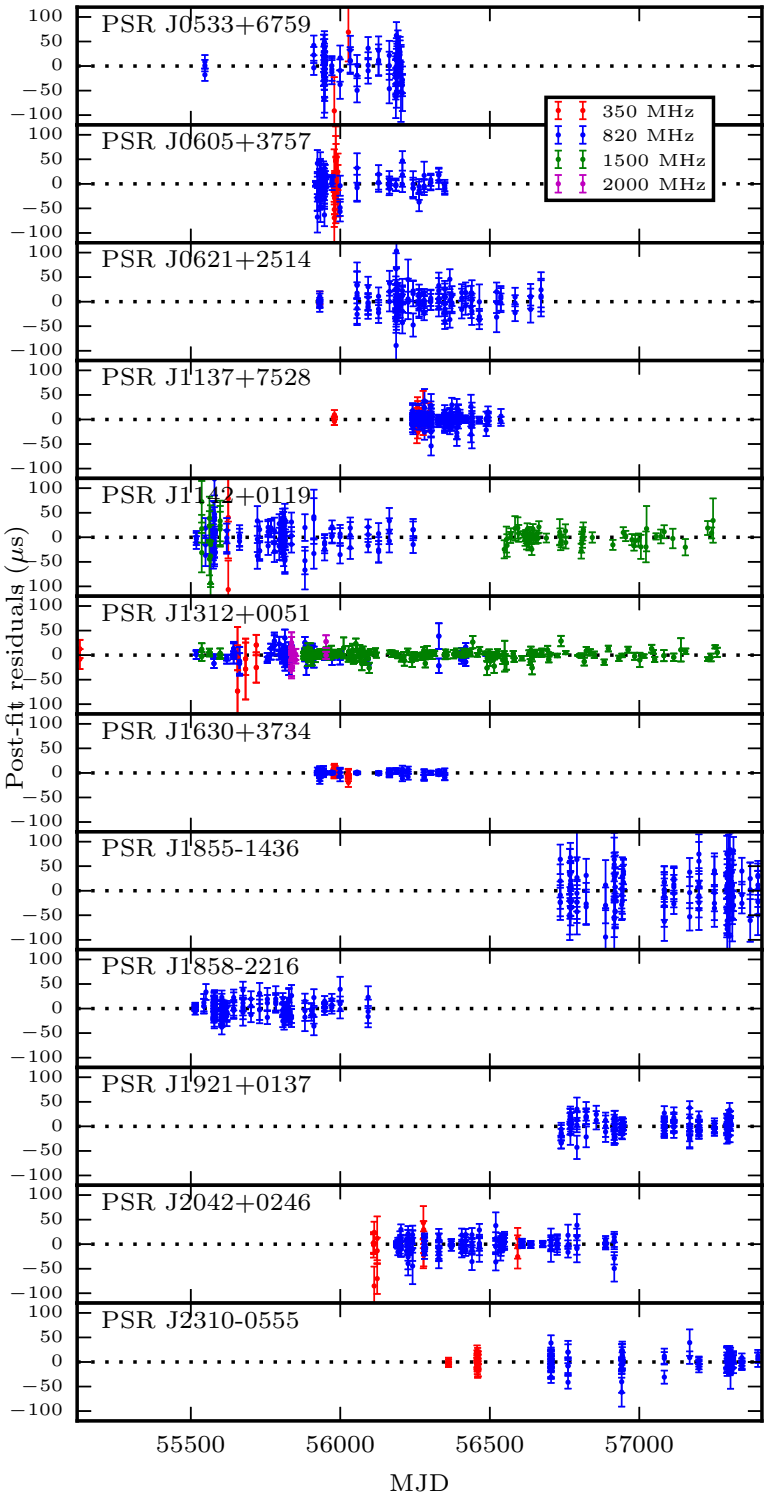

Fig. 2.1.—: Post-fit timing residuals of nine MSPs with timing solutions. The data observed at 350, 820, and 2000 MHz were taken at the GBT, while the data observed at 1500 MHz were taken at the Nançay telescope.

isolated[7], compared to $\sim$ 25 % in the field[8], due to hours-long integration times. Our searches are 45−50 minutes for each source, much longer than the few-minute integrations of all-sky surveys. Despite this bias in favor of finding isolated MSPs, there have been only seven isolated MSPs found in searches of *Fermi* unassociated sources ($\sim$ 10%). The lack of isolated MSPs may be related to the large numbers of energetic "spider" pulsars (i.e. black widow or redback systems (Roberts 2013)) uncovered in these searches. Those systems, likely ablating away their companions, may be the evolutionary predecessors for isolated MSPs. This implies that *Fermi* LAT MSPs are, on average, younger than the typical MSP.

PSR J0621+2514

PSR J0621+2514 has a spin period of 2.72 ms, a DM of 83.64 pc cm^{-3}, a minimum He-WD companion mass of 0.15 $M_\odot$ and an orbital period of 1.26 days, the shortest orbital period among the MSPs in this chapter. In addition, this pulsar has a relatively high spin-down luminosity (4.7×10^{34} ergs s^{-1}).

PSR J1142+0119

PSR J1142+0119 has an extremely small eccentricity that cannot yet be measured from pulsar timing. It has a spin period of 5.1 ms, a DM of 19.2 pc cm^{-3}, a He-WD companion minimum mass minimum limit of 0.15 $M_\odot$ and an orbital period of 1.58 days. Despite a timing baseline of 4.7 years, we have only a weak measurement of proper motion of 105 ± 62 mas yr^{-1}. Given a distance of 0.9 kpc, and Equation (2.7), the upper limit on proper motion is < 37 mas yr^{-1}. This suggests that we need a longer pulsar timing baseline in order to measure a significant proper motion. It

[7]From `http://www.naic.edu/~pfreire/GCpsr.html`
[8]From `http://astro.phys.wvu.edu/GalacticMSPs/GalacticMSPs.txt`

also suggests that the DM-distance may be underestimated.

PSR J1312+0051

PSR J1312+0051 has a spin period of 4.23 ms, a DM of 15.35 pc cm^{-3}, a minimum He-WD companion mass of 0.18 $M_\odot$, and an orbital period of 38.5 days. With the long radio timing span of over five years, we were able to measure significant proper motion of 25.00 ± 0.89 mas yr^{-1}, which allowed us to obtain a more precise intrinsic period derivative of 12.0×10^{-21} by correcting for Shklovskii effect at a distance of 0.8 kpc.

PSR J1312+0051 is bright and well-timed, with a relatively low timing RMS of 4.8 μs (low given that most of the timing data were taken in search-mode at the GBT). It is in the Arecibo declination range and has been included in the NANOGrav pulsar timing array (e.g. The NANOGrav Collaboration et al. (2015)).

PSR J1630+3734

PSR J1630+3734 is also a MSP in a binary system with a He-WD companion. It has a spin period of 3.32 ms, a DM of 14.13 pc cm^{-3}, a minimum companion mass limit of 0.24 $M_\odot$ and an orbital period of 12.53 days. Using a more accurate $\dot{P}$ of 10.77×10^{-21} from the longer-term MCMC γ-ray timing analysis enabled a radio timing measurement of a 16.1 ± 3.4 mas yr^{-1} proper motion.

The relatively low timing RMS of 3.6 μs, might make this pulsar a candidate for NANOGrav. However, the declination of 37° is near the limit of the declination range for the Arecibo telescope. J1630+3734 should be a great candidate for a future high sensitivity pulsar timing array using the Five-hundred-meter Aperture Spherical radio Telescope (FAST) or the Square Kilometer Array (SKA).

PSR J1921+0137

PSR J1921+0137 is the latest discovery in this chapter (2014 March) with a spin period of 2.49 ms and DM of 104.9 pc cm^{-3}, which is the highest among the MSPs in the chapter, a minimum He-WD companion mass of 0.24 $M_\odot$ and an orbital period of 9.9 days. There is no proper motion measurement from the MCMC analysis or pulsar timing for J1921+0137 yet.

PSR J2042+0246

PSR J2042+0246 has the longest orbital period (77.2 days) in this chapter. It has a spin period of 4.53 ms, a DM of 9.27 pc cm^{-3}, and a minimum He-WD companion mass limit of 0.19 $M_\odot$. We measured a significant proper motion of 20.62 ± 1.90 mas yr^{-1} from pulsar timing, which led to a more precise measurement of the intrinsic period derivative, after correcting for the Shklovskii effect, of 11.7×10^{-21}. This pulsar scintillates strongly during observations at 820 MHz due to its low DM, making it often quite difficult to detect.

PSR J2310−0555

PSR J2310−0555 has a spin period of 2.61 ms, a DM of 15.5 pc cm^{-3}, and an orbital period of 1.4 days. This pulsar was fairly challenging to time due to strong scintillation and a huge difference between an original LAT position and true timing position. The pulsar was found with the GBT at 350 MHz and follow-up timing observations were conducted at 820 MHz (the 820 MHz beam FWHM is $16'$ and the 350 MHz beam FWHM is $36'$). However, the follow-up timing observations could not detect the pulsar, despite multiple sets of "gridding" observations designed to determine the pulsar's position more precisely. By using an improved source position from the

3FGL catalog, new 820 MHz observations detected J2310−0555 ∼10.8′ away from the original LAT γ-ray position. In addition, the original position is 9.7′ away from the timing position.

PSRs J0605+3757, J1137+7528, J1855−1436 and J1858−2216

PSRs J0605+3757, J1137+7528, J1855−1436, and J1858−2216 are MSPs with typical He-WD companions with spin period ranges from 2.4 to 3.6 ms and DM ranges from 20.9 to 109.2 pc cm^{-3}. They have a relatively long orbital periods, ranging from 29.2 to 61.2 days. We were unable to measure either $\dot{P}$ from the MCMC analysis nor proper motion from radio timing for these pulsars.

2.4.2 Radio and Gamma-ray Light Curves

This section is contributed by Tyrel Johnson

The radio and the γ-ray components of pulsar emission are believed to originate mostly in different locations in the magnetosphere (Venter et al. 2009). The γ-ray emission mechanism is typically thought to be curvature radiation from particles accelerated along the magnetic field lines in the outer magnetosphere (e.g. Muslimov & Harding 2004; Cheng et al. 1986); however, other models predict an additional synchrotron component (Viganò et al. 2015), that the emission is all synchrotron from the striped pulsar wind (Pétri 2012), or that the emission arises from inverse Compton scattering (Lyutikov et al. 2012). While much is known about pulsar radio emission, the exact mechanism is still being debated. Although it is likely that for MSPs, the radio emission is generated much farther out in the magnetosphere than is thought to be the case for slow pulsars.

By analysing phase differences between radio and γ-ray light curves (LCs), Venter

Table 2.2. The Upper Limit and Measured Proper Motions

PSR	d (kpc)	$\mu_{\rm up}$ (mas yr^{-1})	$\mu_{\rm timing}$ (mas yr^{-1})
J0533+6759	2.4	22	unknown
J0605+3757	0.7	32	unknown
J0621+2514	2.3	40	unknown
J1137+7528	1.5	19	unknown
J1142+0119	0.9	37	105 ± 62
J1312+0051	0.8	46	25.0 ± 1
J1630+3734	0.9	39	16.1 ± 3
J1855−1436	3.1	20	unknown
J1858−2216	0.9	27	unknown
J1921+0137	3.5	30	unknown
J2042+0246	0.8	40	20.6 ± 2
J2310−0555	0.7	33	unknown

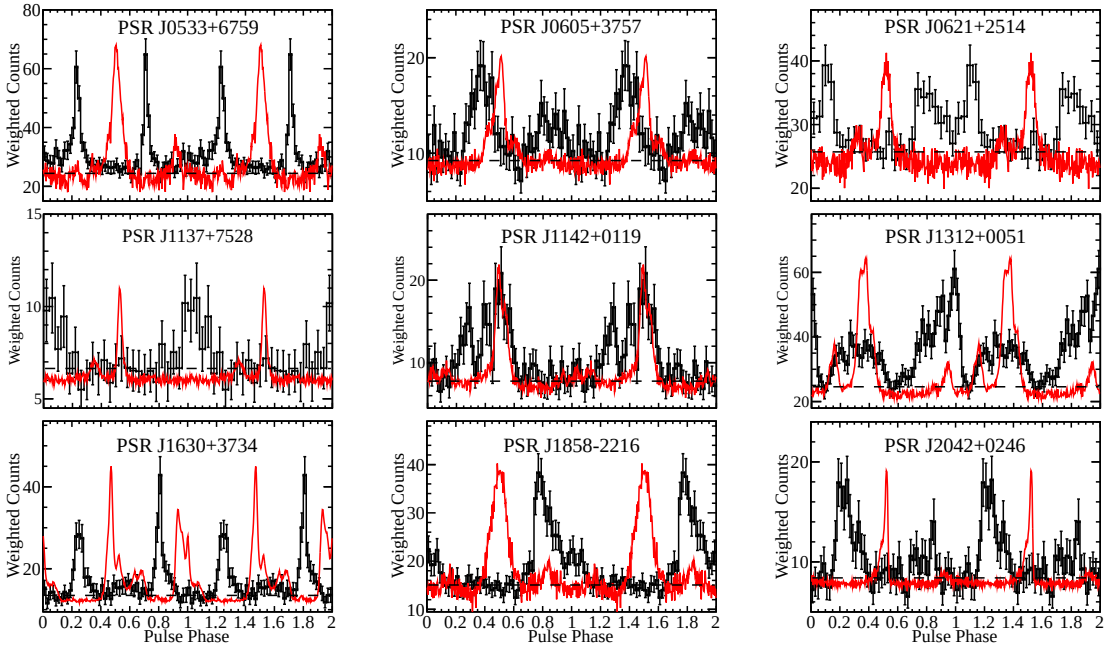

Fig. 2.2.—: The γ-ray and radio light curves of nine MSPs. The radio profiles are summed over detections at 820 MHz while γ-ray light curves correspond to the integrated *Fermi* LAT photons found within 5° of each MSP, and with spectrally and positionally determined photon weights. The horizontal dashed lines are an estimation of the background level.

et al. (2012) and Johnson et al. (2014) divided MSPs into three broad classes. For Class I the γ-ray peak trails the radio peak by < 0.5 in phase, for Class II the radio and γ-ray peaks are aligned (within 0.1 in phase), and for Class III, the γ-ray peak leads (between 0.3 and 0.1 in phase) the radio peak. After fitting various pulsar emission models to the radio and γ-ray MSP LCs, they found that the radio emission of Class I and III MSP most probably originates in the open field region above the polar cap near the stellar surface. The γ-ray emission of Class I MSP comes from narrow vacuum gap near the surface of the last closed field lines. Class III high energy emission is thought to come from the high altitude region above the polar cap. For Class II MSPs, the radio and γ-ray emission are both assumed to originate in the extended altitude region close to the last open magnetic field line.

In our work the γ-ray profiles were folded with the radio ephemerides and the radio delay due to propagation in the ISM was removed. Therefore, the lags between radio and γ-ray profiles are physical. The radio and γ-ray LCs are shown in Fig. 2.2. Note that we only have preliminary γ-ray results for PSRs J1855−1436, J1921+0137 and J2310−0555 so we only present nine MSPs here. The analysis will be completed within the next few months after this thesis. For nine MSPs we performed the preliminary classification by visual examination of the lags between radio and γ-ray LCs. The results are the following:

Class I: PSRs J0533+6759, J0621+2514, J1137+7528, J1312+0051, J1630+3734 and J1858−2216.

Class II: None.

Class III: PSRs J0605+3757, J1142+0119 and J2042+0246

However, a fitting analysis as in Johnson et al. (2014) should be applied to deter-

mine the lags between γ-ray and radio LCs more precisely.

2.4.3 Gamma-ray Pulsations

This section is contributed by Tyrel Johnson

For the twelve MSPs with phase-connected timing solutions, a binned maximum likelihood analysis was performed on a $21.^{\circ}2 \times 21.^{\circ}2$ (the largest square that will fit entirely inside our 15° radius selection) region of interest (ROI), centered on the corresponding radio position, using the `P7REP_SOURCE_V15` instrument response functions (IRFs). To model the ROI for each MSP, we included sources from the LAT 4-year source catalog, 3FGL (Acero et al. 2015), within a 25° radius of the ROI center. All known, extended sources in 3FGL were modeled as such using the same spatial templates. The Galactic diffuse emission was modeled using the `gll_iem_v05r1.fits` spatial template and the isotropic diffuse (including the extra-Galactic γ-ray and residual instrument backgrounds) using `iso_source_v05.txt`[9]

Because of our choice of good time intervals, it was necessary to model the Earth limb emission using the same spatial template and spectral shape as 3FGL. PSRs J0533+6759, J0604+3757, J1142+0119, J1312+0051, J1630+3734, and J1858−2216 were included in the 3FGL catalog as known γ-ray pulsars, but we moved each to their respective radio timing positions in our model, requiring changing the positions by $\leq 0.^{\circ}1$. PSRs J0621+2514, J1137+7528, and J2042+0246 were not known γ-ray pulsars in 3FGL and we thus found the closest sources, moved those to the radio timing positions, and identified them in our model, requiring changing the positions by $\leq 0.^{\circ}04$. In each model, the spectral parameters of point and extended sources within 6°of the ROI center and with test statistic (TS, Acero et al. 2015) values ≥ 50 were

[9]These diffuse models are available for download at
`http://fermi.gsfc.nasa.gov/ssc/data/access/lat/BackgroundModels.html`.

left free, as were the normalizations of the Galactic and isotropic diffuse components. All other source parameters were kept fixed throughout the analysis.

We modeled the spectrum of each MSP as a simple power law (Eq. 2.8) and an exponentially-cutoff power law (Eq. 2.9) with the b parameter fixed to one (a simple cutoff) and free to vary.

$$\frac{dN}{dE} = N_0 \left(\frac{E}{E_0}\right)^{-\Gamma} \tag{2.8}$$

$$\frac{dN}{dE} = N_0 \left(\frac{E}{E_0}\right)^{-\Gamma} \exp\left\{-\frac{E}{E_{\rm C}}^{b}\right\}. \tag{2.9}$$

In Eqs. 2.8 and 2.9, N_0 is a normalization factor with units cm^{-2} s^{-1} MeV^{-1}, Γ is the photon index, and E_0 is a scale parameter in units of MeV, taken as the pivot energy from 3FGL. For PSRs J0621+2514, J1137+7528, and J2042+0246 we used the pivot energy from the closest 3FGL sources that we moved to the radio positions. In Eqn. 2.9, $E_{\rm C}$ is the cutoff energy in units of GeV and b is an exponential index controlling the sharpness of the cutoff.

We then calculated $\mathrm{TS_{cut}} = -2(\ln(\mathcal{L}_{\rm cut}) - \ln(\mathcal{L}_{\rm pl}))$ and $\mathrm{TS_{b\ free}} = -2(\ln(\mathcal{L}_{\rm b\ free}) - \ln(\mathcal{L}_{\rm cut}))$, where $\mathcal{L}_{\rm pl}$ is the maximum likelihood of the power-law fit, $\mathcal{L}_{\rm cut}$ is the maximum likelihood of the cutoff fit with $b = 1$, and $\mathcal{L}_{\rm b\ free}$ is the maximum likelihood of the cutoff fit with the b parameter free to vary. In each case, there is one additional degree of freedom, allowing us to use the likelihood ratio test to approximate the rejection of the power law in favor of the simple exponential cutoff as $\sim \sqrt{\mathrm{TS_{cut}}}$ and the rejection of the simple cutoff in favor of the b-free fit as $\sim \sqrt{\mathrm{TS_{b\ free}}}$.

The best-fit results for each MSP are given in Tables 5.1, 5.2, 5.3, 5.4, and 5.5. For all but PSR J1137+7528, the power-law spectrum was rejected in favor of the simple cutoff at $\gtrsim 4\,\sigma$. The b-free fit was never significantly preferred over the simple exponential cutoff (always $\lesssim 2\,\sigma$). For PSR J1137+7528, the power-law shape can

not be significantly rejected in favor of a simple exponential cutoff and thus we only report values for and derived from the power-law fit. For each MSP we provide the spectral parameters and point-source TS from the best fit, the values of TS_{cut} and $TS_{b\ free}$, and the integrated photon (F) and energy fluxes (G) from 0.1 to 100 GeV are derived from the best fit.

As estimated by (Ackermann et al. 2012), the systematic uncertainties on the LAT effective area (A_{eff}) are 10% for $\log_{10}(E/1\ \mathrm{MeV}) \leq 2$, 5% for $\log_{10}(E/1\ \mathrm{MeV}) = 2.75$, and 10% for $\log_{10}(E/1\ \mathrm{MeV}) \geq 4$ with linear extrapolation, in log space, in between. Following Abdo et al. (2013), we estimate the effects of these uncertainties on our derived spectral parameters by generating bracketing IRFs using a modified A_{eff} given by,

$$A_{brack}(E,\theta) = A_{eff}(E,\theta)(1 + err(E)B(E)), \tag{2.10}$$

where $err(E)$ represented the systematic uncertainties noted previously and the bracketing functions we used were $B(E) = \pm 1$ to estimate systematic uncertainties on N_0 and $B(E) = \pm\tanh(\log_{10}(E/E_0)/0.13)$ to estimate systematic uncertainties on both Γ and E_C. For the latter bracketing functions, we generated bracketing IRFs specifically for each MSP using E_0 from the four-year source list. In order to estimate the systematic uncertainties on the photon and energy fluxes, we recalculated these values from each bracketing IRFs fit and took the maximum excursions from the nominal values.

When fitting with the bracketing IRFs, we generated new source maps files[10] for the free point sources in each region of interest with the bracketing IRFs and used the source maps for the fixed sources and the diffuse backgrounds calculated with the P7REP_SOURCE_V15 IRFs. This was done as the diffuse backgrounds are

[10]For more information on source maps files for use with LAT binned likelihood analysis see `http://fermi.gsfc.nasa.gov/ssc/data/analysis/scitools/binned_likelihood_tutorial.html`.

specific to the LAT data and nominal IRFs and the spectral values of the fixed sources correspond to the same IRFs.

In order to get the best γ-ray pulse profiles possible, we extended the data set to 2015 June 24, the end of the P7REP data, for the timing analysis. We selected events in this time range with reconstructed directions within 5°of each MSP and used the best-fit spectral model to calculate the probability for each event to be associated with that particular MSP. We then folded the events at the radio period using the `fermi` plugin (Ray et al. 2011) for the TEMPO2 timing software (Hobbs et al. 2006) and calculated the spectrally-weighted H-test significance (Kerr 2011), resulting in a $> 5\,\sigma$ pulsed detection for each MSP. The uncertainties for each bin of the γ-ray light curve and the background level are calculated as described in Guillemot et al. (2012) and Abdo et al. (2013). Pulsed statistics for each MSP are given in Tables 5.1, 5.2, 5.3, 5.4, and 5.5.

2.5 Discussion

2.5.1 Radio and γ-ray Flux Densities

In the early searches for pulsars in *Fermi* unassociated sources, the bright sources with pulsar-like spectra were intensively searched with various radio telescopes and yielded many discoveries of MSPs (e.g. Ransom et al. 2011, Kerr 2011). However, from the more recent searches, some bright radio MSPs were found in fainter *Fermi* unassociated sources (e.g. Bhattacharyya et al. 2013). These detections suggest that there may be no, or only weak correlations between the flux of the pulsars and the γ-ray sources. With additional 12 γ-ray MSPs in this chapter, we have more samples to investigate the correlation between radio flux densities and energy fluxes of γ-ray

MSPs.

Figure 2.3 is a plot of *Fermi* γ-ray MSPs, showing radio flux densities at 1400 MHz against γ-ray energy fluxes from photons with energies above 100 Mev. The pulsars on the plot are from the second γ-ray pulsar catalog (2PC) (Abdo et al. 2013), another *Fermi*unidentified source analysis (Camilo et al. 2015) and the new GBT *Fermi* MSPs in this chapter. For MSPs with flux-calibrated data, we used those values as starting points. If they had no flux calibration measurements, we used the radiometer equation to calculate flux densities at 820 MHz. Then, we extrapolated the 1400 MHz flux densities from the flux density estimates at 820 MHz using the relation $S_f \propto f^{\alpha}$, where α is the spectral index. We adopted a spectral index of -1.41 from the latest study of the distribution of pulsar spectral indices (Bates et al. 2013). Furthermore, we adopted γ-ray energy fluxes from the third *Fermi* LAT source catalog (3FGL) (Acero et al. 2015). Figure 2.3, shows no correlation between the radio and γ-ray fluxes and suggests that faint LAT unassociated sources are as reasonable MSP candidates as the bright ones. Additionally, it shows that the new GBT *Fermi* MSPs are among the faintest γ-ray *Fermi* MSPs detected in the radio. This emphasizes the high sensitivity of the GBT in discovering faint MSPs.

2.5.2 Galactic Plane Searches with S-band

Young and energetic pulsars are believed to be the primary γ-ray emitters near the Galactic plane. We have observed 22 pulsar-like Galactic plane sources and found no new pulsars. The unsuccessful searches in the plane are not completely unexpected. As discussed in Abdo et al. (2013), the poor success rate of radio searches near the Galactic plane is probably due to the combination of smaller radio beam sizes in young pulsars compared to MSPs (and to γ-ray beams) and the intensive radio

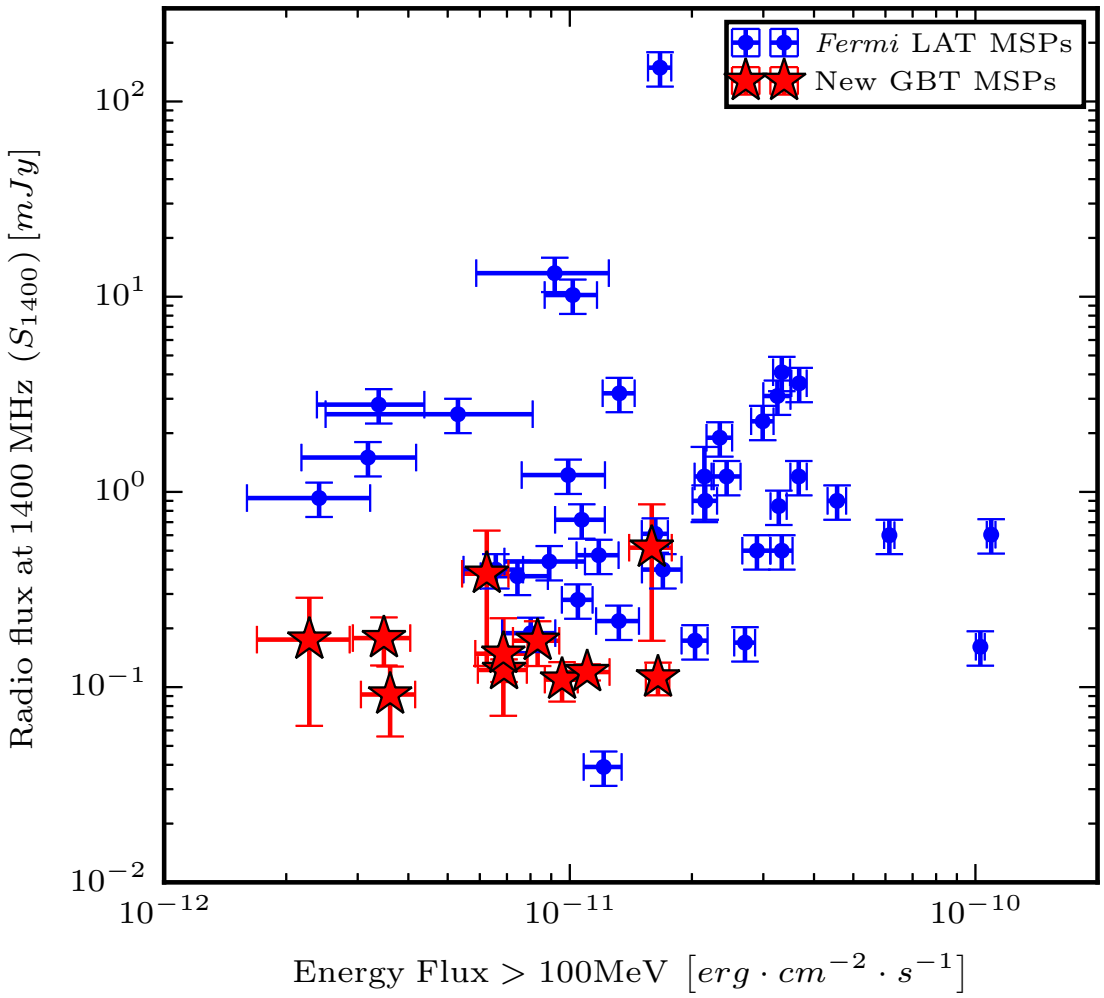

Fig. 2.3.—: A plot of radio flux density vs γ-ray flux for the MSPs from the Second Pulsar Catalog (2PC) (Abdo et al. 2013) and the new GBT MSPs. The lack of any correlation between the radio and gamma-ray fluxes likely explains much of the continuing success of the radio MSP searches of *Fermi* unassociated sources, and suggests that many more MSPs are waiting to be found based on even a very weak γ-ray signature.

searches of previous pulsar surveys. In addition, the large 95% error regions of most *Fermi* unassociated sources are more confused in the crowded regions of the Galactic plane, and are significantly larger than the GBT's S-band beam width of 6-arcmin. To cover an entire γ-ray error region, we have to perform multiple short-time gridded observations on most sources which reduces the search sensitivity. It is also possible that pulsars in the field may have steep spectral indices.

2.5.3 Single-Pulse Searches

We found no individual pulses from any of the 198 sources. As discussed in Deneva et al. (2009), the intermittency ratio, the measurement of the efficiency to detect objects by single-pulse search over periodicity search, for MSPs is small. Additionally, all the MSPs on this chapter are not close to the known giant pulse (GP, an occasional intense short-duration burst) emitters as shown on Figure 2.4, the $B_{LC} - \dot{E}$ correlation (Knight 2006). This and the fact that GP emission is likely rare among the MSP population, largely explains why single-pulse searches are not successful towards LAT unassociated sources.

2.5.4 LAT γ-ray Detection Threshold

Abdo et al. (2013) discuss the prediction that a metric for γ-ray luminosity is related to spin-down luminosity and distance by $\propto \sqrt{\dot{E}}/D^2$. Despite the unreliable distances from the NE2001 model and/or Galactic background confusion from some pulsars, the detectability metric threshold of approximately $10^{16}\,(\mathrm{erg}\cdot\mathrm{s}^{-1})^{\frac{1}{2}}\cdot\mathrm{kpc}^{-2}$ appears to be a good prediction for LAT pulsation detection. Figure 2.5) shows that PSR J2310−0555 falls slightly below the threshold but the rest of the MSPs are above the detectability threshold.

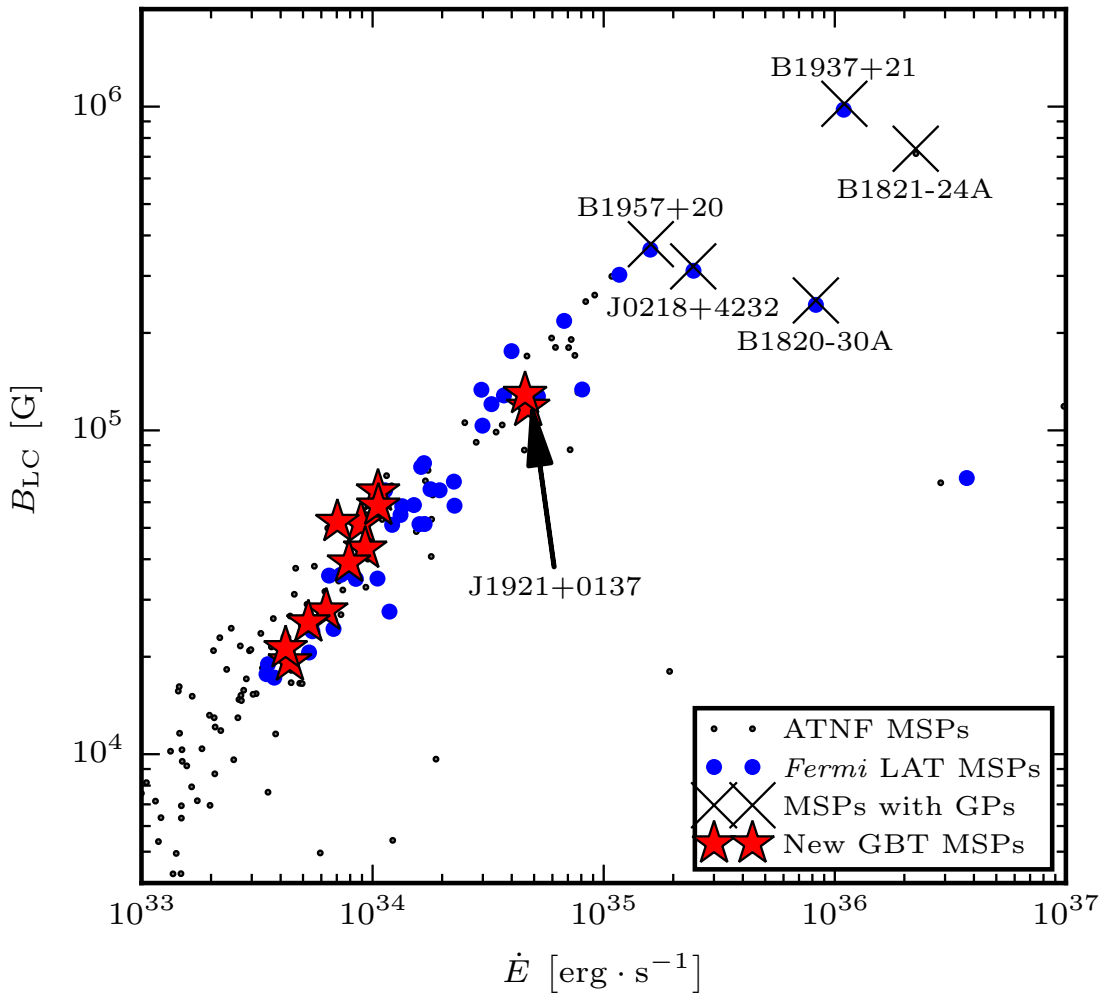

Fig. 2.4.—: The correlation between magnetic field strength at the light cylinder (B_{LC}) and spin down luminosity ($\dot{E}$) of MSPs, with giant-pulse emitters shown as crosses.

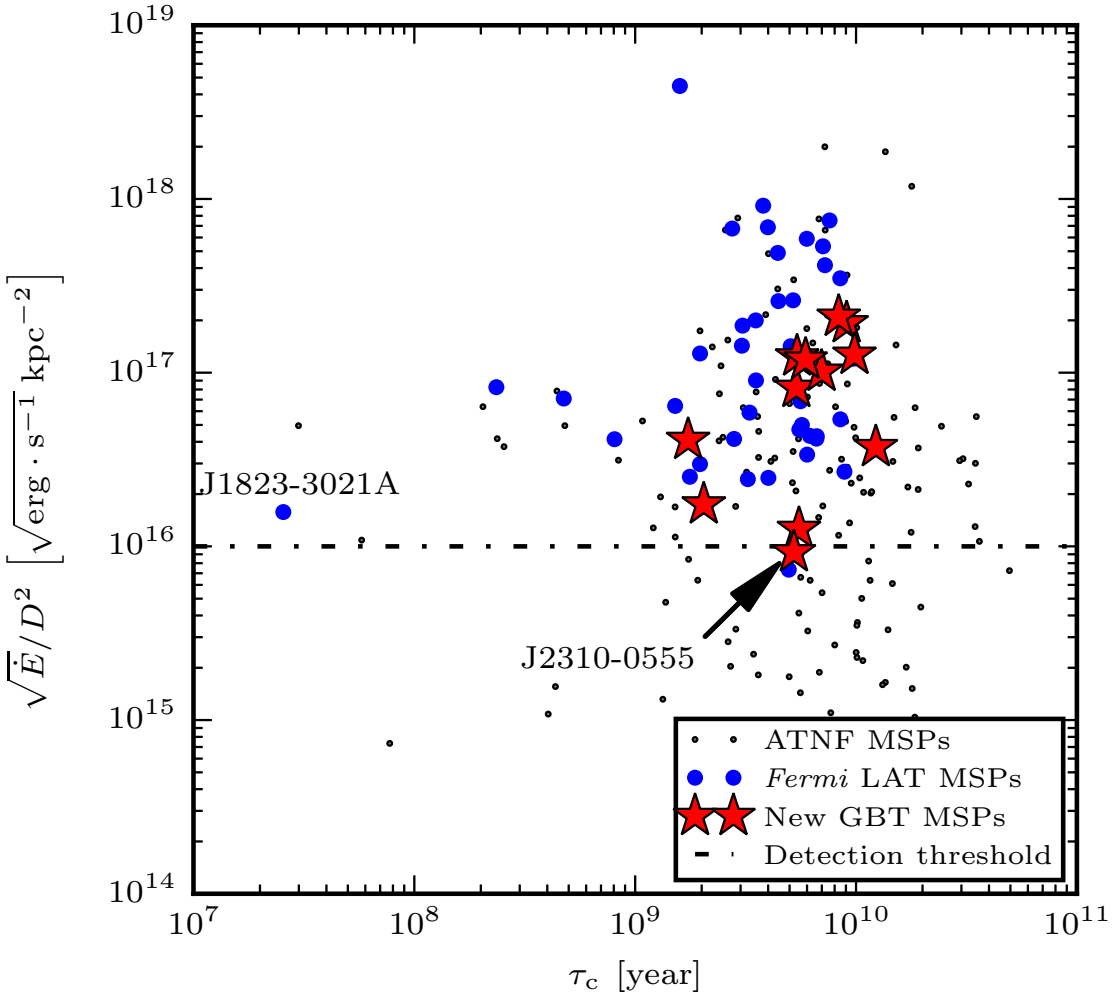

Fig. 2.5.—: $\sqrt{\dot{E}/D^2}$ versus characteristic age of ATNF MSPs, LAT MSPs, and the twelve new MSPs described here. The dashed line is a γ-ray detection threshold at $10^{-16}\,(\mathrm{erg\cdot s^{-1}})^{\frac{1}{2}}\cdot\mathrm{kpc^{-2}}$. The plot shows PSR J1823−3021A, the most γ-ray luminous and youngest MSP to date (Freire et al. 2011).

2.5.5 Orbital Period and Companion Mass Relation

This section is contributed by Scott Ransom

MSPs in binary systems are thought to evolve from low-mass X-ray binaries (LMXBs), where the neutron star accretes mass and angular momentum from the companion star (Alpar et al. 1982). The mass transfer process in the system initiates when the donor star evolves up to the red giant branch (RGB), expands to fill its Roche lobe, and stellar materials overflow onto the neutron star through an accretion disk. Based on previous studies of LMXBs with low-mass ($<2\,M_{\odot}$) main-sequence donors (e.g. Webbink et al. (1983); Joss et al. (1987); Rappaport et al. (1995)), Tauris & Savonije (1999) derived a relationship, hereafter called TS99, which predicts degenerate He-core white dwarf (He-WD) companion masses from the final orbital period of "normal" (final orbital period $\gtrsim$1-2 days) binary MSPs.

Accurately measuring companion masses is difficult. Since TS99 was introduced, some fairly precise measurements of He-WD companion masses from either Shapiro delay (via pulsar timing, e.g. PSR J1909-3744, Jacoby et al. (2005); PSR J0437−4751, Verbiest et al. (2008)) or modeling of optical properties of the companion stars (e.g. van Kerkwijk et al. (2005); Kaplan et al. (2014)) have supported the TS99 correlation (e.g. Tauris & van den Heuvel (2014)). Recently, *Fermi* and other pulsar surveys have significantly increased the number of known Galactic MSP binaries. By statistically analyzing the binary MSP orbital parameters, we can constrain the He-WD companion masses and therefore test TS99 and/or assumptions about the orbital inclination angle distribution.

For the analysis, we have primarily gathered Galactic MSPs with He-WD companions from the Australian Telescope National Facility (ATNF) pulsar catalog version

1.52[11] (Manchester et al. 2005), as well as *Fermi* MSPs from this and two other recent papers. From the ATNF catalog, we selected only those pulsars unassociated with globular clusters (parameter *assoc* $\neq$ "GC"), have a short spin period (parameter $P_0 < 30\,\mathrm{ms}$), and that have a He-WD companion (parameter $BinComp =$ "He"). We also included pulsars where $MinComp =$ "unknown" with minimum companion mass $< 0.4\,M_\odot$. These pulsars are likely to have a He-WD companion rather than a heavy CO-WD companion. We explicitly excluded known "redback" pulsars, whose companions are non-degenerate and have not yet evolved into He-WDs. These pulsars are listed in Ray et al. (2012) and Roberts et al. (2015). We also ignored J1933−6211, which requires a pulsar mass $<1\,M_\odot$to be consistent with TS99. In addition to the ATNF pulsars and the 12 binary MSPs in this chapter, we have included 7 new *Fermi* MSPs from the PSC: 4 from Parkes (Camilo et al. 2015) and 3 from the GBT observations at 350 MHz (Bangale et al. 2015, in prep). This brings the total number of pulsars in the following analysis to 81.

Figure 2.6 shows the TS99 relation for the 81 Galactic MSPs described above, plus an additional five which have orbital periods shorter than one day For this plot we have assumed a pulsar mass (M_p) of $1.48\,M_\odot$ as suggested by Özel et al. (2012), for the mean of the recycled neutron star mass distribution. With this assumption, 76 of the 81 MSPs have companion mass ranges consistent with the TS99 relation. There are several possible explanations for the five MSPs which are inconsistent with the TS99 relation, as discussed in Guillemot & Tauris (2014). For example, they may have evolved from binary systems other than LMXBs (i.e. intermediate mass X-ray binaries (IMXBs)), or they may simply have pulsar masses that differ significantly from $1.48\,M_\odot$.

A common assumption when investigating binary pulsars and their correspondence

[11] `http://www.atnf.csiro.au/people/pulsar/psrcat/`.

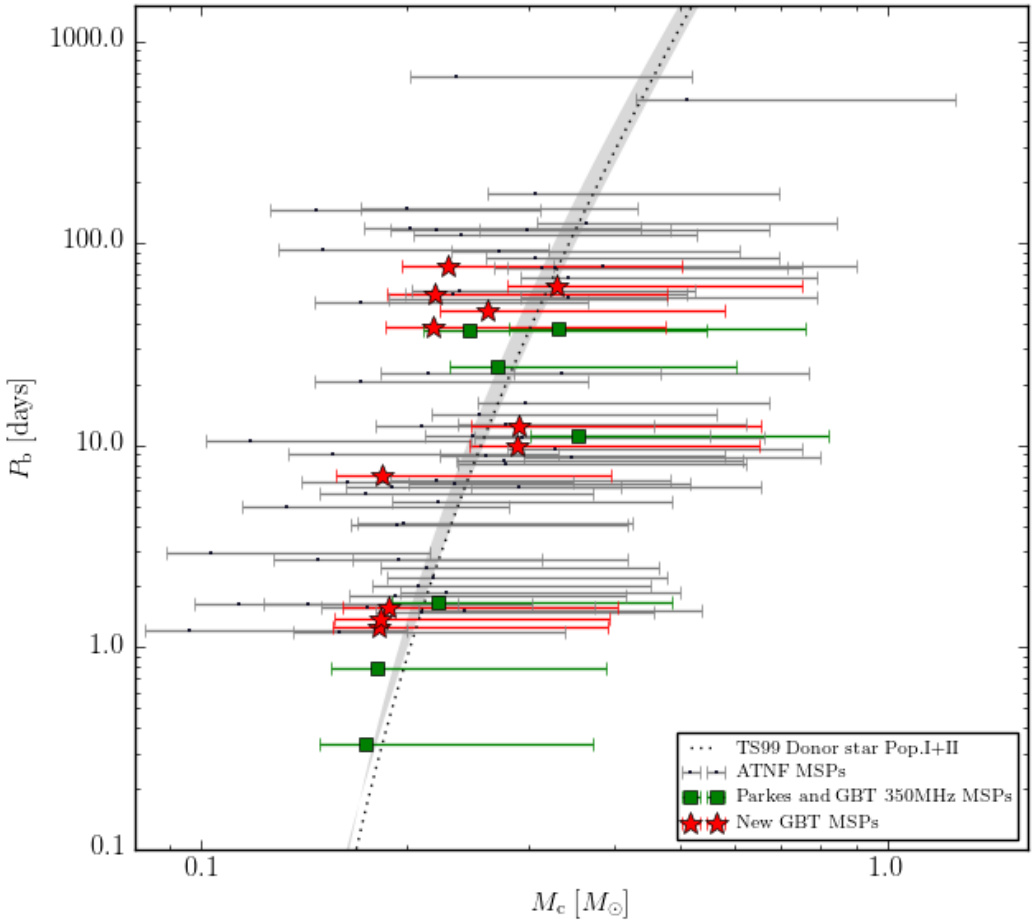

Fig. 2.6.—: A plot of TS99 relation with Galactic MSPs. The width of the relation is calculated from the Pop. I donor star relation (metallicities $Z = 0.001$) and the Pop. II donor star (metallicities $Z = 0.02$) relation. The dotted line shows the relation for Pop. I and Pop. II donor stars. Note that TS99 becomes uncertain for pulsars with $P_b < 1$ day (dashed line). The data points show the median companion mass ($i = 60°$ assuming $M_p = 1.48\ M_\odot$), while the lower and upper limits correspond to the minimum companion mass with $i = 90°$ and a 90% confidence (assuming random orbital inclinations) maximum companion mass with $i = 25.84°$.

with the TS99 relation is that orbital inclinations are distributed randomly, meaning that probability density is uniform or flat in $\cos i$. Stairs et al. (2005) and Smedley et al. (2014) examined this assumption by investigating binary MSPs with He-WD companions available at that time and found that the $\cos i$ corresponding to the $P_b - Mc$ correlation is randomly distributed, as one might expect, if all pulsar masses are roughly $1.75 \pm 0.04\,M_\odot$.

Using our much larger sample of binary MSPs we can also check the assumption of random orbital inclinations for binary MSPs. We can assume that TS99 is correct for He-WD MSP systems and then look at the resulting distribution of inferred inclinations. If pulsar orbits are randomly distributed and TS99 is correct, then $\sim 50\%$ of the predicted median companion masses (i.e. those computed with $i = 60^\circ$) should lie above the TS99 relation while the other 50% should lie below. However, we found that 56 out of 81 pulsars ($\sim 69\%$) fall below the TS99 relation (using Pop. I and Pop. II donor stars) when assuming all pulsar masses are $1.48\,M_\odot$. The binomial probability for 56 or more out of 81 median masses to fall below the TS99 prediction, assuming an intrinsic probability of 50%, indicates that this would occur by chance only $\sim 1.6 \times 10^{-4}$ of the time. The low binomial probability could suggest that TS99 is incorrect and/or that observed pulsar orbits are not randomly distributed. However, it is crucial to note that this number changes if we assume different pulsar masses (i.e. TS99 results in a flatter $\cos i$ distribution if we assume all pulsar masses are higher). This statement is supported by previous studies by Stairs et al. (2005) and Smedley et al. (2014). They examined the $\cos i$ distribution of binary MSPs with He-WD companions available at the time, and found (for $\cos i$ corresponding to the $P_b - Mc$ relations) that a large ($\sim 1.75\,M_\odot$) assumed pulsar mass yielded fairly flat $\cos i$ distributions. However, we know that pulsar masses are not all the same, and

so assuming constant pulsar masses in these analyses is potentially problematic.

In order to test TS99's predictions with a more realistic distribution of pulsar masses, we performed a simple Monte Carlo analysis using the 81 pulsars described above. We ran 10,000 iterations where we randomly selected each pulsar mass from the Özel et al. (2012) normal distribution ($1.48 \pm 0.21 \ M_{\odot}$) for recycled pulsars, such that every MSP system becomes consistent with TS99. Given TS99's predicted companion mass and the randomly drawn pulsar mass, the mass function determines the inclination of each system,

$$f(m_p, m_c) = \frac{4\pi^2}{G} \frac{(a \sin i)^3}{{P_b}^2} = \frac{(m_c \sin i)^3}{(m_p + m_c)^2}, \tag{2.11}$$

where G is the Newton's gravitational constant. For pulsars with known inclinations and companion masses, we used the known values: J0337+1715a (Ransom et al. 2014), J1713+0747, B1855+09, J1909−3744 (The NANOGrav Collaboration et al. 2015), and J0437−4715 (Verbiest et al. 2015, in prep).

Figure 2.7 shows the histogram of $\cos i$ from the statistical simulations, which indicates that the distribution is not uniform, but favors larger $\cos i$ (i.e. lower inclinations) in general. A KS-test comparing the simulated $\cos i$ distributions with a uniform distribution yields a median p-value of 1.1×10^{-4}, suggesting that we can reject a random inclination hypothesis at $\sim 0.01\%$ confidence ($\sim 3.7\sigma$). Approximately 95% of the 10,000 simulation trials resulted in p-values smaller than 0.002.

These results suggest that we may be preferentially observing MSPs with more face-on orbits. Perhaps MSP radio emission, which is certainly a wide fan beam given the number of MSPs with both radio and gamma-ray emission, is more concentrated near the spin axes of the pulsars (i.e. nearly aligned rotators assuming the magnetic field is aligned with the spin angular momentum), which we expect to be aligned with

the orbital angular momentum due to accretion during the recycling process. Future emission studies, perhaps using radio polarization information and γ-ray emission modelling, may be able to investigate this aligned-emission hypothesis.

If our analysis is correct, and TS99 applies to these systems, we can make predictions about the properties of some of the MSPs. The analysis indicates that three MSPs should have low-mass neutron stars, with J1400−1438 having m_p <1.28 $M_\odot$, and both J1125−6014 and J1903−7051 having m_p <1.16 $M_\odot$. Similarly, the analysis suggests that five of the MSP systems (J1643−1224, J1748−3009, J1653−2054, J2229+2643, and J1841+0130) each have i <30° at 95% confidence. Interestingly, Fonseca et al. (in prep.) has come to a similar conclusion about J1643−1224 (i <37°) based on the lack of detection of Shapiro delay in that system. Also note that while the overall indications are for more face-on orbits, in general, there seems to be no evidence for pulsars with extremely face-on orbits (e.g. $i \lesssim 15°$).

2.6 Conclusion

We report the discovery of twelve new MSPs from radio searches of *Fermi* LAT unassociated sources with the GBT. We have established phase-connected timing solutions for all twelve, and have detected γ-ray pulsations from each. We used a new MCMC gamma-ray timing technique to provide better measurements of $\dot{P}$ and proper motion due to the longer time span of the LAT γ-ray data. We also investigated 20 LAT sources near the Galactic plane in order to search for young pulsars, yet found no new pulsars there. The twelve new MSPs with timing solutions improve our knowledge of several aspects of the MSP population. Radio flux densities and γ-ray fluxes for γ-ray MSPs are currently almost completely uncorrelated, suggesting that we may yet find bright radio pulsars in faint γ-ray sources. We also investigated the

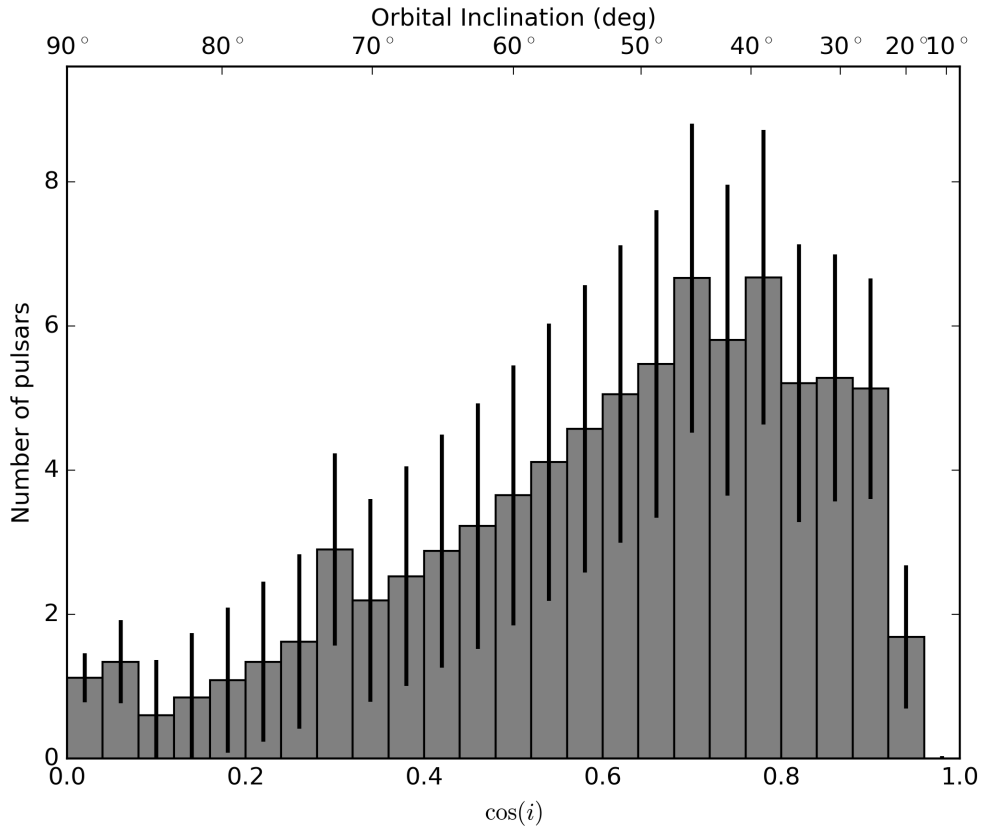

Fig. 2.7.—: For pulsar masses randomly selected from a normal distribution appropriate for recycled neutron stars ($1.48 \pm 0.21\,M_{\odot}$, based on Özel et al. 2012), we calculated corresponding companion masses which make the systems consistent with the TS99 relation, and thereby also determined the orbital inclinations of the systems. The histogram shows the distribution of $\cos i$ from 10,000 iterations of these simulations, with the vertical black bars being the ± 1-σ variation in each bin. The distribution is not flat as would be expected from random orbital inclinations (see §2.5.5).

$P_b - M_c$ relation of pulsars with He-WD companions and found that the distribution of binary inclination angles may not be distributed randomly, but instead prefers lower inclinations (higher $\cos i$).

Chapter 3

Four New Pulsars in Tight Orbits

3.1 "Spider" Pulsars

Millisecond pulsars (MSP) in compact binary systems are fascinating objects to study. At the present time, two types of compact binaries are known: the pulsar wind may be ablating away the companion or the pulsar may accrete mass from the companion, with the companion being gradually destroyed in both cases. Such cannibalistic behaviour suggested the arachnid nicknames for these types of systems: "Black Widows" (BWs) and "Redbacks" (RBs) respectively (it is a common practice to refer both to MSPs and to MSP+companion systems as BWs or RBs). BWs are rotation-powered MSPs in compact circular orbits with short orbital periods on the order of hours and very low mass companion ($\sim$ 0.01-0.05 $M_{\odot}$). RBs are similar systems, but with heavier non-degenerate companion of $\sim$ 0.1-0.4 $M_{\odot}$. See Fig. 3.1 for an artist's impression of RBs and BWs.

BWs and RBs are thought to represent an important stage in pulsar evolution. In 1988 Fruchter et al. discovered the first known BW, B1957+20, and suggested that the isolated MSPs are formed from BWs after the pulsar wind completely evaporates

the companion. The discovery of binary pulsars with extremely small companions, which are possibly ablated away by pulsar winds, (i.e. the pulsar planets Wolszczan & Frail 1992) are indirect evidence for this scenario. However, Chen et al. (2013) demonstrated that it is difficult to produce the isolated MSPs from the BWs on a Hubble time scale. Thus, the evolutionary link between BWs and isolated MSPs remains unclear.

The discovery of the RB "missing link" system, PSR J1023+0038, brought evidence of back and forth transitions between Low Mass X-ray Binary (LMXB) states and radio pulsar states (e.g. Archibald et al. 2009; Papitto et al. 2013). RBs are therefore suggested to be the links between the accretion-powered X-ray pulsars and the rotation-powered radio pulsars.

The materials expelled from the companion often hinder the detection of pulsar emission. The eclipse mechanism is still unknown but is thought to be caused by either absorption or dispersive smearing of the radio waves (Thompson et al. 1994). While the absorption process, based on the interaction between the radio emission and the ejected material, decreases observed total flux density, the smearing process does not diminish the *unpulsed* flux density. It instead distorts its pulsed component. Smearing can be caused by the rapid DM variation in the ionized region of the companion which slightly increases the total line of sight electron column density. MSP detection is very sensitive to changes in the DM, so even a minimally altered DM could result in a non-detection of the pulsar.

Besides the main radio eclipse, happening around the inferior conjunction, the unbound plasma can also cause short irregular eclipses at random orbital phases. This is a distinctive phenomenon of BW and RB systems. Sometimes, immediately before and after the eclipse (for both regular and irregular eclipses), an increase in

the DM is observed, indicating that the line of sight passes directly through the intrabinary plasma.

For the BW and RB systems, an intrabinary shock may have formed between the pulsar and the companion at the location where pulsar-wind pressure balances with the wind pressure from the companion. The so-called pulsar-wind shock (pulsar wind nebulae) can be the source of high-energy (X-ray or γ-ray) emission modulated at the orbital period (e.g. Dubus 2015; Huang et al. 2012) in addition to pulsations from the pulsar itself.

Prior to the launch of *Fermi*, most BWs and RBs known resided in globular clusters (e.g. Ransom et al. 2005; Hessels et al. 2007). The Galactic BWs and RBs were the rare systems; only one RB (Chakrabarty & Morgan 1998) and three BWs were known (Johnston et al. 1992; Fruchter et al. 1988; Lundgren et al. 1995; Stappers et al. 1996, respectively). The radio searches of *Fermi*-LAT unassociated sources have so far revealed 15 new BWs and 9 new RBs, which now bring the total number of these systems to 28 (and counting) (Grenier & Harding 2015). Despite the dramatic seven-fold increase, the number of BW and RB systems known is still not large and there is plenty of room for new discoveries within the sample of unidentified *Fermi* sources. As more RB and BW systems are discovered, we will better understand the stages of pulsar evolution, explore the intricate interaction between pulsar emission and the intrabinary plasma and, in general, learn more about this exotic part of the pulsar population.

3.2 Observation and data analysis

The goal of GBT's AGLST14A_480 project (PI Sanpa-Arsa) was to search for new radio MSPs within the internal *Fermi* LAT 4-year pulsar-like source catalog (now

3FGL). The observations were conducted during year 2014, in the same manner as described in Chapter 2. Thus, here I will give only a brief summary of the observing setup.

In total, 68 sources were observed. Depending on the source location and the size of the 95 % position error box, either the 350 MHz- or 820 MHz-centered GBT receiver was used. The sources with Galactic latitude ($|b|$) between 2° and 5° and with position error boxes smaller than 16′ can be observed with a single 820-MHz pointing (16′ GBT beam FWHM at 820 MHz). The sources above Galactic plane ($|b| > 5°$) and with error box smaller than 36′ were observed with the GBT's 350-MHz receiver (FWHM of 36′). Using lower frequencies allowed us to explore sources with less precise positions, but this method cannot be used for the low-latitude candidates because of the sharp rise of the sky temperature in the Galactic plane at lower observing frequencies ($T_{\rm gal} \sim \nu^{-2.55}$, Lawson et al. 1987).

The data were recorded with the Green Bank Ultimate Pulsar Processing Instrument (GUPPI) backend in search mode (DuPlain et al. 2008) and then processed offline. The processing steps included RFI removal, dedispersion, acceleration and periodic pulsar searches (see Chapter 2 for details). In addition, we performed single-pulse search on each source.

Upon discovery, the follow-up observations were scheduled in order to obtain TOAs and refine pulsar ephemerides, using the GBT at 820 MHz and GUPPI. For PSR J1513−2550, we acquired additional extended timing observations with the Nançay telescope at 1.48 GHz using the NUPPI backend with 1024 channels over 512 MHz bandwidth. Once timing solution had been firmly established, we used it to search for the γ-ray-pulsations from the same source.

Throughout this chapter, we count the orbital phase clockwise from the ascending

node. This implies that orbital phase is 0.25 when the companion is between the pulsar and the Earth (inferior conjunction). This is the phase where eclipses are expected to happen.

3.3 Results

3.3.1 Pulsar timing

We were able to phase-connect the four new MSPs with the follow-up observations spanning over 2.3 years using the GBT and the Nançay telescope. We found that PSR J1622−0315 and J2017−1614 are likely to exhibit γ-ray pulsation and have optical counterpart. J1622−0315 and J2155+5448 shows notable flux variation in many observation. We also were able to measure the proper motion of J1622−0315. The residual plot of the three MSPs are shown in Fig.3.2.

Three MSPs (PSRs J1513−2550, J2017−1614 and J2115+5448) were best-fit with the ELL1 binary model (see Table5.8), which indicates a circular orbit (the eccentricity is negligible). They have not had proper motion measurements from pulsar timing yet; therefore a purely kinematic contribution to the observed period derivative ($\dot{P}_{\rm obs}$), known as the Shklovskii effect ($\dot{P}_{\rm Shk}$) [1], cannot be computed yet. This means that the physical parameters $\dot{E}$ and B of the pulsar, which depend on $\dot{P}$, are currently upper limits.

PSR J1622−0315, a new RB, on the other hand, is best-fit with the BTX binary model (see Table 5.9), which allows multiple derivatives of the orbital frequency to be included in the timing model. The proper motion is measured with sufficient significance and consequently yields the $\dot{P}_{\rm Shk}$ of 17×10^{-21}. This value is, however,

[1] $\dot{P}_{\rm Shk} = \mu^2 P d/c$, where μ is the pulsar proper motion, P is the spin period, d is the distance to the system, and c is the speed of light

higher than the $\dot{P}_{\rm obs}$ of 11.6×10^{-21}. This implies that the DM-derived distance (d) is likely overestimated resulting in the overestimation of $\dot{P}_{\rm Shk}$.

3.3.2 The new MSPs

PSR J1513−2550

PSR J1513−2550 is a millisecond pulsar with spin period of 2.12 ms, DM of 47.12 pc cm^{-3}, orbital period of 4.3 hours and minimum companion mass of 0.02 $M_{\odot}$. It is in a tight orbit with very low companion mass ($\geq 0.02\,M_{\odot}$) and exhibits eclipses in some observations. J1513−2550 is therefore considered a black widow pulsar. See Fig. 3.3 for the discovery plot.

PSR J1513−2550 is a very bright MSP with a mean flux density at 820 MHz of ~ 2 mJy. In general, bright MSPs with narrow pulse profiles like PSR J1513−2550 yield high quality TOAs and, therefore, small timing residuals of order μs. They are excellent candidates for pulsar timing arrays (PTAs) which aim to detect gravitational waves; for instance, the North American Nanohertz Observatory for Gravitational Waves (NANOGrav), the European Pulsar Timing Array (EPTA), and the Parkes Pulsar Timing Array (PPTA) (see Hobbs et al. (2010) for a review). Normally, BWs and RBs exhibits orbital period variations over time; therefore orbital frequency derivatives are usually required for BWs and RBs timing. Adding more parameters, however, reduces sensitivity to gravitational waves, so including BWs and RBs into PTAs is potentially troublesome. However, the lost of phase connection due to orbital period variability only happens in RBs. The orbital period change of BWs is slow enough that we can still keep them phase connected. In addition, Bochenek et al. (2015) showed that for fast, strong, narrow-pulsed and non-eclipsing BWs, fitting for the orbital period derivatives reduces less than 5% of the gravitational wave sensi-

tivity. They recommended using these suitable BWs in the PTAs. Unfortunately, J1513−2550 shows strong and irregular radio eclipses; thus, it is likely not suitable for the PTAs.

PSR J1622−0315

PSR J1622−0315 has a spin period of 3.86 ms, DM of 21.4 $\mathrm{pc\,cm^{-3}}$, orbital period of 3.9 hours, minimum companion mass of 0.1 $M_\odot$, and shows strong and irregular eclipses. PSR J1622−0315 can therefore be classified as a redback system. See Fig.3.4 for the discovery plot. The orbital frequency derivative is significantly measured at $1.57(7) \times 10^{-19}$ $\mathrm{Hz\,s^{-1}}$ which indicates the orbital period changes with time due to classical effects from the main sequence companion star. This pulsar eclipses for nearly half of the orbit and when it is "on", it displays significant flux density variability due to diffractive scintillation in most observations. It additionally exhibits smaller short-duration eclipses during some observing sessions (see Fig. 3.13).

With the precise pulsar ephemeris, we folded the *Fermi* LAT photons and found a plausible γ-ray pulsation at 6.9σ. However, we still need to improve the ephemeris in order to assert the pulsation. We also identified a star from the Sloan Digitized Sky Survey (SDSS) at the position of the pulsar as the optical counterpart. In addition, we fold data from R-band images obtained at the Hiltner 2.4-m Telescope of the Michigan-Dartmouth-MIT (MDM) Observatory on June 2016 and found that the photometric light curve shows sinusoidal variations (Jules Halpern, private communication). The variation is consistent with ellipsoidal distortion from a companion that is overflowing its Roche lobe. Such ellipsoidal distorion leads to two maxima and two minima per orbit on the light curve (see Fig. 3.5). The maxima occur equally at phases 0.0 and 0.5 when the tidally distortion of a companion is largest, whereas the

minima occur unequally at phases 0.25 and 0.75. The inequality is due to the fact that the inner Lagrangian point (L1) of a companion viewing at phase 0.75 encounters larger effect of limb and gravity darkening; therefore flux at phase 0.75 is lower in magnitude (Li et al. 2014). The optical variation validates the astrometric position and orbital frequency derivative measurement from pulsar timing.

PSR J2017−1614

PSR J2017−1614 is another black widow pulsar with spin period of 2.31 ms, DM of 25.44 pc cm^{-3}, orbital period of 2.3 hours, and minimum companion mass of 0.03 $M_{\odot}$. See Fig. 3.6 for the discovery plot. With a relatively weak radio signal and broad pulse profile, PSR J2017−1614 has quite poor timing precision (Fig. 3.2), with timing RMS of 17 μs.

By folding LAT γ-ray photons with the timing ephemeris of PSR J2017−1614, γ-ray pulsations with a significance of 5.7 σ were found (see Fig. 3.7). The detection is relatively weak but may be improved with an updated ephemeris. We also found a variation in the optical light curve of the companion star from data from the 2.4-m at MDC. The modulation is dominated by a process of heating a companion by the pulsar wind which contributes most at phase 0.75 (see Fig. 3.8; Jules Halpern, private communication). In general, light curves of BWs are most affected by heating from the MSP wind due to their very compact orbits.

PSR J2115+5448

PSR J2115+5448 is a black widow pulsar with spin period of 2.6 ms, DM of 77.41 pc cm^{-3} orbital period of 3.2 hours, and minimum companion mass of 0.02 $M_{\odot}$. See the discovery plot at Fig. 3.9.

PSR J2115+5448 exhibits short-duration eclipses during many observations and has an orbital period derivative ($\dot{P}_B = 6 \times 10^{-11}\,\mathrm{s\,s^{-1}}$), suggesting a modulation in orbital period. It has a high spin-down luminosity ($\dot{E}$) of $1.65 \times 10^{35}\,\mathrm{erg\,s^{-1}}$, placing it in a group of few *Fermi* MSPs with the spin-down luminosity more than $10^{35}\,\mathrm{erg\,s^{-1}}$. However, a contribution in $\dot{P}_{\mathrm{obs}}$ from the Shklovskii effect has not been measured yet which results in an overestimation in $\dot{P}$ and therefore an overestimation in $\dot{E}$ ($\dot{E} \propto \dot{P}/P^3$).

3.3.3 Single-pulse search

This section is contributed by Anna Bilous

For all four pulsars the single-pulse search was run on the discovery session. This search did not yield any positive results (see Figures 3.10 and 3.11): no excess of single-pulse candidates were detected at the respective DMs of all four pulsars. Search sensitivity was calculated using Eq. 2.3. The $S_{\mathrm{thr}} \times \sqrt{n_{\mathrm{box}}}$ was 0.4 Jy for 820 MHz (for the threshold S/N of 5).

The energies of single pulses from the non-recycled pulsars usually have normal or log-normal distribution (Burke-Spolaor et al. 2012). The analogous distributions for MSPs (let alone RB/BW systems) are not very well known, however, some of the MSPs are known to emit, in addition to normal pulses, a distinct class of pulses called Giant Pulses (GPs). GPs are bright narrow pulses with a steep power-law energy distribution. According to Knight (2006), for the established GP emitters, which are a very small segment of the MSP population, the probability of detecting a GP with the energy 20 times exceeding the energy of the average profile[2] varies between 10^{-4} (B1937+21) to 10^{-7} per pulsar spin period.

[2]Or, equivalently, with $S_{\mathrm{sps}}/S > 20$.

Taking into account the $S_{\rm sps}/S$ from Table3.1 and the corresponding lengths of sessions measured in pulsar spin periods, it can be concluded that our pulsars do not emit GPs much brighter than those of PSR B1937+21. However, the sensitivity and time span of the observations do not allow us to rule the GP-like emission completely.

Two additional notes should be made. Firstly, the average flux of RB/BW systems is known to vary within an order of magnitude. Thus, other, future single-pulse searches can be more fruitful. Secondly, the width of GPs can be smaller than our time resolution of 64 μs ($n_{\rm box} = 1$), which effectively reduces the sensitivity.

3.4 Discussion

3.4.1 Flux variations

All of the new MSPs exhibit eclipses and/or flux variations. PSR J1513−2550 and PSR J2017−1614 show eclipses in some sessions but show no sign of flux variability in others (see Fig. 3.12 and 3.14). PSR J2115+5448 and PSR J1622−0315, however, both exhibit regular and irregular eclipses, and flux variability in different observations (see Figures 3.15 and 3.13). In general, flux variation of a pulsar is a result of significant scattering effects from the interstellar medium (ISM) along the line of sight. The variation in flux of BW and RB, however, can either caused by the scattering effect from the ISM or ejected particles from a companion, or both. Studying

Pulsar	$S_{\rm sps}/S \times \sqrt{n_{\rm box}}$	**Length of session, s**	**Length of session,** P
J1513-2550	5088	1966	9.4×10^5
J1622-0315	6467	2580	6.8×10^5
J2017-1614	35617	2950	1.3×10^6
J2115+5448	7877	2950	1.1×10^6

Table 3.1:: Sensitivity to single pulse flux and observing session durations.

the flux variation in BWs and RBs, thus, can probe properties of the ISM and/or particles expelling from the companion.

3.4.2 Optical, X-ray and γ-ray counterparts

Multi-wavelength studies of BWs and RBs bring much additional information about the MSPs and their companions in these fascinating binary systems. The shape and peak of the optical light curve from photometry of the binaries reveals information about the companion as well as an interaction between the companion and the pulsar. The sinusoidal shape of the light curve indicates the modulation of the near-Roche lope filling companion (as seen in PSR J1622−0315). The light curve peak at orbital phase of 0.75 (superior conjunction) suggests irradiation from the pulsar which means the pulsar is possibly ablating the companion. Furthermore, the double peaks at phase zero and 0.5 indicate tidal interaction between the pulsar and the companion. Colors from optical photometry additionally reveal physical properties of the companion namely radius and temperature.

By monitoring the BWs or RBs at high energies (X-ray and γ-ray), one may detect the orbital modulation in X-ray or γ-ray which could be the result of intra-binary shocks where the pulsar-wind pressure balances the wind pressure from the companion star (e.g. Archibald et al. (2010) and Xing & Wang (2015)). Additionally, drastic increases in the γ-ray flux and the disappearance of radio pulsations in RBs could signal the transition from rotation-powered to accretion-powered pulsar states (Stappers et al. 2014). Observing RBs with optically bright companions can help constrain the mass function of the companion and the pulsar (Bellm et al. 2016). Furthermore by regularly monitoring RBs in multiple wavebands, we may be able to find a new transitioning pulsar. This is because the transition between the accretion-

power stage (LMXBs: X-ray loud, radio quiet) to the rotation-power stage (binary pulsar: X-ray quiet, radio loud) can take place within the relatively short time scale of years or even months (e.g. Archibald et al. 2015; Benvenuto et al. 2015)

3.5 Conclusion

In this chapter, we investigate the properties and counterparts of four new MSPs in compact orbits with low mass companions, known as black widows (BWs) and redbacks (RBs), discovered with the GBT in *Fermi* unassociated sources. PSR J1513−2550, J2017−1614 and J2115+5448 are BWs and PSR J1622−0315 is a RB. All four MSPs are eclipsing which is one of the signature behaviours of these systems. PSR J1622−0315 and PSR J2155+5448 exhibit "irregular" short-time eclipses at a random orbital phase. The short-duration eclipses are the result of material ejected from the companion which result in flux density variability. From the follow-up observations at the GBT and the Nançay telescope, we obtained phase-connected timing solutions for all of the pulsars. From pulsar timing, we were able to measure the orbital period derivative of PSR J1622−0315 and J2115+5448 and the proper motion of PSR J1622−0315. With the precise timing ephemerides, we folded *Fermi* LAT photons and found that PSR J1622−0315 and J2017−1614 have likely significant γ-ray pulsations. The optical light curve from PSR J1622−0315 is sinusoidal at half the orbital period, indicating that the companion is filling its Roche lobe. We also performed single-pulse searches on all pulsars and found no significant individual pulses.

The BWs and RBs are thought to be the missing links in pulsar evolution. Therefore monitoring these systems in multiple wavelength bands will illuminate other properties of these fascinating systems. Such observations will allow us to glimpse the eclipse mechanism(s), the transition from LMXBs to rotation-powered pulsars,

and the formation of isolated MSPs.

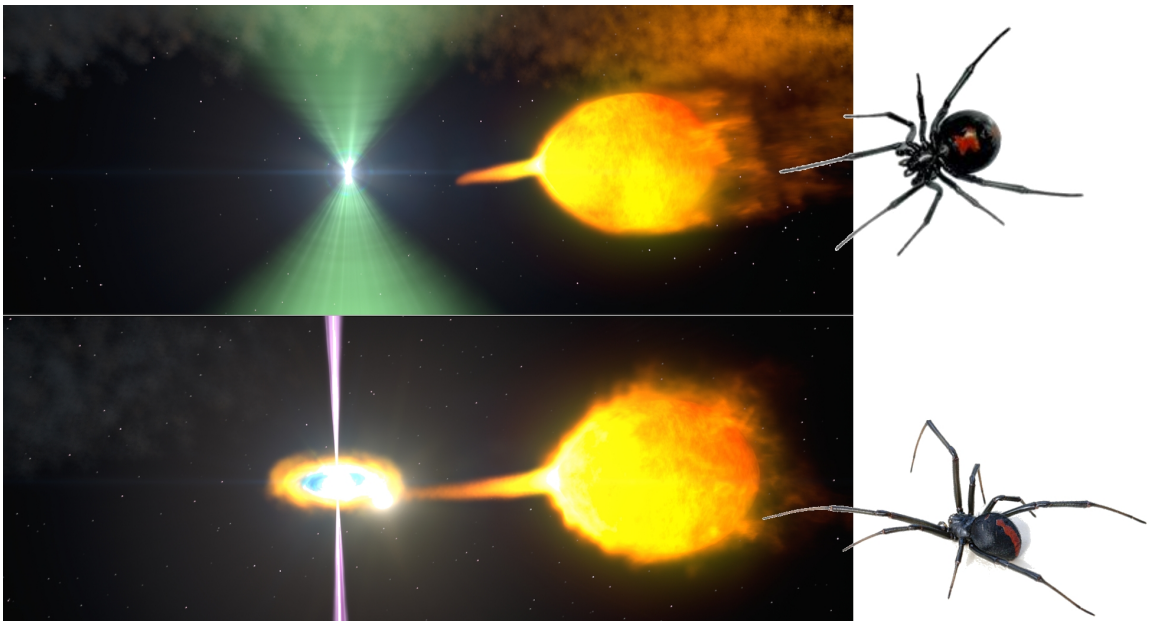

Fig. 3.1.—: Artist's impression of a redback (top) and a black widow binary systems together with the photgraphs of their arachnid namesakes. *(Image credits: NASA Goddard's Scientific Visualization Studio, Wikipedia)*

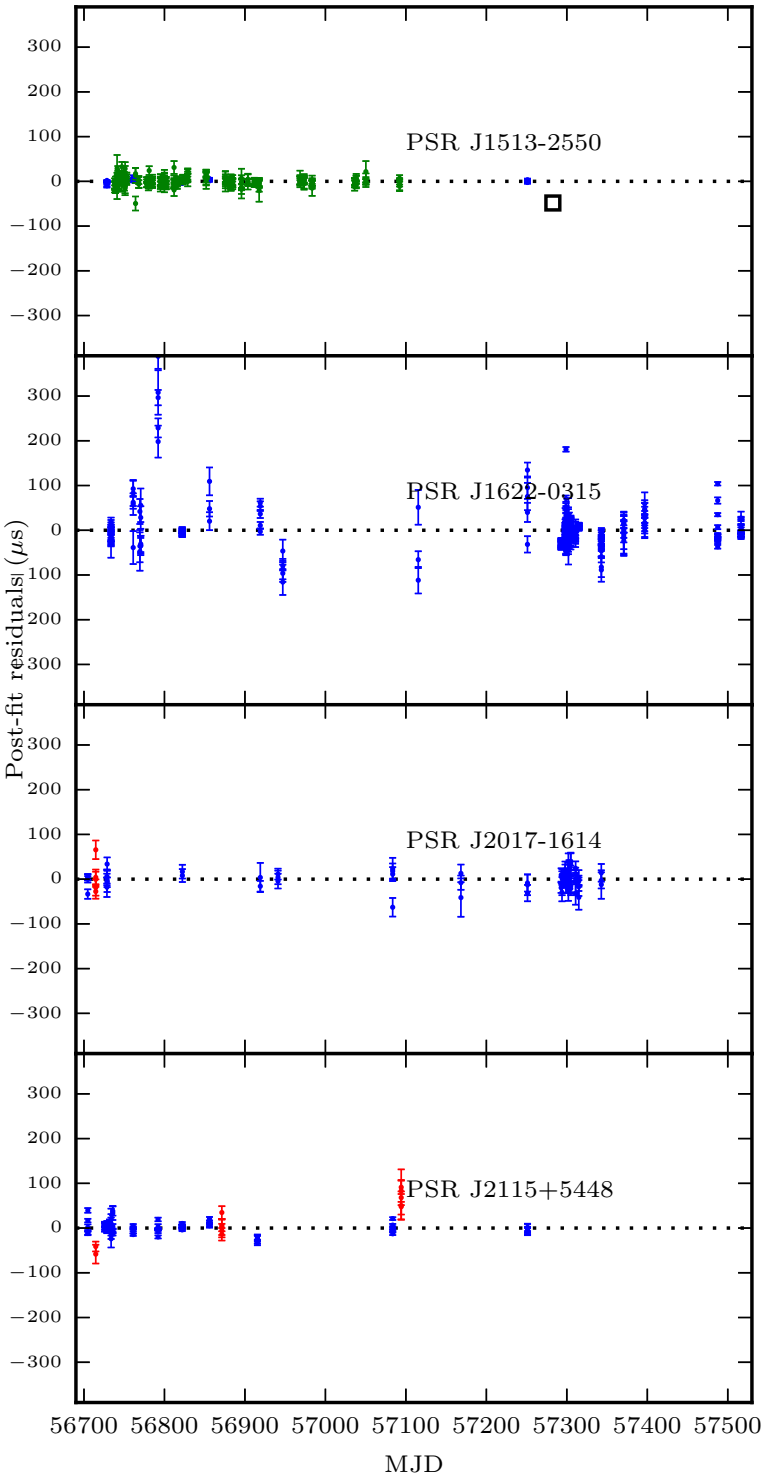

Fig. 3.2.—: The residual plots of PSR J1513−2550, PSR 1622−0315, PSR J2017−1614 and PSR J2115+5448 as a function of observing time in MJD and the residual time in μs. The red, blue and green dots are the observation at 350 MHz, 820 MHz and 1400 MHz respectively.

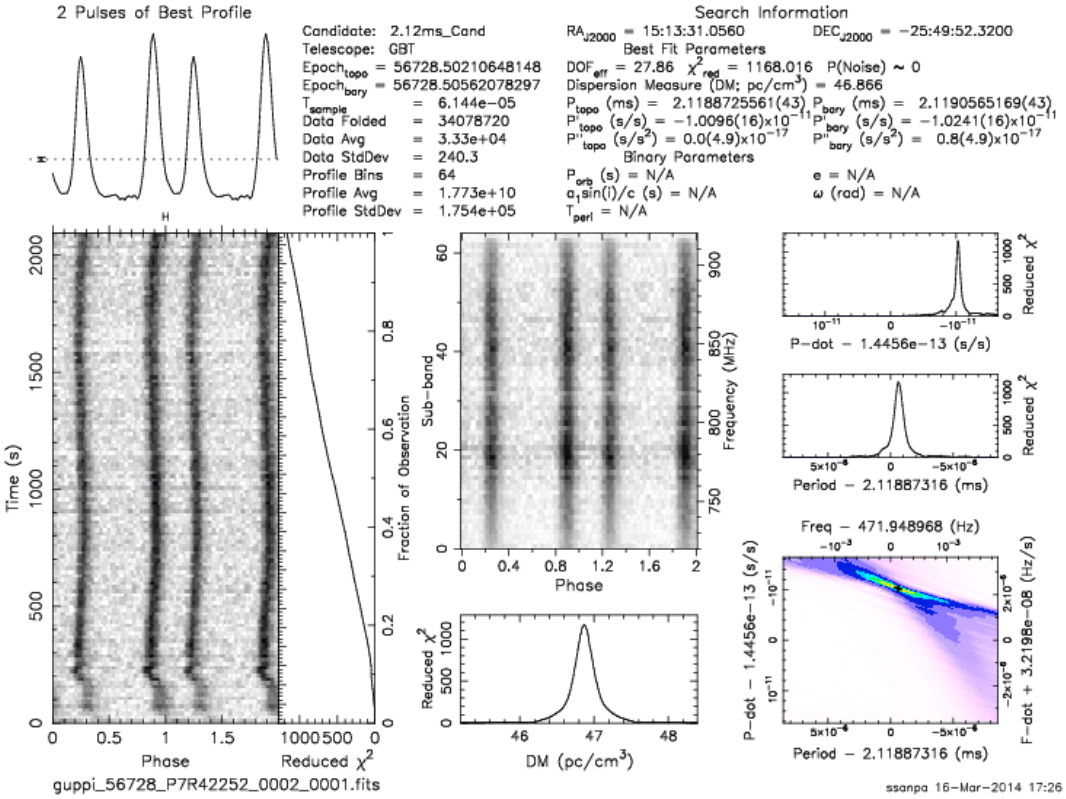

(a)

Fig. 3.3.—: The discovery plots of PSR J1513−2550. The pulsar signal is very bright, resulting in the prominent peak in DM-P-$\dot{P}$ parameter space. In this 30-min observation, the period shows almost no acceleration-induced variation, however, there is some evidence of the eclipse egress or confusion due to gases from a companion at the start of the observing session.

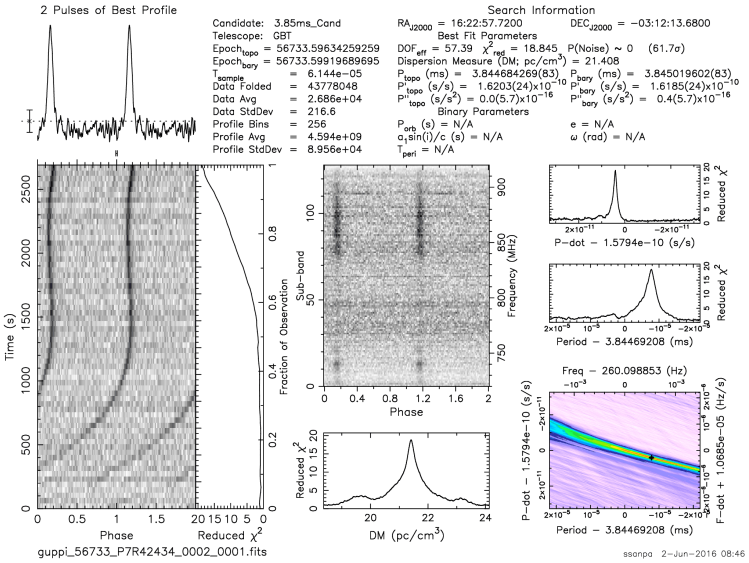

(a)

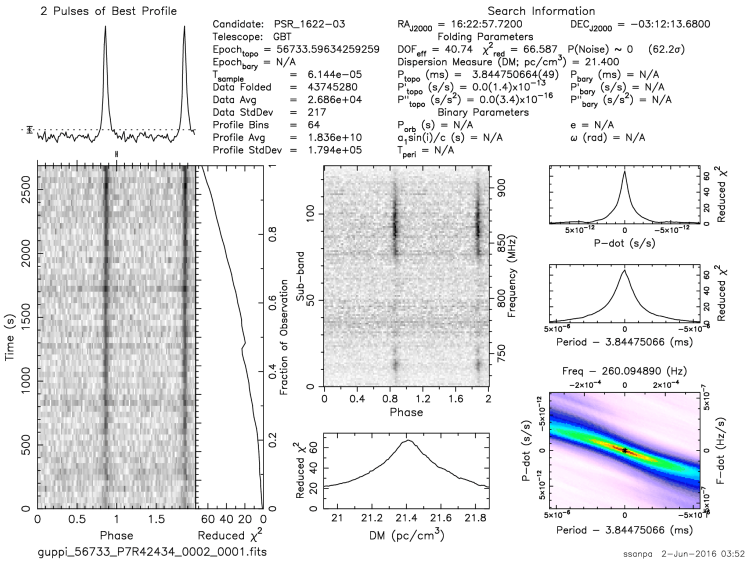

(b)

Fig. 3.4.—: The discovery plot of PSR J1622−0315 is shown on panel 3.4a. The curvature of the pulsar-like signal on the waterfall plot indicates large acceleration of the star. This curvature can be corrected by folding the raw data with an improved pulsar ephemeris (panel 3.4b). The cloud at the beginning of the session could be a result from eclipse or scintillation.

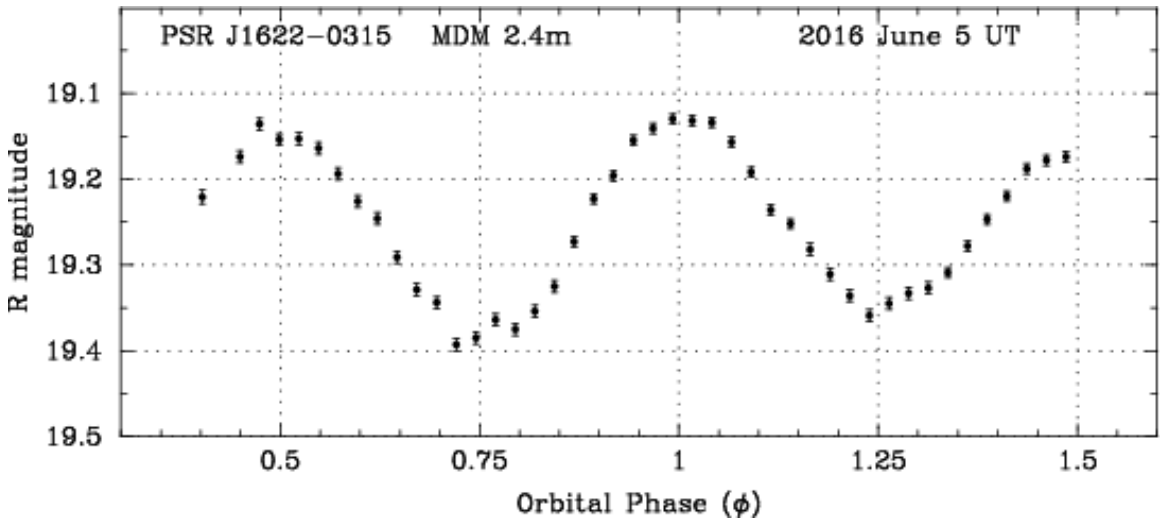

Fig. 3.5.—: Optical light curve of PSR J1622+0315 taken with the 2.4-m Telescope of the MDM Observatory on 2016 June 5 shows an sinusoidal modulation in magnitude which is consonant with ellipsoidal distortion from a companion filling its Roche lobe. *Image credit: Jules Halpern*

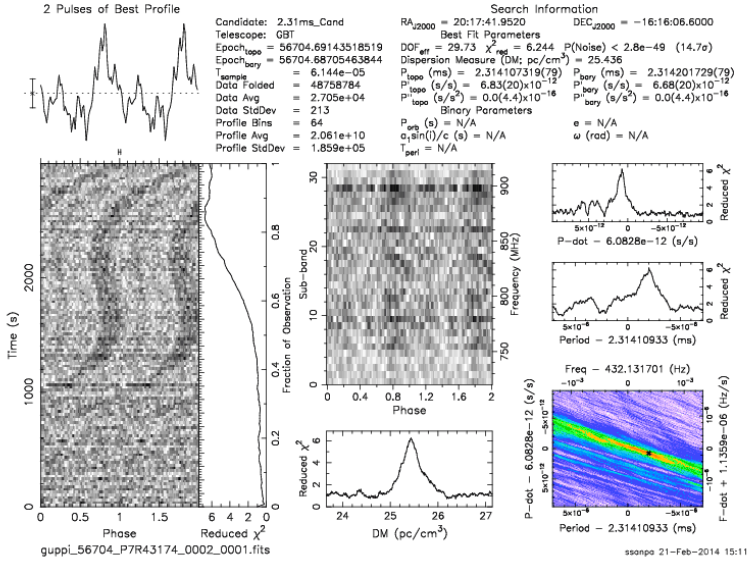

(a)

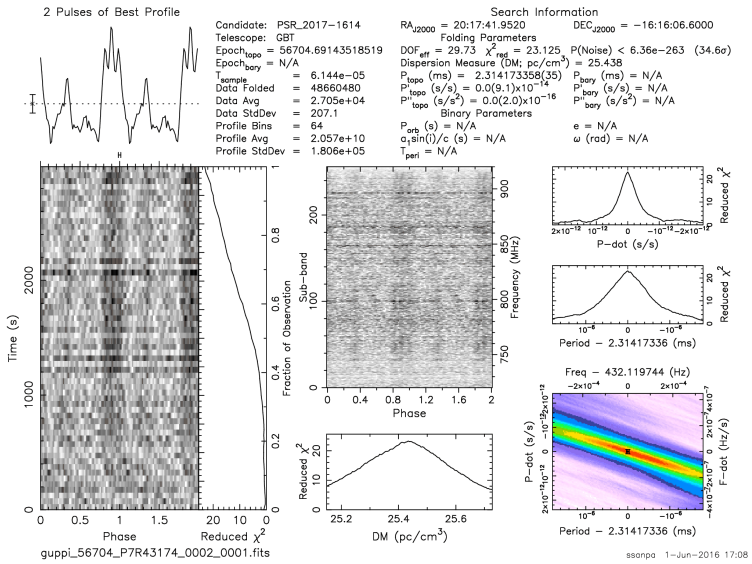

(b)

Fig. 3.6.—: The discovery plot of PSR J2017−1614. The acceleration from the pulsar orbital motion shows as a curvature in the waterfall plot on the panel 3.6a which is corrected by folding data with an improved ephemeris from the timing solution as shown in panel 3.6b. The beginning of the observation shows evidence of an eclipse.

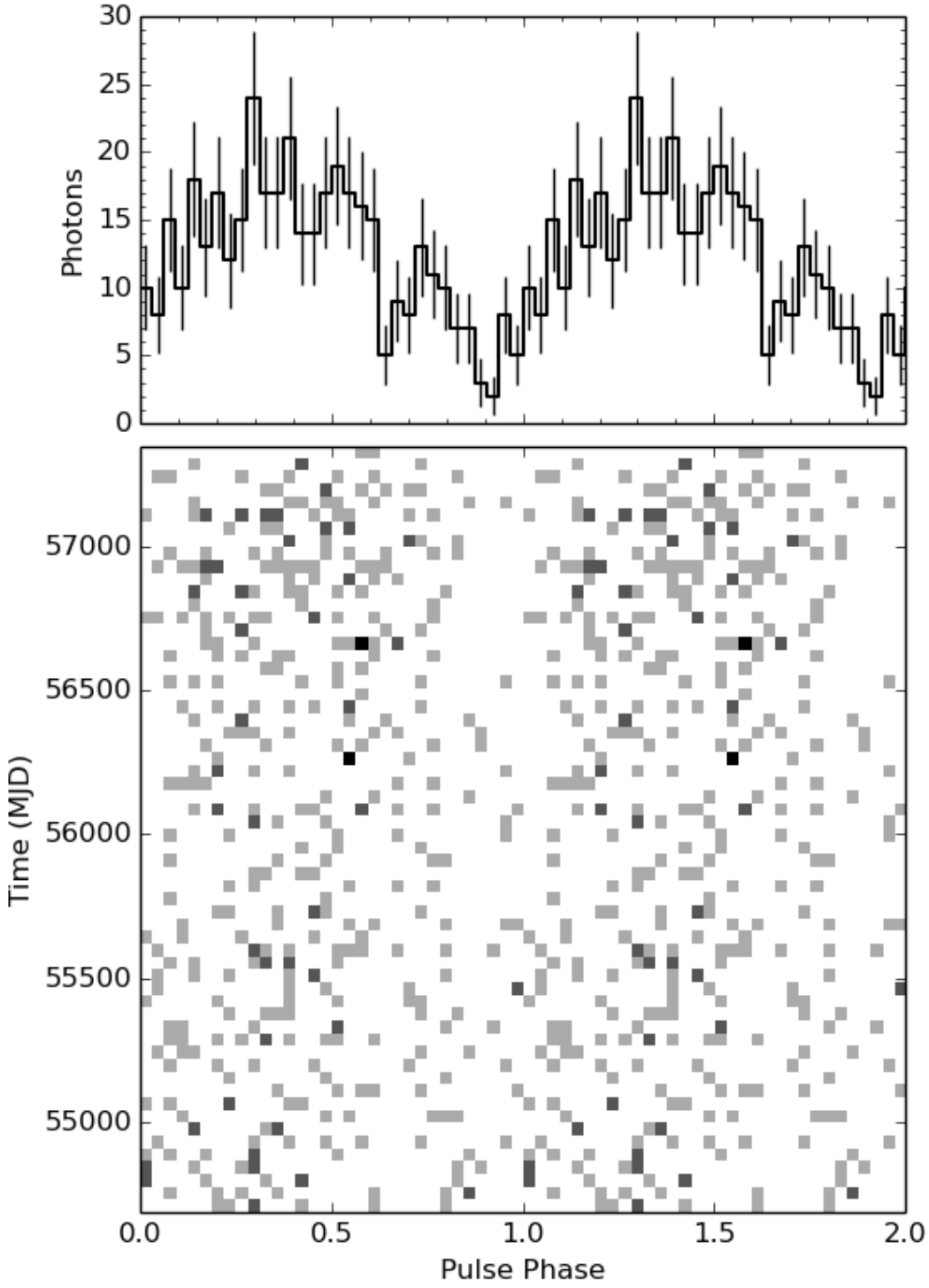

Fig. 3.7.—: The phaseogram that shows a weak γ-ray pulsation of PSR J2017−1614. The detection threshold is $5.7\,\sigma$ with a radius < 0.5 degree and energy > 900 Mev cut-off. *Image credit: Paul Ray*

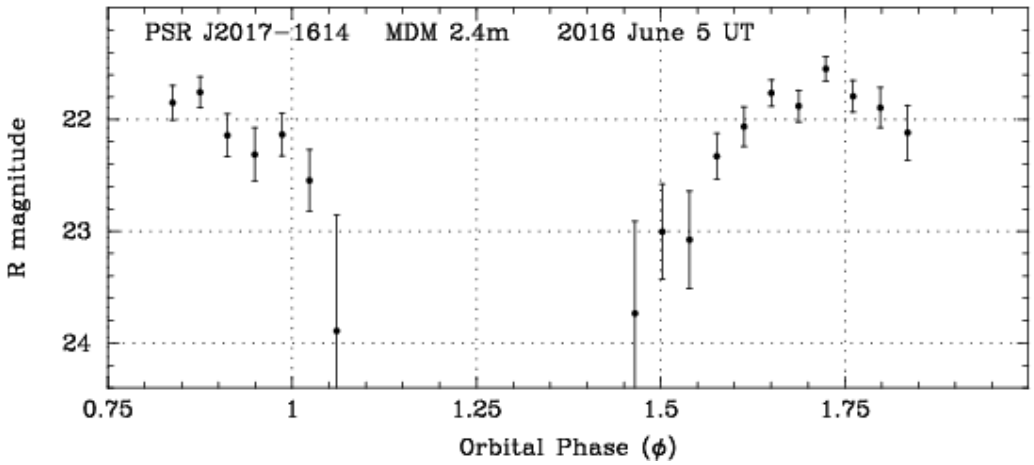

Fig. 3.8.—: Optical light curve of PSR J2017−1614 taken with the 2.4-m Telescope of the MDM Observatory on 2016 June 5. Even though the light curve only displays a partial orbit, it shows maximum brightness at phase 0.75, when heating from the pulsar should be maximized. *Image credits: Jules Halpern*

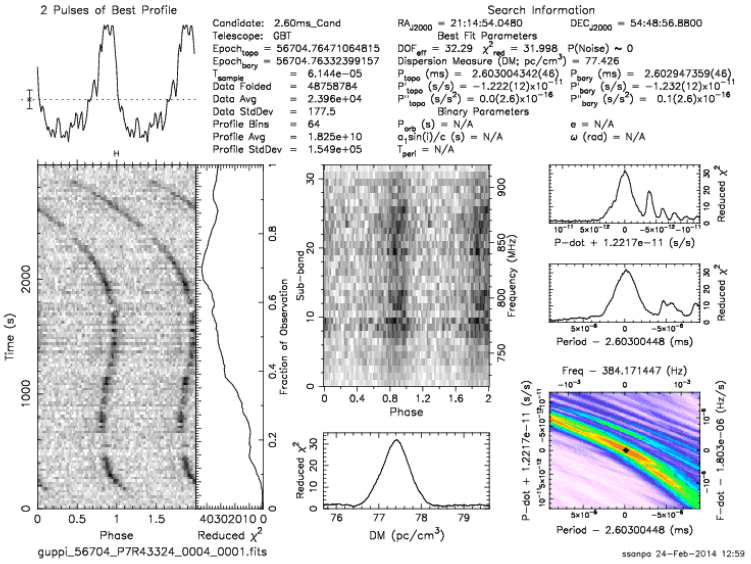

(a)

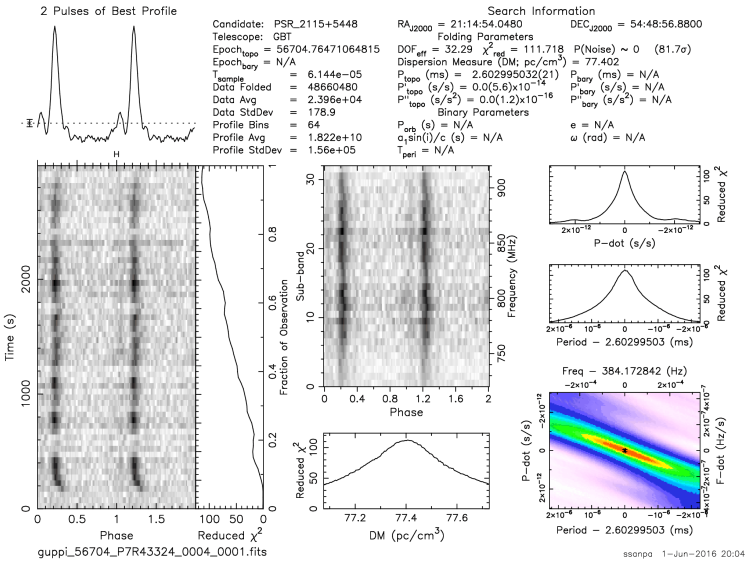

(b)

Fig. 3.9.—: The discovery plot of PSR J2115+5448. PSR J2115+5448 was accelerated by the orbital motion, which resulted in curvature of the pulsar-like signal as shown in Fig.3.9a. The curvature is corrected with the parameters from pulsar timing in Fig3.9b. The pulsar exhibits scintillations, and possibly also short iregular eclipses throughout the observation.

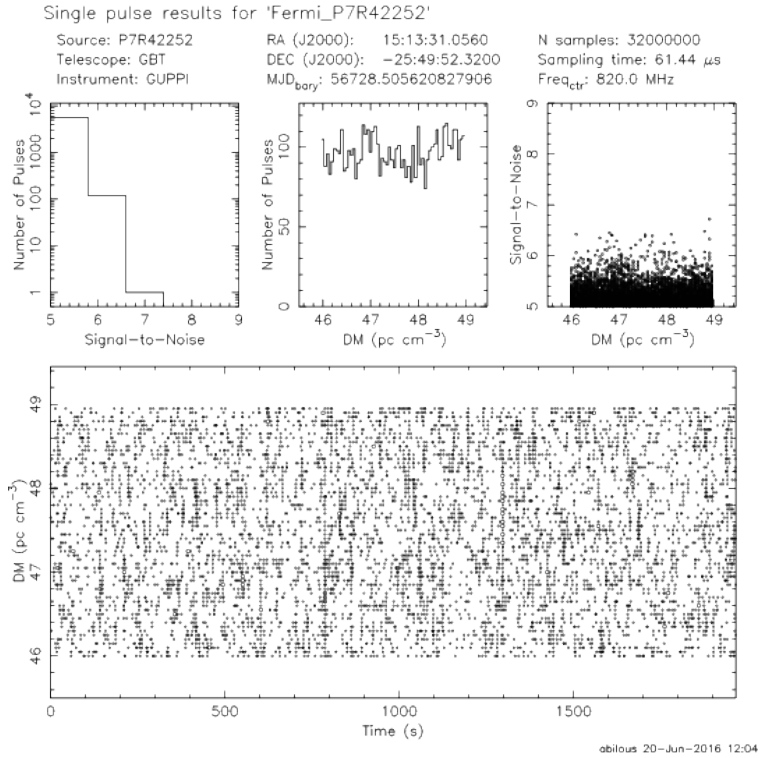

(a)

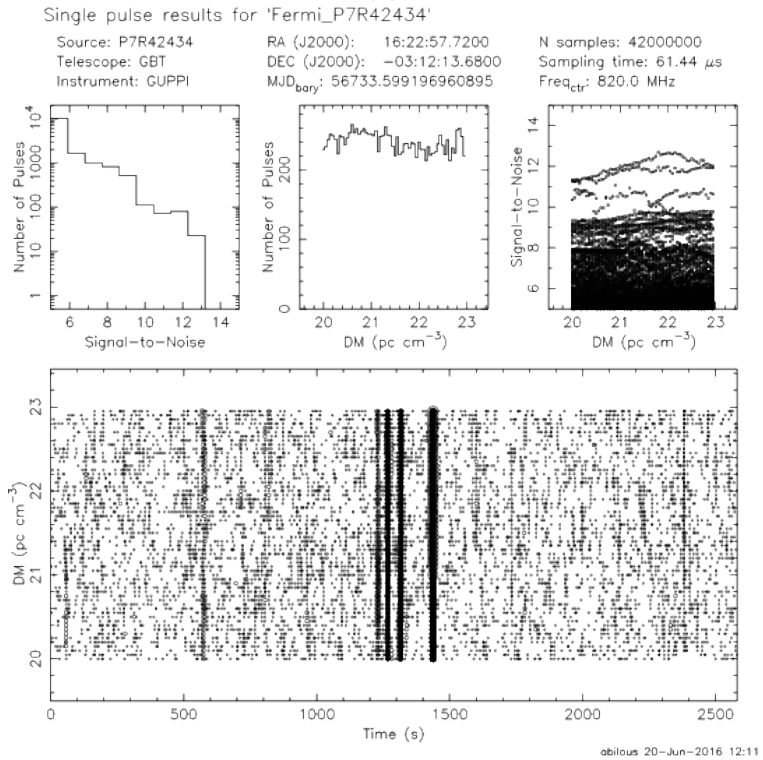

(b)

Fig. 3.10.—: Single-pulse diagnostic plots for PSR J1513−2250 (a) and PSR J1622−0315 (b). No obvious single-pulse candidates were detected at the pulsars' respective DMs of 46.86 pc cm^{-3} and 21.4 pc cm^{-3}.

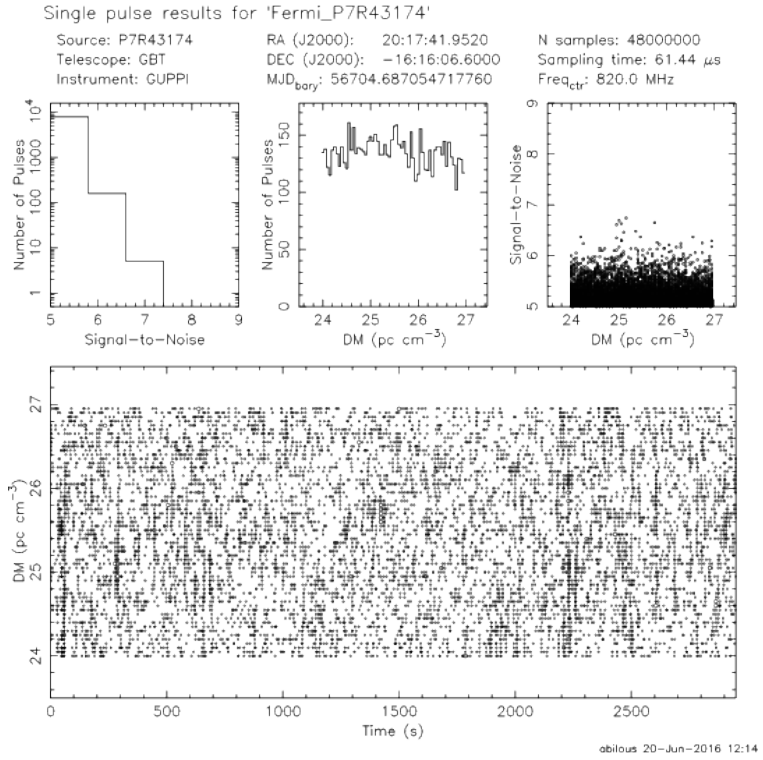

(a)

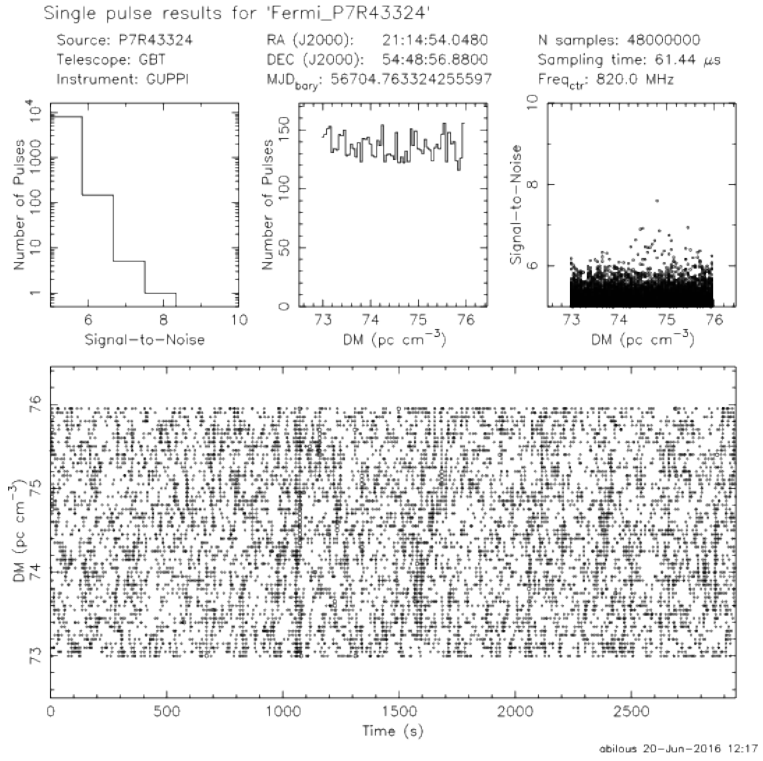

(b)

Fig. 3.11.—: Single-pulse diagnostic plots for PSR J2017−1614 (a) and PSR J2115+5448 (b). No obvious single-pulse candidates were detected at the pulsars' respective DMs of 25.44 pc cm^{-3} and 77.4 pc cm^{-3}.

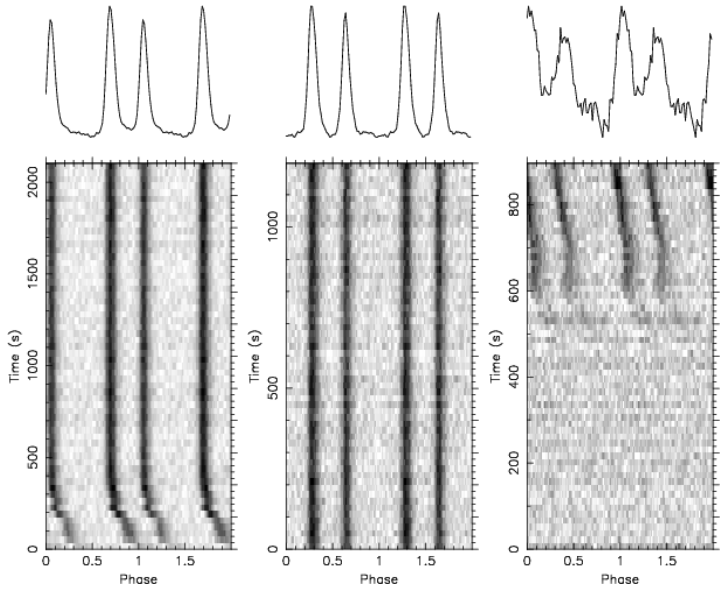

(a) (b) (c)

Fig. 3.12.—: Example of folded pulse profiles PSR J1513−2550 at 820 MHz. Panel 3.12a and 3.12c show evidence of an eclipse egress at the beginning and two-thirds of the way through the observation, respectively. The pulsar signal is very strong and exhibits no flux density variations at other times.

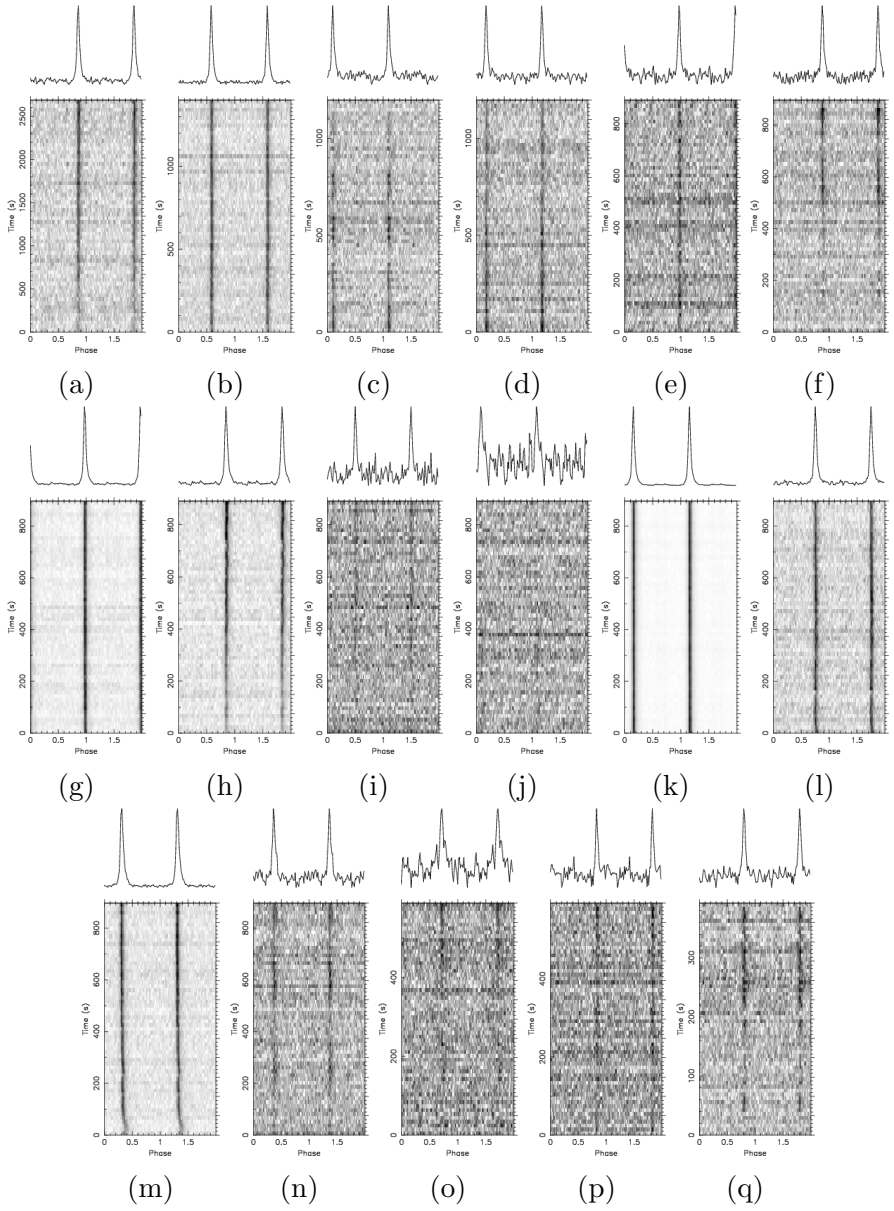

Fig. 3.13.—: Example of folded pulse profiles of PSR J1622−0315 at 820 MHz. Diffractive scintillation is demonstrated by the variability of flux density among same length observations. For instance, the observed intensities of the 15-minute observations from panel 3.13e through 3.13n vary by a factor of ~ 120 ($\sim 0.1 - 12$ mJy). Additionally, the irregular eclipses (the flux variability within the observation) are exhibited on panel 3.13a, 3.13c, 3.13d, 3.13f, 3.13h, 3.13i, 3.13j and from 3.13m to 3.13q.

.

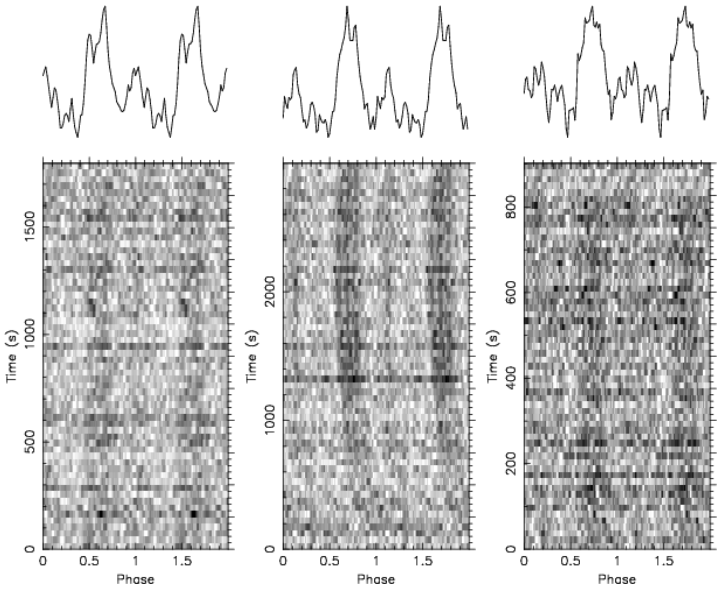

(a) 350 MHz (b) 820 MHz (c) 820 MHz

Fig. 3.14.—: Example folded pulse profiles of PSR J2017−1614 at 350 MHz on panel 3.14a and at 820 MHz on panel 3.14b and 3.14c. There is no obvious variation in flux density in different observation with the same length. The panel 3.14b shows the egress from the eclipse about one-third of the way through the observation.

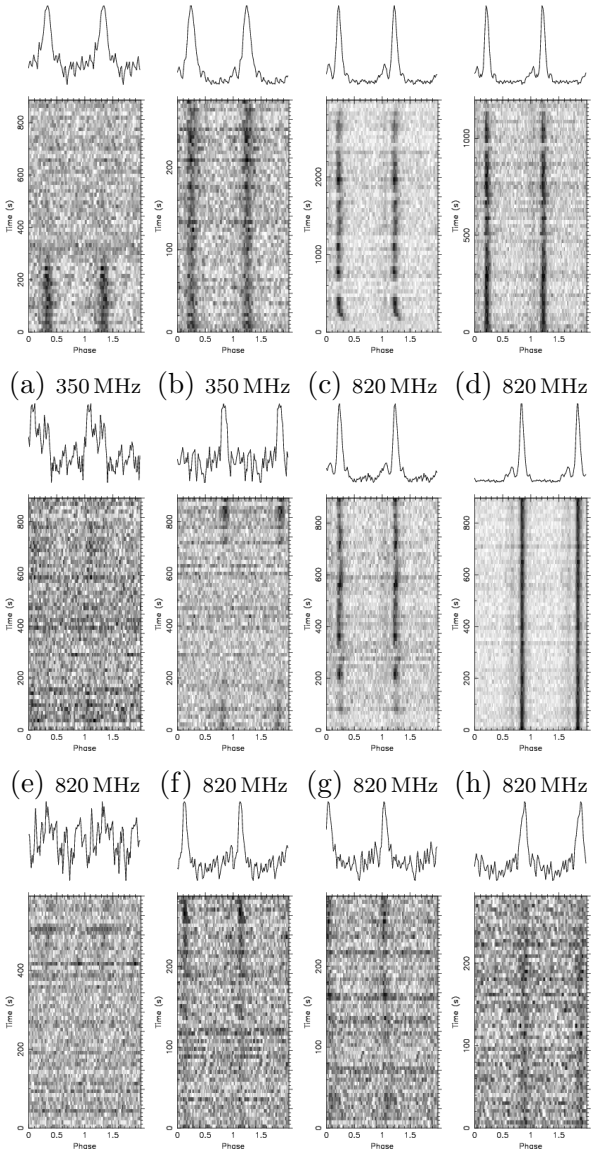

(a) 350 MHz (b) 350 MHz (c) 820 MHz (d) 820 MHz

(e) 820 MHz (f) 820 MHz (g) 820 MHz (h) 820 MHz

(i) 820 MHz (j) 820 MHz (k) 820 MHz (l) 820 MHz

Fig. 3.15.—: Example folded pulse profiles of PSR J2115+5548 at 350 MHz on panel 3.15a and 3.15b, and at 820 MHz from panel 3.15c through 3.15l. The panel 3.15a displays eclipsing ingress at 350 MHz about one third into the observation. There is evidence of eclipsing egress at the beginning of the 820 MHz observation on panel 3.15c. The variations of intensity indicate the scintillation of the pulsar emission.

Chapter 4

Conclusions and Future Work

In this thesis, I present the discovery and analysis of 12 new MSPs with He-WD companions and four new "Spider" MSPs in compact orbits (orbital periods < 1 day). These MSPs were discovered by searching for pulsar-like signals within the error boxes of *Fermi*LAT unassociated sources with the GBT. For all of the MSPs timing solutions were established, and γ-ray pulsations were detected for twelve of them.

For the timing analyses of the 12 He-WD MSP systems, we were able to determine better measurements of $\dot{P}$ for several of the pulsars using a new MCMC single-photon timing technique over the full *Fermi* mission. One of the brightest pulsars, with the lowest timing rms residuals, has already been added to the NANOGrav timing array. We performed single-pulse searches on all 198 *Fermi* LAT sources and also searched 20 sources near the Galactic plane for young pulsars. However, the results were negative in both cases. We confirmed that there is almost no correlation between γ-ray and radio flux density, which suggests the possibility of finding new bright radio pulsars by searching faint γ-ray sources. Additionally, we have examined the $P_b - M_c$ relation, including the twelve new pulsars with He-WD companions, and

found that the distribution of binary inclination angles i may be skewed towards lower inclinations (as opposed to $\cos i$ being drawn from a uniform distribution, as would be the case if orbits are randomly distributed).

The four new "spider" pulsars (those thought to be missing links in pulsar evolution), exhibit regular eclipses and/or random short-duration eclipses. Such behaviour is the signature of Black Widow and Redback systems. Two of the four pulsars show extremely strong diffractive scintillation at our 820 MHz observing frequency. For two of the MSPs we found optical counterparts. One of them shows modulation in its light curve with a period equal to half of P_b, which indicates ellipsoidal distortion of the swollen companion.

We plan to perform optical observations of the four spiders in September 2016 to (1) obtain more data on those that are marginally detected, and (2) to acquire multi-color light curves for further more detailed studies. These studies will be led by Jules Halpern. Additionally, we were granted 80 hours of GBT time in the Fall 2016 semester to search for even more pulsars towards *Fermi* unassociated sources. We expect to find new MSPs and possibly other exotic pulsar systems as part of this project.

With a number of new, state-of-the-art radio telescopes achieving first light in the near future (e.g. FAST and SKA), we will extend pulsar timing baselines and reduce the rms timing residuals of known pulsars, as well as search for new sources. Now that the Gravitational Wave (GW) window on the universe has opened (e.g. Abbott et al. 2016b,a)[1], discovering more MSPs is crucial to improve the sensitivity of the Pulsar Timing Arrays that will be used to directly detect other longer-wavelength GWs. It is not an exaggeration to say that the *Fermi* LAT sources are gifts that keep

[1]Note that the LIGO project is sensitive to GW frequencies on the order of hundreds of Hz (such as those produced by NS-NS or BH-BH mergers), while PTAs are sensitive to GW frequencies in the nanohertz regime (such as those produced by SMBH binaries).

on giving, and that the best of the pulsar era is yet to come.

Chapter 5

Appendix: Tables

Table 5.1. Best-fit Parameters for the MSPs J0605+3757, J1312+0051, and J1855-1436 with DD binary model

Parameter	PSR J0605+3757	PSR J1312+0051	PSR J1855-1436
Right Ascension (RA, J2000)	$06^{\rm h}\ 05^{\rm m}\ 5\overset{\rm s}{.}5439(1)$	$13^{\rm h}\ 12^{\rm m}\ 46\overset{\rm s}{.}64232(9)$	$18^{\rm h}\ 55^{\rm m}\ 54\overset{\rm s}{.}2286(3)$
Declination (DEC, J2000)	$37^\circ\ 57'\ 35\overset{''}{.}96(1)$	$+00^\circ\ 51'\ 0\overset{''}{.}104(3)$	$-14^\circ\ 36'\ 8\overset{''}{.}98(3)$
Galactic Longitude, l (°)	174.19	314.84	20.36
Galactic Latitude, b (°)	8.02	63.23	-7.57
Spin Period (ms)	2.7279541573929(5)	4.2280189916604(2)	3.594091653371(1)
Period Derivative, $\dot{P}_{obs}$ (10^{-21})	4.8(2)	17.527(3)	10.9(1)
Reference Epoch (MJD)	56130.0	55600.0	57066.0
Dispersion Measure ($pc\,cm^{-3}$)	20.9462(4)	15.345(1)	109.2
Flux Density at 820 MHz (mJy)	0.37(9)	0.8(5)	0.24(6)
Binary Model	DD	DD	DD
Projected Semi-Major Axis (lt-s)	18.948654(3)	14.7498916(6)	29.219353(5)
Orbital Period, P_b (days)	55.6723344(6)	38.50383280(2)	61.5399707(7)
Orbital Eccentricity	0.0003743(4)	0.00023821(7)	0.0002974(5)
Epoch of Periastron (MJD)	55968.810(7)	55123.856(2)	56788.76(2)
Longitude of Periastron, ω (deg)	133.74(4)	219.11(2)	234.98(9)
Span of Timing Data (MJD)	55917 – 56349	55128 – 57115	56735 – 57396
Number of radio TOAs	106	262	140
RMS radio TOA Residual (μs)	13.53	4.806	36.2
Derived Parameters			
Proper Motion in RA ($\rm mas\,yr^{-1}$)	...	-22.35(66)	...
Proper Motion in DEC ($\rm mas\,yr^{-1}$)	...	-11.2(1.5)	...
Transverse velocity, V_T ($\rm km\,s^{-1}$)	...	$9(2)\times10^1$	...
Shklovskii effect, $\dot{P}_{shk}$ (10^{-21})	...	5(1)	...
Galactic potential effect, $\dot{P}_{gal}$ (10^{-21}) ...	0.19(4)	0.33(7)	1.6(5)
Intrinsic Period Derivative, $\dot{P}_{int}$ (10^{-21}) *	4.6(2)	12(1)	9.3(5)
Mass Function ($M_\odot$)	0.002356888(1)	0.0023240276(3)	0.007072614(3)
Minimum Companion Mass ($M_\odot$)	$\geq$0.18	$\geq$0.18	$\geq$0.27
DM-derived Distance (kpc)	0.7	0.8	3.1

Table 5.1—Continued

Parameter	PSR J0605+3757	PSR J1312+0051	PSR J1855-1436
Surface Magnetic Field (10^8 G)	1.1	2.3	1.8
Characteristic Age (Gyr)	9.4	5.6	6.1
Spin-down Luminosity, $\dot{E}$ (10^{34} ergs s^{-1})	0.89	0.63	0.79
γ-ray Spectral Fit Parameters			
Fermi 5-Year Source (3FGL)	3FGL J0605.0+3756	3FGL J1311.0+0036	3FGL J1856.1-1217
TS	177	913	...
TS_{cut}	48	72	...
$TS_{b\ free}$	0	1	...
N_0 (10^{-12} cm^{-2} s^{-1} MeV^{-1})	$2.9\pm1.3\pm0.3$	$5.9\pm0.6\pm0.3$	...
Spectral Index Γ	$0.2\pm0.6^{+0.4}_{-0.2}$	$1.6\pm0.1\pm0.1$	...
E_C (GeV)	$1.2\pm0.3^{+0.2}_{-0.1}$	$2.5\pm0.5\pm0.1$	...
F_{100} (10^{-9} cm^{-2} s^{-1})	$3.5\pm1.1^{+0.9}_{-0.3}$	$1.9\pm0.2\pm0.1$	...
G_{100} (10^{-12} erg cm^{-2} s^{-1})	$6.0\pm0.8^{+0.2}_{-0.1}$	$1.5\pm0.1\pm0.1$	...
Pulsed Significance (σ)	7.7σ	13.8σ	...
γ-ray Efficiency, η (%)	3.95	1.82	...

*$\dot{P}_{int} = \dot{P}_{obs} - \dot{P}_{shk} - \dot{P}_{gal}$ when $\dot{P}_{shk}$ is available

Note. — Numbers in parentheses represent 1-σ uncertainties in the last digit for the timing parameters. Minimum companion masses were calculated assuming a pulsar mass of 1.4 $M_\odot$. The DM-distances were derived according to the NE2001 Galactic electron density model (Cordes & Lazio 2002) and likely have ∼20% uncertainties. The contribution in period derivative from the Shklovskii effect are included for the pulsar with significant measurement of proper motion.

Table 5.2. Best-fit Parameters for the Isolated MSP J0533+6759

Parameter	PSR J0533+6759
Right Ascension (RA, J2000)	$05^{\rm h}\ 33^{\rm m}\ 55\overset{\rm s}{.}1401(3)$
Declination (DEC, J2000)	$67^\circ\ 59'\ 17\overset{''}{.}489(3)$
Galactic Longitude, l (°)	144.78
Galactic Latitude, b (°)	18.18
Spin Period (ms)	4.3881599698083(9)
Period Derivative, $\dot{P}_{obs}$ (10^{-21})	12.61(9)
Reference Epoch (MJD)	55877.0
Dispersion Measure ($pc\,cm^{-3}$)	57.369(2)
Flux Density at 820 MHz (mJy)	0.26(3)
Span of Timing Data (MJD)	55547 – 56207
Number of radio TOAs	86
RMS radio TOA Residual (μs)	24.05
Derived Parameters	
Proper Motion in RA ($\rm mas\,yr^{-1}$)	...
Proper Motion in DEC ($\rm mas\,yr^{-1}$)	...
Transverse velocity, V_T ($\rm km\,s^{-1}$)	...
Shklovskii effect, $\dot{P}_{shk}$ (10^{-21})	...
Galactic potential effect, $\dot{P}_{gal}$ (10^{-21}) ...	1.3(4)
Intrinsic Period Derivative, $\dot{P}_{int}$ (10^{-21}) *	11.3(4)
DM-derived Distance (kpc)	2.4
Surface Magnetic Field (10^8 G)	2.3
Characteristic Age (Gyr)	6.2
Spin-down Luminosity, $\dot{E}$ ($10^{34}\,\rm ergs\,s^{-1}$)	0.53
γ-ray Spectral Fit Parameters	
Fermi 5-Year Source (3FGL).....	3FGL J0534.0+6759
TS	479
$\rm TS_{cut}$	31
$\rm TS_{b\ free}$	1
N_0 (10^{-12} $\rm cm^{-2}\ s^{-1}\ MeV^{-1}$)	$1.1\pm0.1^{+0.6}_{-0.5}$
Spectral Index Γ	$1.6\pm0.1\pm0.1$
$E_{\rm C}$ (GeV)	$5.6\pm1.5\pm0.4$
F_{100} (10^{-9} $\rm cm^{-2}\ s^{-1}$)	$9.9\pm1.7^{+0.9}_{-0.6}$
G_{100} (10^{-12} erg $\rm cm^{-2}\ s^{-1}$)	$9.9\pm0.8^{+0.6}_{-0.5}$
Pulsed Significance (σ)	13.5σ
γ-ray Efficiency, η (%)	128.73

*$\dot{P}_{int} = \dot{P}_{obs} - \dot{P}_{shk} - \dot{P}_{gal}$ when $\dot{P}_{shk}$ is available

Note. — Numbers in parentheses represent 1-σ uncertainties in the last digit for the timing parameters. Minimum companion masses were calculated assuming a pulsar mass of 1.4 $M_\odot$. The DM-distances were derived according to the NE2001 Galactic electron density model (Cordes & Lazio 2002) and likely have ∼20% uncertainties. The contribution in period derivative from the Shklovskii effect are included for the pulsar with significant measurement of proper motion.

Table 5.3. Best-fit Parameters for the MSPs J0621+2514 and J1137+7528 with ELL1 binary model

Parameter	PSR J0621+2514	PSR J1137+7528
Right Ascension (RA, J2000)	$06^{\rm h}\ 21^{\rm m}\ 10\overset{\rm s}{.}8542(1)$	$11^{\rm h}\ 37^{\rm m}\ 2\overset{\rm s}{.}0573(4)$
Declination (DEC, J2000)	$25^\circ\ 14'\ 3\overset{''}{.}83(3)$	$75^\circ\ 28'\ 2\overset{''}{.}3111(5)$
Galactic Longitude, $l\,(^\circ)$	187.12	129.0
Galactic Latitude, $b\,(^\circ)$	5.07	40.77
Spin Period (ms)	2.7217879391872(4)	2.5126423832770(7)
Period Derivative, $\dot{P}_{obs}$ (10^{-21})	24.83(3)	3.24(5)
Reference Epoch (MJD)	56300.0	56258.0
Dispersion Measure ($pc\,cm^{-3}$)	83.629(6)	29.1702(1)
Flux Density at 820 MHz (mJy)	0.24(5)	0.25(2)
Binary Model	ELL1	ELL1
Projected Semi-Major Axis (lt-s)	1.276860(3)	4.103576(1)
Orbital Period, P_b (days)	1.256356677(3)	7.12991220(3)
Epoch of Ascending Node (MJD)	56185.7806471(4)	55980.452289(2)
$\epsilon_1, e\cos(\omega)(10^{-6})$	$\sim$23.5	13.0(5)
$\epsilon_2, e\cos(\omega)(10^{-6})$	$\sim$20.9	42.4(5)
Span of Timing Data (MJD)	55931 – 56671	55980 – 56537
Number of radio TOAs	130	183
RMS radio TOA Residual (μs)	17.21	6.7
Derived Parameters		
Galactic potential effect, $\dot{P}_{gal}$ (10^{-21}) ...	0.8(2)	0.4(1)
Intrinsic Period Derivative, $\dot{P}_{int}$ (10^{-21}) *	24.1(2)	2.8(1)
Mass Function ($M_\odot$)	0.001416077(9)	0.001459492(1)
Minimum Companion Mass ($M_\odot$)	$\geq$0.15	$\geq$0.15
DM-derived Distance (kpc)	2.3	1.5
Surface Magnetic Field (10^8 G)	2.6	0.9
Characteristic Age (Gyr)	1.8	14.1
Spin-down Luminosity, $\dot{E}$ $(10^{34}\,{\rm erg\,s^{-1}})$	4.71	0.7

Table 5.3—Continued

Parameter	PSR J0621+2514	PSR J1137+7528
γ-ray Spectral Fit Parameters		
Fermi 5-Year Source (3FGL)	3FGL J0621.0+2514	3FGL J1136.1+7523
TS	125	18
TS_{cut}	24	4
$TS_{b\ free}$	0	1
N_0 (10^{-12} cm^{-2} s^{-1} MeV^{-1})	$1.7\pm0.3\pm0.1$	$6.2\pm2.0^{+0.3}_{-0.5}$
Spectral Index Γ	$1.3\pm0.3\pm0.1$	$2.0\pm0.2\pm0.1$
E_C (GeV)	$3.1\pm1.1\pm0.1$	···
F_{100} (10^{-9} cm^{-2} s^{-1})	$6.2\pm2.4^{+0.3}_{-0.6}$	$1.5\pm0.9\pm0.2$
G_{100} (10^{-12} erg cm^{-2} s^{-1})	$7.2\pm1.2^{+0.4}_{-0.5}$	$1.5\pm0.5\pm0.1$
Pulsed Significance (σ)	6.8σ	5.9σ
γ-ray Efficiency, η (%)	9.68	5.77

$^*\dot{P}_{int} = \dot{P}_{obs} - \dot{P}_{shk} - \dot{P}_{gal}$ when $\dot{P}_{shk}$ is available

Note. — Numbers in parentheses represent 1-σ uncertainties in the last digit for the timing parameters. Minimum companion masses were calculated assuming a pulsar mass of 1.4 $M_\odot$. The DM-distances were derived according to the NE2001 Galactic electron density model (Cordes & Lazio 2002) and likely have ∼20% uncertainties. The contribution in period derivative from the Shklovskii effect are included for the pulsar with significant measurement of proper motion.

Table 5.4. Best-fit Parameters for the MSPs J1142+0119, J1630+3734, and J1858-2216 with ELL1 binary model

Parameter	PSR J1142+0119	PSR J1630+3734	PSR J1858-2216
Right Ascension (RA, J2000)	$11^{\rm h}\,42^{\rm m}\,50\overset{\rm s}{.}145(3)$	$16^{\rm h}\,30^{\rm m}\,36\overset{\rm s}{.}46693(7)$	$18^{\rm h}\,58^{\rm m}\,17\overset{\rm s}{.}8792(8)$
Declination (DEC, J2000)	$+01^\circ\,19'\,35\overset{''}{.}69(9)$	$37^\circ\,34'\,42\overset{''}{.}097(1)$	$-22^\circ\,16'\,56\overset{''}{.}4(1)$
Galactic Longitude, l (°)	267.54	60.24	13.58
Galactic Latitude, b (°)	59.4	43.21	-11.39
Spin Period (ms)	5.0752983064042(5)	3.3181121293936(9)	2.3840129012370(2)
Period Derivative, $\dot{P}_{obs}$ (10^{-21}) ...	14.99(1)	10.77(9)	3.8(1)
Reference Epoch (MJD)	56315.0	56136.0	55800.0
Dispersion Measure ($pc\,cm^{-3}$)	19.197(1)	14.18009(7)	26.631(2)
Flux Density at 820 MHz (mJy) ..	0.23(5)	1.1(7)	0.4(2)
Binary Model	ELL1	ELL1	ELL1
Projected Semi-Major Axis (lt-s) .	1.531445(2)	9.039336(1)	19.603385(3)
Orbital Period, P_b (days)	1.583497340(1)	12.52502574(2)	46.0826044(2)
Epoch of Ascending Node (MJD) .	55796.0636781(5)	55980.2657727(2)	55513.4362591(9)
$\epsilon_1, e\cos(\omega)(10^{-6})$	$\sim$12.4	-42.2(1)	-126.2(3)
$\epsilon_2, e\cos(\omega)(10^{-6})$	$\sim$11.5	29.0(2)	-33.2(2)
Span of Timing Data (MJD)	55518 – 57246	55923 – 56349	55514 – 56093
Number of radio TOAs	191	117	138
RMS radio TOA Residual (μs) ...	15.822	1.8	10.65
Derived Parameters			
Proper Motion in RA ($\rm mas\,yr^{-1}$) .	-41(29)	2.4(3.5)	...
Proper Motion in DEC ($\rm mas\,yr^{-1}$)	-97(66)	-15.9(3.4)	...

Table 5.4—Continued

Parameter	PSR J1142+0119	PSR J1630+3734	PSR J1858-2216
Transverse velocity, V_T ($\mathrm{km\,s^{-1}}$)	$4(3)\times10^2$	$7(2)\times10^1$	...
Shklovskii effect, $\dot{P}_{shk}$ (10^{-21})	$1(1)\times10^2$	1.9(9)	...
Galactic potential effect, $\dot{P}_{gal}$ (10^{-21}) ...	0.5(1)	0.30(7)	0.22(5)
Intrinsic Period Derivative, $\dot{P}_{int}$ (10^{-21}) *†	14.5(1)	8.6(9)	3.6(1)
Mass Function ($M_\odot$)	0.001537984(5)	0.005055161(2)	0.003808921(1)
Minimum Companion Mass ($M_\odot$)	$\geq$0.15	$\geq$0.24	$\geq$0.21
DM-derived Distance (kpc)	0.9	0.9	0.9
Surface Magnetic Field (10^8 G)	2.7	1.7	0.9
Characteristic Age (Gyr)	5.5	6.1	10.4
Spin-down Luminosity, $\dot{E}$ ($10^{34}\,\mathrm{ergs\,s^{-1}}$) .	0.44	0.93	1.06
γ-ray Spectral Fit Parameters			
Fermi 5-Year Source (3FGL)	3FGL J1142.9+0120	3FGL J1630.2+3733	3FGL J1855.1-2243
TS	239	245	222
$\mathrm{TS_{cut}}$	16	32	46
$\mathrm{TS_{b\ free}}$	0	4	1
N_0 (10^{-12} $\mathrm{cm^{-2}\ s^{-1}\ MeV^{-1}}$)	$5.1\pm1.2^{+0.3}_{-0.2}$	1.4±0.4±0.1	2.0±0.6±0.1
Spectral Index Γ	1.4±0.3±0.1	1.1±0.4±0.1	0.8±0.4±0.1
E_C (GeV)	4.7±1.8±0.1	2.0±0.6±0.1	1.9±0.6±0.1
F_{100} (10^{-9} $\mathrm{cm^{-2}\ s^{-1}}$)	5.1±1.5±0.4	$6.1\pm2.3^{+0.7}_{-0.6}$	$6.3\pm1.8^{+0.5}_{-0.4}$
G_{100} (10^{-12} erg $\mathrm{cm^{-2}\ s^{-1}}$)	6.4±0.8±0.1	$6.9\pm1.0^{+0.3}_{-0.2}$	$9.0\pm1.0^{+0.5}_{-0.4}$
Pulsed Significance (σ)	8.2σ	6.1σ	15.5σ

Table 5.4—Continued

Parameter	PSR J1142+0119	PSR J1630+3734	PSR J1858-2216
γ-ray Efficiency, η (%)	14.1	7.19	8.23

*$\dot{P}_{int} = \dot{P}_{obs} - \dot{P}_{shk} - \dot{P}_{gal}$ when $\dot{P}_{shk}$ is available

†For PSR J1142+0119 the proper motion measurement is only $\sim 2\sigma$; therefore $\dot{P}_{shk}$ is not realiable. We used the $\dot{P}_{obs} - \dot{P}_{gal}$ as the $\dot{P}_{int}$ for this particular pulsar

Note. — Numbers in parentheses represent 1-σ uncertainties in the last digit for the timing parameters. Minimum companion masses were calculated assuming a pulsar mass of 1.4 $M_{\odot}$. The DM-distances were derived according to the NE2001 Galactic electron density model (Cordes & Lazio 2002) and likely have ∼20% uncertainties. The contribution in period derivative from the Shklovskii effect are included for the pulsar with significant measurement of proper motion.

Table 5.5. Best-fit Parameters for the MSPs J1921+0137, J2042+0246, and J2310-0555 with ELL1 binary model

Parameter	PSR J1921+0137	PSR J2042+0246	PSR J2310-0555
Right Ascension (RA, J2000)	$19^{\rm h}\ 21^{\rm m}\ 30\overset{\rm s}{.}30765(5)$	$20^{\rm h}\ 42^{\rm m}\ 11\overset{\rm s}{.}00287(5)$	$23^{\rm h}\ 10^{\rm m}\ 6\overset{\rm s}{.}430(4)$
Declination (DEC, J2000)	$01^\circ\ 37'\ 25\overset{''}{.}539(3)$	$02^\circ\ 46'\ 14\overset{''}{.}397(2)$	$-05^\circ\ 55'\ 35\overset{''}{.}9(1)$
Galactic Longitude, l (°)	37.83	48.99	69.7
Galactic Latitude, b (°)	-5.94	-23.02	-57.91
Spin Period (ms)	2.4963718144300(2)	4.5337267023282(3)	2.6125867919415(6)
Period Derivative, $\dot{P}_{obs}$ (10^{-21}) ...	19.35(3)	14.03(6)	4.96(4)
Reference Epoch (MJD)	57022.0	56520.0	56879.0
Dispersion Measure ($pc\,cm^{-3}$)	104.921197	9.2694(2)	15.5139(7)
Flux Density at 820 MHz (mJy) ..	0.4(1)	0.3(2)	0.18(8)
Binary Model	ELL1	ELL1	ELL1
Projected Semi-Major Axis (lt-s) .	7.726566(2)	24.5699969(8)	1.378352(2)
Orbital Period, P_b (days)	9.92929053(3)	77.2005806(3)	1.397095364(1)
Epoch of Ascending Node (MJD) .	56745.208691(1)	56123.669067(1)	56362.8169580(6)
$\epsilon_1, e\cos(\omega)(10^{-6})$	21.4(4)	-136.4(1)	...
$\epsilon_2, e\cos(\omega)(10^{-6})$	30.1(4)	-95.3(1)	...
Span of Timing Data (MJD)	56738 – 57304	56111 – 56916	56361 – 57396
Number of radio TOAs	124	197	118
RMS radio TOA Residual (μs) ...	12.67	6.34	10.49
Derived Parameters			
Proper Motion in RA ($\rm mas\,yr^{-1}$) .	...	15.1(1.2)	...
Proper Motion in DEC ($\rm mas\,yr^{-1}$)	...	-14.1(2.5)	...

Table 5.5—Continued

Parameter	PSR J1921+0137	PSR J2042+0246	PSR J2310-0555
Transverse velocity, V_T ($\mathrm{km\,s^{-1}}$)	...	$8(2)\times10^{1}$	...
Shklovskii effect, $\dot{P}_{shk}$ (10^{-21})	...	4(1)	...
Galactic potential effect, $\dot{P}_{gal}$ (10^{-21}) ...	1.3(5)	0.36(8)	0.18(4)
Intrinsic Period Derivative, $\dot{P}_{int}$ (10^{-21}) *	18.0(5)	10(1)	4.78(5)
Mass Function ($M_\odot$)	0.005023493(3)	0.0026721258(3)	0.001440492(6)
Minimum Companion Mass ($M_\odot$)	$\geq$0.24	$\geq$0.19	$\geq$0.15
DM-derived Distance (kpc)	3.5	0.8	0.7
Surface Magnetic Field (10^8 G)	2.1	2.1	1.1
Characteristic Age (Gyr)	2.2	7.2	8.7
Spin-down Luminosity, $\dot{E}$ ($10^{34}\,\mathrm{ergs\,s^{-1}}$)	4.57	0.42	1.06
γ-ray Spectral Fit Parameters			
Fermi 5-Year Source (3FGL)	3FGL J1921.2+0136	3FGL J2042.1+0247	3FGL J2310.1-0557
TS	...	0	...
$\mathrm{TS_{cut}}$	...	0	...
$\mathrm{TS_{b\ free}}$	...	0	...
N_0 (10^{-12} $\mathrm{cm^{-2}\ s^{-1}\ MeV^{-1}}$)	...	1.4±0.4±0.1	...
Spectral Index Γ	...	0±0.4±0.1	...
E_C (GeV)	...	0.0±0.6±0.1	...
F_{100} (10^{-9} $\mathrm{cm^{-2}\ s^{-1}}$)	...	$6.1\pm2.3^{+0.7}_{-0.6}$	...
G_{100} (10^{-12} erg $\mathrm{cm^{-2}\ s^{-1}}$)	...	$6.9\pm1.0^{+0.3}_{-0.2}$	...
Pulsed Significance (σ)	...	0σ	...

Table 5.5—Continued

Parameter	PSR J1921+0137	PSR J2042+0246	PSR J2310-0555
γ-ray Efficiency, η (%)	...	12.58	...

*$\dot{P}_{int} = \dot{P}_{obs} - \dot{P}_{shk} - \dot{P}_{gal}$ when $\dot{P}_{shk}$ is available

Note. — Numbers in parentheses represent 1-σ uncertainties in the last digit for the timing parameters. Minimum companion masses were calculated assuming a pulsar mass of 1.4 $M_{\odot}$. The DM-distances were derived according to the NE2001 Galactic electron density model (Cordes & Lazio 2002) and likely have $\sim$20% uncertainties. The contribution in period derivative from the Shklovskii effect are included for the pulsar with significant measurement of proper motion.

Table 5.6. Radio Searches of *Fermi* Unassociated Sources with the GBT

Source	R.A. J2000.0	Decl. J2000.0	l deg	b deg	Integration Time minutes	Observing Freq MHz	3FGL name
P7R40016	$00^h06^m17^s$	$+01^\circ35'08''$	100.4	-59.3	35	350	3FGL J0006.2+0135
P72Y0024	$00^h08^m07^s$	$+68^\circ33'49''$	119.0	6.0	55	820	3FGL J0008.5+6853
P72Y0024	$00^h08^m07^s$	$+68^\circ33'50''$	119.0	6.0	50	820	3FGL J0008.5+6853
P7R40023	$00^h08^m21^s$	$+14^\circ56'00''$	107.7	-46.7	35	350	3FGL J0008.3+1456
P7R40031 *	$00^h10^m30^s$	$-14^\circ25'10''$	84.0	-74.1	33	350	3FGL J0010.5−1425
P7R40076	$00^h28^m38^s$	$+75^\circ07'06''$	121.4	12.3	45	820	3FGL J0028.6+7507
P7R40076	$00^h28^m38^s$	$+75^\circ07'06''$	121.4	12.3	45	820	3FGL J0028.6+7507
1FGL J0039.2+4331	$00^h39^m01^s$	$+43^\circ28'08''$	120.5	-19.3	29	820	None
1FGL J0039.2+4331	$00^h39^m01^s$	$+43^\circ28'08''$	120.5	-19.3	5	820	None
2FGL J0039.1+4331	$00^h39^m07^s$	$+43^\circ31'38''$	120.6	-19.3	50	820	3FGL J0039.1+4330
1FGL J0046.8+5658	$00^h47^m02^s$	$+56^\circ56'50''$	122.3	-5.9	5	820	None
1FGL J0054.9−2455	$00^h54^m59^s$	$-24^\circ52'23''$	142.6	-87.6	5	820	None
1FGL J0106.7+4853	$01^h06^m35^s$	$+48^\circ55'29''$	125.5	-13.9	45	820	None
1FGL J0106.7+4853	$01^h06^m35^s$	$+48^\circ55'29''$	125.5	-13.9	5	820	None
1FGL J0106.7+4853	$01^h06^m35^s$	$+48^\circ55'30''$	125.5	-13.9	45	820	None
P72Y0218	$01^h27^m11^s$	$-08^\circ15'52''$	148.7	-69.3	50	820	3FGL J0127.1−0818
1FGL J0134.4+2632	$01^h34^m36^s$	$+26^\circ35'45''$	134.8	-35.3	45	820	None
1FGL J0134.4+2632	$01^h34^m36^s$	$+26^\circ35'45''$	134.8	-35.3	5	820	None
P7R40251	$01^h48^m20^s$	$+52^\circ00'36''$	131.8	-9.9	45	820	3FGL J0148.3+5200
P72Y0261	$01^h53^m07^s$	$+75^\circ16'01''$	126.9	12.9	50	820	3FGL J0152.8+7517
P72Y0294	$02^h03^m46^s$	$+30^\circ42'27''$	140.8	-29.6	40	820	3FGL J0203.6+3043
1FGL J0203.5+3044	$02^h03^m57^s$	$+30^\circ45'17''$	140.8	-29.6	5	820	None
P7R40308 *	$02^h11^m16^s$	$-06^\circ49'42''$	169.6	-62.2	50	350	3FGL J0211.2−0649
P7R40312 *	$02^h12^m08^s$	$+53^\circ20'09''$	134.9	-7.6	40	820	3FGL J0212.1+5320
2FGL J0212.1+5318	$02^h12^m09^s$	$+53^\circ18'18''$	134.9	-7.7	25	350	3FGL J0212.1+5320
2FGL J0212.1+5318	$02^h12^m09^s$	$+53^\circ18'20''$	134.9	-7.7	38	820	3FGL J0212.1+5320
P7R40312 *	$02^h12^m10^s$	$+53^\circ19'59''$	134.9	-7.6	45	820	3FGL J0212.1+5320
1FGL J0212.3+5319	$02^h12^m11^s$	$+53^\circ20'04''$	134.9	-7.6	45	820	None
1FGL J0212.3+5319	$02^h12^m11^s$	$+53^\circ20'04''$	134.9	-7.6	5	820	None
2FGL J0221.2+2516	$02^h21^m16^s$	$+25^\circ16'15''$	147.3	-33.3	42	820	3FGL J0221.2+2518
2FGL J0221.2+2516	$02^h21^m16^s$	$+25^\circ16'15''$	147.3	-33.3	5	820	3FGL J0221.2+2518
P7R40363 *	$02^h28^m01^s$	$+22^\circ48'01''$	150.3	-34.9	58	350	3FGL J0228.0+2248
P7R40378	$02^h32^m55^s$	$+26^\circ06'12''$	149.7	-31.4	45	820	3FGL J0232.9+2606
P7R40389 *	$02^h38^m00^s$	$+52^\circ37'46''$	138.8	-6.9	45	820	None
P7R40422 *	$02^h51^m06^s$	$+26^\circ03'42''$	153.9	-29.5	42	820	3FGL J0251.1+2603
1FGL J0258.0+2033	$02^h57^m40^s$	$+20^\circ25'40''$	158.9	-33.5	45	820	None
1FGL J0258.0+2033	$02^h57^m40^s$	$+20^\circ25'40''$	158.9	-33.5	5	820	None
P7R40452	$03^h04^m41^s$	$-06^\circ04'20''$	185.4	-52.0	53	820	None
P7R40452	$03^h04^m41^s$	$-06^\circ04'20''$	185.4	-52.0	53	820	None
P7R40452	$03^h04^m41^s$	$-06^\circ04'21''$	185.4	-52.0	45	820	None
1FGL J0311.3−0922	$03^h11^m21^s$	$-09^\circ24'03''$	191.4	-52.6	5	820	None

Table 5.6—Continued

Source	R.A. J2000.0	Decl. J2000.0	l deg	b deg	Integration Time minutes	Observing Freq MHz	3FGL name
P7R40463 *	$03^h12^m09^s$	$-09^\circ21'33''$	191.5	-52.4	28	820	3FGL J0312.1−0921
P72Y0468	$03^h12^m57^s$	$-22^\circ22'29''$	212.4	-57.6	28	820	3FGL J0312.7−2222
1FGL J0318.1+0254	$03^h17^m54^s$	$+02^\circ56'01''$	178.3	-43.6	45	820	None
1FGL J0318.1+0254	$03^h17^m54^s$	$+02^\circ56'01''$	178.3	-43.6	5	820	None
2FGL J0318.0+0255	$03^h18^m01^s$	$+02^\circ55'36''$	178.4	-43.6	6	820	3FGL J0318.1+0252
2FGL J0318.0+0255	$03^h18^m01^s$	$+02^\circ55'37''$	178.4	-43.6	50	820	3FGL J0318.1+0252
P7R40505	$03^h30^m39^s$	$+04^\circ37'44''$	179.5	-40.1	37	820	3FGL J0330.6+0437
P7R40509	$03^h32^m00^s$	$+63^\circ08'52''$	139.9	5.7	45	820	3FGL J0332.0+6308
24M0388	$03^h32^m31^s$	$-11^\circ18'00''$	198.2	-49.0	45	820	None
24M0388	$03^h32^m31^s$	$-11^\circ18'00''$	198.2	-49.0	5	820	None
P7R40512 *	$03^h33^m28^s$	$+40^\circ03'05''$	153.6	-13.0	45	820	3FGL J0333.4+4003
P72Y0524	$03^h34^m34^s$	$+78^\circ47'21''$	130.6	18.4	50	820	None
2FGL J0336.0+7504	$03^h36^m00^s$	$+75^\circ04'45''$	133.1	15.5	50	820	3FGL J0336.1+7500
P7R40522 *	$03^h36^m08^s$	$+75^\circ00'38''$	133.1	15.5	45	820	3FGL J0336.1+7500
24M0400	$03^h36^m55^s$	$+32^\circ05'24''$	159.2	-18.9	45	820	3FGL J0336.5+3210
24M0400	$03^h36^m55^s$	$+32^\circ05'24''$	159.2	-18.9	5	820	3FGL J0336.5+3210
P7R40535	$03^h40^m25^s$	$-02^\circ22'26''$	188.8	-42.6	40	350	None
P72Y0550	$03^h45^m37^s$	$+32^\circ39'31''$	160.3	-17.3	36	820	3FGL J0345.3+3236
24M0444	$03^h59^m00^s$	$+60^\circ02'24''$	144.4	5.2	45	820	3FGL J0358.8+6002
24M0444	$03^h59^m00^s$	$+60^\circ02'24''$	144.4	5.2	5	820	3FGL J0358.8+6002
24M0453	$04^h01^m36^s$	$-20^\circ36'00''$	215.0	-46.3	20	820	None
24M0453	$04^h01^m36^s$	$-20^\circ36'00''$	215.0	-46.3	5	820	None
P7R40591A *	$04^h12^m05^s$	$+02^\circ29'44''$	189.6	-33.4	40	350	3FGL J0412.0+0229
P7R40602 *	$04^h19^m06^s$	$+66^\circ36'19''$	141.5	11.6	45	820	3FGL J0419.1+6636
2FGL J0423.4+5612	$04^h23^m26^s$	$+56^\circ12'21''$	149.4	4.6	50	820	None
1FGL J0426.5+5437	$04^h26^m41^s$	$+54^\circ35'45''$	150.9	3.9	45	820	None
1FGL J0426.5+5437	$04^h26^m41^s$	$+54^\circ35'45''$	150.9	3.9	5	820	None
2FGL J0426.7+5434	$04^h26^m45^s$	$+54^\circ34'51''$	150.9	3.9	50	820	3FGL J0426.7+5437
2FGL J0428.0−3845	$04^h28^m03^s$	$-38^\circ45'41''$	241.8	-43.8	39	820	None
2FGL J0428.0−3845	$04^h28^m03^s$	$-38^\circ45'41''$	241.8	-43.8	5	820	None
2FGL J0430.2+3508c	$04^h30^m15^s$	$+35^\circ08'57''$	165.5	-9.1	50	820	None
2FGL J0430.2+3508c	$04^h30^m15^s$	$+35^\circ08'57''$	165.5	-9.1	5	820	None
P72Y0641	$04^h32^m14^s$	$+55^\circ55'41''$	150.5	5.3	40	820	None
1FGL J0448.6+1118	$04^h48^m56^s$	$+11^\circ22'10''$	187.4	-20.8	5	820	None
P72Y0703	$05^h00^m06^s$	$+52^\circ36'13''$	155.6	6.3	45	820	3FGL J0500.3+5237
P72Y1005	$05^h18^m08^s$	$+55^\circ04'21''$	155.2	9.9	33	820	None
1FGL J0523.5−2529	$05^h23^m27^s$	$-25^\circ29'47''$	228.2	-29.8	45	820	None
1FGL J0523.5−2529	$05^h23^m27^s$	$-25^\circ29'47''$	228.2	-29.8	5	820	None
P7R40759	$05^h26^m26^s$	$+22^\circ47'54''$	182.9	-6.9	35	820	3FGL J0526.4+2247
P72Y0772	$05^h26^m59^s$	$+66^\circ48'14''$	145.5	17.0	45	820	3FGL J0527.3+6647
24M0660	$05^h29^m21^s$	$+09^\circ38'25''$	194.6	-13.4	45	820	3FGL J0529.1+0933

Table 5.6—Continued

Source	R.A. J2000.0	Decl. J2000.0	l deg	b deg	Integration Time minutes	Observing Freq MHz	3FGL name
24M0660	$05^h29^m21^s$	$+09^\circ38'25''$	194.6	-13.4	5	820	3FGL J0529.1+0933
2FGL J0533.9+6759 †	$05^h33^m57^s$	$+67^\circ59'51''$	144.8	18.2	41	820	3FGL J0534.0+6759
2FGL J0533.9+6759 †	$05^h33^m57^s$	$+67^\circ59'51''$	144.8	18.2	5	820	3FGL J0534.0+6759
2FGL J0534.8−0548c	$05^h34^m52^s$	$-05^\circ48'42''$	209.4	-19.7	50	820	None
2FGL J0534.9−0450c	$05^h34^m54^s$	$-04^\circ50'17''$	208.4	-19.2	5	820	None
1FGL J0536.2−0607c	$05^h36^m05^s$	$-06^\circ10'04''$	209.8	-19.6	30	820	None
1FGL J0536.2−0607c	$05^h36^m05^s$	$-06^\circ10'04''$	209.8	-19.6	5	820	None
2FGL J0538.5−0534c	$05^h38^m35^s$	$-05^\circ34'28''$	209.6	-18.7	32	820	3FGL J0539.2−0536
1FGL J0539.4−0400	$05^h40^m08^s$	$-04^\circ02'56''$	208.3	-17.7	45	820	None
1FGL J0539.4−0400	$05^h40^m08^s$	$-04^\circ02'56''$	208.3	-17.7	5	820	None
2FGL J0541.8−0203c	$05^h41^m48^s$	$-02^\circ03'38''$	206.7	-16.4	30	350	None
2FGL J0541.8−0203c	$05^h41^m49^s$	$-02^\circ03'37''$	206.7	-16.4	50	820	None
P72Y0835	$05^h41^m50^s$	$-01^\circ49'55''$	206.5	-16.3	40	350	None
P72Y0835	$05^h41^m50^s$	$-01^\circ49'55''$	206.5	-16.3	60	350	None
P72Y0835	$05^h41^m50^s$	$-01^\circ49'56''$	206.5	-16.3	45	820	None
2FGL J0543.2−0120c	$05^h43^m14^s$	$-01^\circ20'08''$	206.2	-15.8	38	820	None
2FGL J0543.2−0120c	$05^h43^m14^s$	$-01^\circ20'08''$	206.2	-15.8	5	820	None
2FGL J0545.6+6018	$05^h45^m38^s$	$+60^\circ18'51''$	152.5	15.7	35	350	3FGL J0545.6+6019
1FGL J0547.0+0020c	$05^h47^m03^s$	$-04^\circ02'56''$	209.2	-16.2	45	820	None
1FGL J0547.0+0020c	$05^h47^m03^s$	$-04^\circ02'56''$	209.2	-16.2	5	820	None
2FGL J0547.1+0020c	$05^h47^m11^s$	$-02^\circ03'38''$	207.3	-15.2	26	350	3FGL J0546.4+0031c
2FGL J0547.5−0141c	$05^h47^m31^s$	$-01^\circ41'11''$	207.0	-15.0	30	350	None
2FGL J0547.5−0141c	$05^h47^m31^s$	$-01^\circ41'11''$	207.0	-15.0	48	820	None
P72Y0859	$05^h53^m26^s$	$-20^\circ35'05''$	225.7	-21.7	40	350	3FGL J0553.5−2036
1FGL J0553.9+3105	$05^h53^m56^s$	$+31^\circ07'07''$	179.1	2.7	5	820	None
1FGL J0553.9+3105	$05^h53^m56^s$	$+31^\circ07'07''$	179.1	2.7	5	820	None
P72Y0862	$05^h54^m40^s$	$+03^\circ04'56''$	203.6	-11.2	45	350	None
1FGL J0600.5−2006	$06^h01^m01^s$	$-19^\circ54'00''$	225.8	-19.7	5	820	None
2FGL J0605.3+3758 †	$06^h05^m23^s$	$+37^\circ58'45''$	174.2	8.1	11	820	3FGL J0605.0+3756
2FGL J0605.3+3758 †	$06^h05^m23^s$	$+37^\circ58'45''$	174.2	8.1	12	820	3FGL J0605.0+3756
2FGL J0605.3+3758 †	$06^h05^m23^s$	$+37^\circ58'45''$	174.2	8.1	1	820	3FGL J0605.0+3756
2FGL J0605.3+3758 †	$06^h05^m23^s$	$+37^\circ58'46''$	174.2	8.1	11	820	3FGL J0605.0+3756
2FGL J0605.3+3758 †	$06^h05^m23^s$	$+37^\circ58'46''$	174.2	8.1	12	820	3FGL J0605.0+3756
2FGL J0605.3+3758 †	$06^h05^m23^s$	$+37^\circ58'46''$	174.2	8.1	50	820	3FGL J0605.0+3756
1FGL J0605.3+3800	$06^h05^m24^s$	$+37^\circ58'06''$	174.2	8.1	5	820	None
1FGL J0605.3+3800	$06^h05^m24^s$	$+37^\circ58'07''$	174.2	8.1	5	820	None
2FGL J0605.3+3758 †	$06^h05^m24^s$	$+37^\circ58'51''$	174.2	8.1	10	820	3FGL J0605.0+3756
1FGL J0608.1−0630c	$06^h08^m17^s$	$-06^\circ17'02''$	213.7	-12.4	45	820	None
P72Y0892	$06^h08^m31^s$	$-06^\circ10'02''$	213.6	-12.3	40	350	None
P7R40880 *	$06^h11^m43^s$	$+27^\circ59'52''$	183.7	4.5	45	820	3FGL J0611.7+2759
2FGL J0616.6+2425	$06^h16^m36^s$	$+24^\circ25'15''$	187.4	3.8	50	820	None

Table 5.6—Continued

Source	R.A. J2000.0	Decl. J2000.0	l deg	b deg	Integration Time minutes	Observing Freq MHz	3FGL name
2FGL J0616.6+2425	$06^h16^m36^s$	$+24^\circ25'15''$	187.4	3.8	5	820	None
1FGL J0621.5+2508	$06^h21^m13^s$	$+25^\circ10'31''$	187.2	5.1	45	820	None
1FGL J0621.5+2508	$06^h21^m13^s$	$+25^\circ10'31''$	187.2	5.1	5	820	None
2FGL J0621.2+2508	$06^h21^m15^s$	$+25^\circ08'20''$	187.2	5.0	50	820	3FGL J0621.0+2514
2FGL J0621.2+2508	$06^h21^m15^s$	$+25^\circ08'20''$	187.2	5.0	5	820	3FGL J0621.0+2514
1FGL J0622.2+3751	$06^h21^m59^s$	$+37^\circ51'36''$	175.8	10.9	5	820	None
1FGL J0622.2+3751	$06^h21^m59^s$	$+37^\circ51'36''$	175.8	10.9	5	820	None
24M0825	$06^h32^m35^s$	$+04^\circ27'36''$	206.8	-2.1	45	820	None
24M0825	$06^h32^m35^s$	$+04^\circ27'36''$	206.8	-2.1	5	820	None
1FGL J0643.2+0859	$06^h43^m14^s$	$+08^\circ58'40''$	204.0	2.3	45	820	None
1FGL J0643.2+0859	$06^h43^m14^s$	$+08^\circ58'40''$	204.0	2.3	5	820	None
P7R41060 *	$07^h40^m55^s$	$+66^\circ22'30''$	149.7	29.6	33	820	3FGL J0740.8+6621
P72Y1109	$07^h44^m10^s$	$+17^\circ18'42''$	202.8	19.2	35	350	3FGL J0744.3+1715
P72Y1109	$07^h44^m10^s$	$+17^\circ18'42''$	202.8	19.2	35	350	3FGL J0744.3+1715
P7R41204 *	$08^h38^m47^s$	$-28^\circ28'41''$	250.6	7.8	30	820	3FGL J0838.8−2829
2FGL J0838.8−2828	$08^h38^m51^s$	$-28^\circ28'32''$	250.6	7.8	5	820	3FGL J0838.8−2829
2FGL J0841.3−3556	$08^h41^m21^s$	$-35^\circ56'21''$	256.9	3.7	50	820	3FGL J0841.3−3554
2FGL J0841.3−3556	$08^h41^m21^s$	$-35^\circ56'21''$	256.9	3.7	5	820	3FGL J0841.3−3554
1FGL J0843.4+6718	$08^h43^m38^s$	$+67^\circ15'56''$	147.7	35.6	34	820	None
1FGL J0843.4+6718	$08^h43^m38^s$	$+67^\circ15'56''$	147.7	35.6	5	820	None
P72Y1279	$08^h49^m18^s$	$-29^\circ13'21''$	252.6	9.2	30	820	3FGL J0849.5−2912
P72Y1280	$08^h49^m47^s$	$+51^\circ09'47''$	167.6	39.1	61	820	3FGL J0849.9+5108
24M1109.2	$08^h54^m52^s$	$+71^\circ51'00''$	142.0	35.1	45	820	3FGL J0855.4+7142
24M1109.2	$08^h54^m52^s$	$+71^\circ51'00''$	142.0	35.1	5	820	3FGL J0855.4+7142
1FGL J0856.6+2103	$08^h56^m32^s$	$+20^\circ59'04''$	206.0	36.5	45	820	None
P72Y1389	$09^h35^m45^s$	$+09^\circ02'21''$	224.8	40.5	35	350	3FGL J0935.2+0903
P72Y1389	$09^h35^m45^s$	$+09^\circ02'22''$	224.8	40.5	28	350	3FGL J0935.2+0903
P72Y1389	$09^h35^m45^s$	$+09^\circ02'22''$	224.8	40.5	34	820	3FGL J0935.2+0903
2FGL J0953.6−1504	$09^h53^m35^s$	$-15^\circ08'32''$	251.9	29.6	27	350	3FGL J0953.7−1510
P72Y1445	$10^h03^m46^s$	$+26^\circ10'32''$	204.6	52.7	35	350	3FGL J1003.6+2608
P72Y1445	$10^h03^m46^s$	$+26^\circ10'32''$	204.6	52.7	35	350	3FGL J1003.6+2608
P72Y1445	$10^h03^m46^s$	$+26^\circ10'32''$	204.6	52.7	35	350	3FGL J1003.6+2608
P7R41464	$10^h27^m51^s$	$+82^\circ53'52''$	127.9	32.8	45	820	3FGL J1027.8+8253
P72Y1529	$10^h32^m07^s$	$+66^\circ25'24''$	141.9	45.2	55	820	3FGL J1032.5+6623
P72Y1549	$10^h40^m58^s$	$-12^\circ05'01''$	259.8	39.6	35	350	3FGL J1040.9−1205
P72Y1549	$10^h40^m58^s$	$-12^\circ05'01''$	259.8	39.6	35	350	3FGL J1040.9−1205
P72Y1549	$10^h40^m58^s$	$-12^\circ05'01''$	259.8	39.6	35	350	3FGL J1040.9−1205
SEED3Y-103	$10^h50^m30^s$	$+04^\circ36'01''$	245.6	53.4	35	350	3FGL J1050.4+0435
SEED3Y-103	$10^h50^m30^s$	$+04^\circ36'01''$	245.6	53.4	35	350	3FGL J1050.4+0435
P72Y1633	$11^h06^m36^s$	$-17^\circ43'24''$	270.4	38.4	35	350	3FGL J1106.6−1744
SEED3Y-110	$11^h18^m25^s$	$-04^\circ14'13''$	263.8	51.4	35	350	3FGL J1118.2−0411

Table 5.6—Continued

Source	R.A. J2000.0	Decl. J2000.0	l deg	b deg	Integration Time minutes	Observing Freq MHz	3FGL name
SEED3Y-110	$11^h18^m25^s$	$-04^\circ14'13''$	263.8	51.4	35	350	3FGL J1118.2−0411
P7R41624	$11^h19^m56^s$	$-22^\circ04'02''$	276.5	36.1	49	820	3FGL J1119.9−2204
2FGL J1120.0−2204	$11^h20^m00^s$	$-22^\circ04'50''$	276.5	36.1	44	820	3FGL J1119.9−2204
2FGL J1120.0−2204	$11^h20^m00^s$	$-22^\circ04'50''$	276.5	36.1	5	820	3FGL J1119.9−2204
1FGL J1123.6−2528	$11^h23^m39^s$	$-25^\circ27'24''$	279.1	33.3	5	820	None
P72Y1698	$11^h26^m56^s$	$-18^\circ57'21''$	276.7	39.6	50	820	3FGL J1127.0−1857
P72Y1724 †	$11^h35^m35^s$	$+75^\circ28'10''$	129.1	40.7	35	350	3FGL J1136.1+7523
1FGL J1142.7+0127 †	$11^h42^m52^s$	$+01^\circ20'54''$	267.5	59.4	5	820	None
1FGL J1142.7+0127 †	$11^h42^m53^s$	$+01^\circ20'54''$	267.5	59.4	5	820	None
P72Y1813	$12^h12^m29^s$	$+51^\circ28'53''$	137.1	64.6	35	820	3FGL J1212.6+5135
2FGL J1226.0+2953	$12^h26^m04^s$	$+29^\circ53'46''$	185.0	83.8	50	820	3FGL J1225.9+2953
1FGL J1249.8+3706	$12^h49^m42^s$	$+37^\circ05'13''$	124.9	80.0	45	820	None
2FGL J1311.7−3429	$13^h11^m46^s$	$-34^\circ29'19''$	307.7	28.2	5	820	3FGL J1311.8−3430
1FGL J1311.7−3429	$13^h11^m48^s$	$-34^\circ29'48''$	307.7	28.2	38	820	None
1FGL J1311.7−3429	$13^h11^m48^s$	$-34^\circ29'48''$	307.7	28.2	5	820	None
1FGL J1311.7−3429	$13^h11^m48^s$	$-34^\circ29'48''$	307.7	28.2	5	820	None
1FGL J1312.6+0048 †	$13^h12^m42^s$	$-34^\circ29'48''$	307.9	28.2	5	820	None
1FGL J1416.2−1001	$14^h15^m02^s$	$-10^\circ01'24''$	334.4	47.7	45	820	None
SEED3Y-29	$14^h18^m26^s$	$+35^\circ42'21''$	63.2	69.6	40	820	3FGL J1418.5+3543
P7R42122 *	$14^h21^m02^s$	$-24^\circ31'39''$	327.7	34.0	45	820	3FGL J1421.0−2431
P72Y2198	$14^h22^m51^s$	$+58^\circ02'55''$	101.8	55.2	45	820	3FGL J1422.8+5801
P72Y2219	$14^h32^m59^s$	$+76^\circ49'27''$	115.7	38.8	45	820	None
2FGL J1511.8−0513	$15^h11^m52^s$	$-05^\circ13'23''$	354.6	43.1	45	820	3FGL J1511.8−0513
2FGL J1513.5−2546	$15^h13^m31^s$	$-25^\circ46'01''$	338.9	27.0	35	350	3FGL J1513.4−2549
2FGL J1513.5−2546	$15^h13^m31^s$	$-25^\circ46'01''$	338.9	27.0	35	350	3FGL J1513.4−2549
P7R42252 *	$15^h13^m31^s$	$-25^\circ49'52''$	338.9	27.0	35	820	3FGL J1513.4−2549
P7R42258 *	$15^h16^m46^s$	$+36^\circ48'30''$	59.7	57.9	40	820	3FGL J1516.7+3648
1FGL J1519.7+4216	$15^h20^m41^s$	$+42^\circ11'40''$	69.2	56.2	45	820	None
SEED3Y-284	$15^h32^m40^s$	$-13^\circ18'37''$	352.1	33.7	35	820	3FGL J1532.7−1319
1FGL J1539.0−3328	$15^h39^m10^s$	$-33^\circ26'30''$	338.7	17.5	5	820	None
2FGL J1539.2−3325	$15^h39^m15^s$	$-33^\circ25'42''$	338.7	17.5	5	820	3FGL J1539.2−3324
P7R42328	$15^h44^m00^s$	$-25^\circ55'46''$	344.7	22.6	45	820	3FGL J1544.1−2555
1FGL J1544.5−1127	$15^h44^m35^s$	$-11^\circ25'33''$	356.2	33.0	5	820	None
P7R42354 *	$15^h53^m10^s$	$+54^\circ37'27''$	85.6	47.2	45	820	3FGL J1553.1+5437
P72Y2431	$15^h59^m57^s$	$+23^\circ20'34''$	38.7	47.4	33	820	3FGL J1559.9+2319
P7R42383 *	$16^h01^m57^s$	$+23^\circ06'38''$	38.5	46.9	45	820	3FGL J1601.9+2306
2FGL J1602.4+2308	$16^h02^m28^s$	$+23^\circ08'27''$	38.6	46.8	50	820	3FGL J1601.9+2306
2FGL J1602.4+2308	$16^h02^m28^s$	$+23^\circ08'27''$	38.6	46.8	5	820	3FGL J1601.9+2306
P7R42434	$16^h22^m57^s$	$-03^\circ12'13''$	10.8	30.7	45	820	3FGL J1622.9−0312
2FGL J1624.2−2124	$16^h24^m17^s$	$-21^\circ24'39''$	355.1	19.3	35	350	None
P7R42443 *	$16^h25^m07^s$	$-03^\circ12'13''$	11.1	30.3	45	820	None

Table 5.6—Continued

Source	R.A. J2000.0	Decl. J2000.0	l deg	b deg	Integration Time minutes	Observing Freq MHz	3FGL name
2FGL J1625.2−0020	$16^h25^m12^s$	$-01^\circ41'11''$	12.6	31.1	45	820	3FGL J1625.1−0021
1FGL J1625.3−0019	$16^h25^m14^s$	$-34^\circ29'48''$	345.2	10.3	45	820	None
1FGL J1625.3−0019	$16^h25^m14^s$	$-34^\circ29'48''$	345.2	10.3	5	820	None
P7R42457 *	$16^h27^m52^s$	$+32^\circ17'42''$	53.0	43.2	40	820	3FGL J1627.8+3217
1FGL J1627.6+3218	$16^h27^m54^s$	$+32^\circ19'58''$	53.0	43.2	30	820	None
1FGL J1627.6+3218	$16^h27^m54^s$	$+32^\circ19'58''$	53.0	43.2	5	820	None
1FGL J1627.8−3204	$16^h28^m10^s$	$-32^\circ04'39''$	347.4	11.5	45	820	None
2FGL J1630.3+3732 †	$16^h30^m23^s$	$+37^\circ32'55''$	60.2	43.3	11	820	3FGL J1630.2+3733
2FGL J1630.3+3732 †	$16^h30^m23^s$	$+37^\circ32'55''$	60.2	43.3	12	820	3FGL J1630.2+3733
2FGL J1630.3+3732 †	$16^h30^m23^s$	$+37^\circ32'55''$	60.2	43.3	5	820	3FGL J1630.2+3733
2FGL J1632.6−2328c	$16^h32^m37^s$	$-23^\circ28'21''$	354.8	16.4	17	350	None
P7R42530 *	$16^h49^m40^s$	$-30^\circ07'45''$	352.0	9.3	45	820	3FGL J1649.6−3007
2FGL J1653.6−0159	$16^h53^m36^s$	$-01^\circ59'47''$	16.6	24.9	49	820	3FGL J1653.6−0158
2FGL J1653.6−0159	$16^h53^m38^s$	$-01^\circ58'36''$	16.6	24.9	10	820	3FGL J1653.6−0158
1FGL J1653.6−0158	$16^h53^m39^s$	$-01^\circ58'21''$	16.6	24.9	45	820	None
P72Y2613	$16^h56^m02^s$	$+20^\circ46'17''$	40.6	34.3	53	820	3FGL J1656.0+2044
P72Y2627	$16^h57^m58^s$	$+61^\circ50'33''$	91.6	37.0	61	820	None
P7R42562	$16^h59^m05^s$	$-01^\circ42'06''$	17.6	23.9	45	820	3FGL J1659.0−0142
P7R42580G	$17^h03^m40^s$	$-28^\circ51'32''$	354.9	7.6	45	820	3FGL J1703.6−2850
P7R42603 *	$17^h11^m46^s$	$-19^\circ23'21''$	3.8	11.7	57	350	None
P7R42606G	$17^h13^m52^s$	$-29^\circ27'14''$	355.7	5.5	45	820	None
P7R42606G	$17^h13^m52^s$	$-29^\circ27'14''$	355.7	5.5	45	820	None
P72Y2678	$17^h14^m00^s$	$-06^\circ16'22''$	15.5	18.4	22	350	None
2FGL J1716.6−0526c	$17^h16^m40^s$	$-05^\circ26'28''$	16.6	18.2	5	820	None
P7R42631	$17^h20^m45^s$	$+07^\circ11'21''$	29.0	23.4	28	820	3FGL J1720.7+0711
2FGL J1722.5−0420	$17^h22^m34^s$	$-04^\circ20'40''$	18.4	17.5	39	820	3FGL J1722.7−0415
2FGL J1727.8−2308	$17^h27^m50^s$	$-23^\circ08'42''$	2.8	6.5	42	820	None
2FGL J1727.8−2308	$17^h27^m50^s$	$-23^\circ08'42''$	2.8	6.5	5	820	None
P7R42654G	$17^h28^m13^s$	$-16^\circ10'08''$	8.7	10.2	45	820	None
1FGL J1730.7−0352	$17^h30^m36^s$	$-03^\circ53'17''$	19.9	16.0	5	820	None
2FGL J1730.6−2409	$17^h30^m37^s$	$-24^\circ09'39''$	2.3	5.4	50	820	3FGL J1729.7−2408
2FGL J1730.6−0353	$17^h30^m38^s$	$-03^\circ53'42''$	19.9	16.0	45	820	3FGL J1730.6−0357
2FGL J1730.6−0353	$17^h30^m38^s$	$-03^\circ53'42''$	19.9	16.0	50	820	3FGL J1730.6−0357
2FGL J1730.6−0353	$17^h30^m38^s$	$-03^\circ53'42''$	19.9	16.0	50	820	3FGL J1730.6−0357
2FGL J1730.6−0353	$17^h30^m38^s$	$-03^\circ53'42''$	19.9	16.0	5	820	3FGL J1730.6−0357
P7R42709A *	$17^h43^m58^s$	$-13^\circ10'42''$	13.3	8.5	40	820	3FGL J1743.9−1310
1FGL J1746.7−3233	$17^h46^m40^s$	$-32^\circ36'17''$	357.0	-2.1	45	820	None
1FGL J1746.7−3233	$17^h46^m40^s$	$-32^\circ36'17''$	357.0	-2.1	45	820	None
1FGL J1746.7−3233	$17^h46^m40^s$	$-32^\circ36'17''$	357.0	-2.1	5	820	None
1FGL J1746.7−3233	$17^h46^m40^s$	$-32^\circ36'17''$	357.0	-2.1	5	820	None
P72Y2820	$17^h49^m48^s$	$-03^\circ05'26''$	23.0	12.2	27	820	3FGL J1749.7−0305

Table 5.6—Continued

Source	R.A. J2000.0	Decl. J2000.0	l deg	b deg	Integration Time minutes	Observing Freq MHz	3FGL name
1FGL J1749.5−0301	$17^h49^m51^s$	$-03^\circ04'20''$	23.0	12.2	5	820	None
SEED_09-94	$17^h57^m11^s$	$+70^\circ31'48''$	101.0	30.0	45	820	3FGL J1756.9+7032
1FGL J1806.2+0609	$18^h05^m50^s$	$+06^\circ12'27''$	33.3	13.0	45	820	None
1FGL J1806.2+0609	$18^h05^m50^s$	$+06^\circ12'27''$	33.3	13.0	5	820	None
2FGL J1805.8+0612	$18^h05^m51^s$	$+06^\circ12'48''$	33.3	13.0	45	820	3FGL J1805.9+0614
SEED_09-122	$18^h08^m00^s$	$+34^\circ54'44''$	61.5	23.5	50	820	3FGL J1809.0+3517
2FGL J1808.3−3356	$18^h08^m22^s$	$-33^\circ56'04''$	358.1	-6.7	50	820	3FGL J1808.3−3357
P7R42794 *	$18^h08^m23^s$	$-33^\circ57'46''$	358.1	-6.7	63	820	3FGL J1808.3−3357
P7R42794 *	$18^h08^m23^s$	$-33^\circ57'47''$	358.1	-6.7	45	820	3FGL J1808.3−3357
2FGL J1729.5−0854	$18^h10^m18^s$	$-11^\circ03'57''$	18.4	3.9	35	350	3FGL J1729.9−0859
2FGL J1816.5+4511	$18^h16^m35^s$	$+45^\circ11'57''$	72.9	24.7	21	820	3FGL J1816.5+4512
24M2244	$18^h19^m23^s$	$-15^\circ31'12''$	15.5	-0.1	5	820	3FGL J1818.7−1528
P7R42830B *	$18^h20^m24^s$	$-32^\circ17'09''$	0.7	-8.2	39	350	3FGL J1820.4−3217
2FGL J1820.6−3219	$18^h20^m38^s$	$-32^\circ19'23''$	0.7	-8.2	50	820	3FGL J1820.4−3217
SEED3Y-344	$18^h22^m26^s$	$+66^\circ34'47''$	96.5	27.6	40	820	None
P7R42854 *	$18^h27^m20^s$	$-14^\circ46'01''$	17.1	-1.5	35	820	3FGL J1826.2−1450
P7R42856	$18^h27^m42^s$	$+11^\circ41'50''$	40.8	10.5	45	820	3FGL J1827.7+1141
2FGL J1829.8−0204c	$18^h29^m48^s$	$-02^\circ04'35''$	28.6	3.9	34	820	3FGL J1829.9−0203c
2FGL J1829.8−0204c	$18^h29^m48^s$	$-02^\circ04'35''$	28.6	3.9	5	820	3FGL J1829.9−0203c
P7R42871 *	$18^h30^m50^s$	$-31^\circ36'09''$	2.4	-9.8	50	820	3FGL J1830.8−3136
2FGL J1832.0−0200	$18^h32^m00^s$	$-02^\circ00'59''$	28.9	3.4	44	820	3FGL J1831.7−0157c
2FGL J1832.0−0200	$18^h32^m00^s$	$-02^\circ00'59''$	28.9	3.4	5	820	3FGL J1831.7−0157c
P7R42896 *	$18^h39^m23^s$	$-05^\circ52'53''$	26.3	-0.0	33	820	3FGL J1838.9−0537
24M2314	$18^h42^m07^s$	$+27^\circ40'13''$	57.1	14.1	45	820	3FGL J1842.2+2742
24M2314	$18^h42^m07^s$	$+27^\circ40'13''$	57.1	14.1	5	820	3FGL J1842.2+2742
P7R42910	$18^h42^m15^s$	$+27^\circ42'08''$	57.1	14.1	50	820	3FGL J1842.2+2742
2FGL J1842.3+2740	$18^h42^m19^s$	$+27^\circ40'15''$	57.1	14.1	35	350	3FGL J1842.2+2742
P7R42921	$18^h45^m32^s$	$-25^\circ24'32''$	9.4	-10.1	40	820	3FGL J1845.5−2524
P72Y3022	$18^h48^m24^s$	$+32^\circ31'43''$	62.3	14.8	56	820	3FGL J1848.4+3216
P7R42929 *	$18^h48^m38^s$	$+32^\circ33'26''$	62.3	14.7	45	820	3FGL J1848.4+3216
P7R42948GP †	$18^h55^m57^s$	$-14^\circ38'55''$	20.3	-7.6	45	820	None
1FGL J1858.1−2218 †	$18^h58^m28^s$	$-22^\circ18'55''$	13.6	-11.4	46	820	None
1FGL J1858.1−2218 †	$18^h58^m28^s$	$-22^\circ18'55''$	13.6	-11.4	5	820	None
1FGL J1858.1−2218 †	$18^h58^m28^s$	$-22^\circ18'55''$	13.6	-11.4	5	820	None
P7R42980	$19^h04^m47^s$	$-07^\circ08'17''$	28.1	-6.2	35	820	3FGL J1904.7−0708
2FGL J1904.9−3720c	$19^h04^m55^s$	$-37^\circ20'00''$	359.8	-18.5	25	820	None
2FGL J1904.9−3720c	$19^h04^m55^s$	$-37^\circ20'00''$	359.8	-18.5	5	820	None
P72Y3081	$19^h06^m38^s$	$+07^\circ19'18''$	41.2	-0.0	45	820	3FGL J1906.6+0720
1FGL J1908.5−0138	$19^h08^m51^s$	$-01^\circ34'43''$	33.5	-4.6	5	820	None
P7R42990A *	$19^h09^m32^s$	$+21^\circ02'54''$	53.7	5.6	45	350	None
P7R43023A *†	$19^h21^m13^s$	$+01^\circ36'27''$	37.8	-5.9	45	820	3FGL J1921.2+0136

Table 5.6—Continued

Source	R.A. J2000.0	Decl. J2000.0	l deg	b deg	Integration Time minutes	Observing Freq MHz	3FGL name
P7R43038 *	$19^h25^m29^s$	$+17^\circ27'47''$	52.3	0.6	35	820	3FGL J1925.4+1727
P7R43071	$19^h44^m08^s$	$+39^\circ19'51''$	73.5	7.6	25	820	3FGL J1944.1+3919
P7R43082	$19^h49^m01^s$	$+13^\circ12'36''$	51.3	-6.4	45	820	3FGL J1949.0+1312
SEED3Y-762	$19^h49^m09^s$	$+13^\circ10'51''$	51.3	-6.4	45	820	3FGL J1949.0+1312
P72Y3203	$19^h55^m50^s$	$+02^\circ12'52''$	42.4	-13.2	45	820	3FGL J1955.9+0212
P7R43125 *	$20^h00^m06^s$	$+42^\circ12'33''$	77.5	6.4	45	820	3FGL J2000.1+4212
P7R43137	$20^h04^m52^s$	$+70^\circ03'33''$	102.9	19.5	45	820	3FGL J2004.8+7003
P7R43143 *	$20^h06^m38^s$	$+01^\circ50'45''$	43.4	-15.8	29	820	3FGL J2006.6+0150
P7R43172	$20^h16^m24^s$	$-09^\circ05'00''$	34.3	-23.0	45	820	3FGL J2016.4−0905
P7R43174 *	$20^h17^m41^s$	$-16^\circ16'06''$	27.3	-26.2	50	820	3FGL J2017.6−1616
24M2527.1	$20^h17^m57^s$	$+36^\circ27'37''$	74.5	0.4	5	820	3FGL J2017.9+3627
P7R43179	$20^h21^m56^s$	$+06^\circ30'09''$	49.6	-16.8	50	350	3FGL J2021.9+0630
P7R43195	$20^h26^m20^s$	$+14^\circ30'51''$	57.3	-13.4	50	350	3FGL J2026.3+1430
1FGL J2027.6+3335	$20^h28^m18^s$	$+33^\circ32'52''$	73.4	-3.0	5	820	None
1FGL J2027.6+3335	$20^h28^m19^s$	$+33^\circ32'52''$	73.4	-3.0	45	820	None
P7R43197G *	$20^h28^m32^s$	$+40^\circ40'37''$	79.2	1.1	34	820	3FGL J2028.5+4040c
1FGL J2030.9+4411	$20^h30^m54^s$	$+44^\circ16'08''$	82.4	2.9	5	820	None
P72Y3322	$20^h33^m54^s$	$+63^\circ10'35''$	98.2	13.5	40	820	3FGL J2033.6+6309
1FGL J2034.7+3639	$20^h34^m56^s$	$+36^\circ32'40''$	76.6	-2.3	45	820	None
1FGL J2034.7+3639	$20^h34^m56^s$	$+36^\circ32'40''$	76.6	-2.3	5	820	None
P7R43222	$20^h36^m25^s$	$+65^\circ51'25''$	100.6	14.8	45	820	3FGL J2036.4+6551
2FGL J2041.2+4735	$20^h41^m17^s$	$+47^\circ35'39''$	86.1	3.4	5	820	3FGL J2041.1+4736
24M2586 †	$20^h42^m19^s$	$+02^\circ49'46''$	49.1	-23.0	5	820	3FGL J2042.1+0247
2FGL J2046.0+4954	$20^h46^m05^s$	$+49^\circ54'45''$	88.4	4.2	35	350	3FGL J2045.2+5026e
1FGL J2047.6+1055	$20^h47^m04^s$	$+10^\circ55'26''$	57.1	-19.6	5	820	None
24M2616	$20^h52^m52^s$	$+31^\circ44'24''$	75.1	-8.2	5	820	None
1FGL J2055.2+3144	$20^h55^m30^s$	$+31^\circ38'02''$	75.4	-8.7	5	820	None
1FGL J2055.2+3144	$20^h55^m30^s$	$+31^\circ38'03''$	75.4	-8.7	45	820	None
1FGL J2055.2+3144	$20^h55^m30^s$	$+31^\circ38'03''$	75.4	-8.7	5	820	None
SEED_09-262	$20^h56^m19^s$	$+31^\circ41'44''$	75.5	-8.8	50	820	None
1FGL J2057.4+3057	$20^h56^m49^s$	$+30^\circ52'43''$	74.9	-9.4	45	820	None
1FGL J2057.4+3057	$20^h56^m49^s$	$+30^\circ52'43''$	74.9	-9.4	5	820	None
P7R43290 *	$21^h03^m46^s$	$-11^\circ13'44''$	37.9	-34.4	50	820	3FGL J2103.7−1113
2FGL J2107.9+5207c	$21^h07^m56^s$	$+52^\circ07'08''$	92.3	3.1	50	820	3FGL J2108.1+5202
P7R43304	$21^h08^m05^s$	$+52^\circ01'48''$	92.3	3.0	35	820	3FGL J2108.1+5202
2FGL J2112.5−3042	$21^h12^m35^s$	$-30^\circ42'37''$	14.9	-42.4	5	820	3FGL J2112.5−3044
1FGL J2112.5−3044	$21^h12^m36^s$	$-30^\circ42'33''$	14.9	-42.4	5	820	None
P7R43324 *	$21^h14^m54^s$	$+54^\circ48'56''$	95.0	4.1	50	820	3FGL J2114.9+5448
1FGL J2116.8+3729	$21^h17^m19^s$	$+37^\circ27'21''$	82.8	-8.2	5	820	None
2FGL J2117.5+3730	$21^h17^m30^s$	$+37^\circ30'43''$	82.8	-8.2	29	350	3FGL J2117.6+3725
2FGL J2117.5+3730	$21^h17^m32^s$	$+37^\circ30'51''$	82.8	-8.2	5	820	3FGL J2117.6+3725

Table 5.6—Continued

Source	R.A. J2000.0	Decl. J2000.0	l deg	b deg	Integration Time minutes	Observing Freq MHz	3FGL name
2FGL J2117.5+3730	$21^h17^m32^s$	$+37^\circ30'52''$	82.8	-8.2	35	350	3FGL J2117.6+3725
2FGL J2128.7+5824	$21^h28^m42^s$	$+58^\circ24'21''$	98.9	5.3	30	350	None
SEED3Y-1251	$21^h31^m07^s$	$-27^\circ41'45''$	20.1	-45.9	50	820	3FGL J2130.8−2745
1FGL J2139.9+4715	$21^h39^m53^s$	$+47^\circ13'29''$	92.6	-4.0	45	820	None
1FGL J2139.9+4715	$21^h39^m53^s$	$+47^\circ13'29''$	92.6	-4.0	5	820	None
P72Y3547	$21^h52^m33^s$	$+41^\circ53'11''$	90.8	-9.6	50	820	3FGL J2151.6+4154
P72Y3580	$22^h12^m33^s$	$+28^\circ00'06''$	85.1	-23.0	50	820	3FGL J2212.6+2801
P7R43453 *	$22^h12^m35^s$	$+07^\circ03'35''$	68.7	-38.6	45	350	3FGL J2212.5+0703
2FGL J2212.6+0702	$22^h12^m37^s$	$+07^\circ02'53''$	68.7	-38.6	50	820	3FGL J2212.5+0703
2FGL J2221.0+6307	$22^h21^m02^s$	$+63^\circ08'03''$	106.9	5.1	27	350	3FGL J2221.7+6318
2FGL J2221.0+6307	$22^h21^m03^s$	$+63^\circ07'54''$	106.9	5.1	50	820	3FGL J2221.7+6318
2FGL J2227.8+0051	$22^h27^m51^s$	$+63^\circ07'54''$	107.5	4.6	46	820	3FGL J2227.8+0040
P7R43479	$22^h28^m35^s$	$-16^\circ36'06''$	43.1	-55.4	45	350	3FGL J2228.5−1636
P72Y3668	$22^h50^m10^s$	$+33^\circ06'01''$	95.5	-23.2	40	350	3FGL J2250.6+3308
P72Y3672	$22^h50^m26^s$	$+17^\circ50'42''$	86.4	-36.3	44	820	3FGL J2250.3+1747
1FGL J2256.9−1024	$22^h56^m52^s$	$-10^\circ22'46''$	59.3	-58.3	5	820	None
P72Y3714 †	$23^h10^m20^s$	$-05^\circ46'29''$	70.0	-57.8	40	350	3FGL J2310.1−0557
P72Y3714_0	$23^h10^m20^s$	$-05^\circ46'30''$	70.0	-57.8	10	820	3FGL J2310.1−0557
P72Y3714_0	$23^h10^m20^s$	$-05^\circ46'30''$	70.0	-57.8	10	820	3FGL J2310.1−0557
1FGL J2339.7−0531	$23^h39^m42^s$	$-05^\circ31'17''$	81.4	-62.5	32	820	None
1FGL J2339.7−0531	$23^h39^m42^s$	$-05^\circ31'17''$	81.4	-62.5	5	820	None
1FGL J2339.7−0531	$23^h39^m42^s$	$-05^\circ31'17''$	81.4	-62.5	5	820	None
P72Y3794	$23^h45^m10^s$	$-15^\circ55'16''$	65.6	-71.0	45	820	3FGL J2345.2−1554

Table 5.7. Radio Searches of *Fermi* Unassociated Sources near the Galactic Plane

Source	R.A. J2000.0	Decl. J2000.0	l deg	b deg	Integration Time minutes	Observing Freq MHz	3FGL name
P72Y0008	$00^h02^m40^s$	$+62^\circ16'44''$	117.3	-0.1	27	2000	3FGL J0002.6+6218
P72Y0106_0	$00^h38^m51^s$	$+63^\circ00'32''$	121.5	0.2	8	2000	3FGL J0039.3+6256
P72Y0348	$02^h23^m53^s$	$+62^\circ04'59''$	133.5	1.1	26	2000	3FGL J0223.6+6204
2FGL J0224.0+6204	$02^h24^m05^s$	$+62^\circ04'35''$	133.5	1.1	59	2000	3FGL J0223.6+6204
P72Y0352_0	$02^h26^m03^s$	$+61^\circ55'48''$	133.8	1.1	10	2000	None
2FGL J0359.5+5410	$03^h59^m33^s$	$+54^\circ10'49''$	148.3	0.8	32	2000	3FGL J0359.5+5413
P72Y0624_0	$04^h27^m07^s$	$+54^\circ36'58''$	150.9	3.9	8	2000	3FGL J0426.7+5437
P72Y0896_0	$06^h08^m18^s$	$+20^\circ37'07''$	189.8	0.3	7	2000	3FGL J0609.2+2051c
P72Y1310	$09^h01^m36^s$	$+54^\circ12'57''$	163.4	40.5	53	2000	None
P72Y2550_0	$16^h36^m10^s$	$+54^\circ12'56''$	82.7	41.3	7	2000	None
P72Y2604	$16^h53^m35^s$	$-01^\circ59'24''$	16.6	24.9	50	2000	3FGL J1653.6−0158
J1803.1-2147c	$18^h03^m11^s$	$-21^\circ47'27''$	8.2	0.2	67	2000	3FGL J1803.1−2147
P72Y2994	$18^h39^m15^s$	$-05^\circ56'46''$	26.3	-0.0	40	2000	3FGL J1838.9−0537
2FGL J1844.3−0343c	$18^h44^m23^s$	$-03^\circ43'54''$	28.8	-0.1	21	2000	3FGL J1844.3−0344
2FGL J1857.2+0055c	$18^h57^m14^s$	$-03^\circ43'54''$	30.3	-3.0	27	2000	3FGL J1857.2+0059
P72Y3053	$18^h57^m41^s$	$+02^\circ12'45''$	35.6	-0.4	43	2000	3FGL J1857.9+0210
2FGL J1906.5+0720	$19^h06^m35^s$	$+07^\circ20'33''$	41.2	-0.0	27	2000	3FGL J1906.6+0720
P72Y3081_0	$19^h06^m38^s$	$+07^\circ19'19''$	41.2	-0.0	7	2000	3FGL J1906.6+0720
2FGL J2034.9+3632	$20^h34^m57^s$	$+36^\circ32'04''$	76.6	-2.3	23	2000	3FGL J2035.0+3634
P72Y3325_0	$20^h35^m00^s$	$+36^\circ33'37''$	76.6	-2.3	7	2000	3FGL J2035.0+3634

Table 5.8. Best-fit Parameters for the MSPs J1513-2550, J2017-1614, and J2115+5448 with ELL1 binary model

Parameter	PSR J1513-2550	PSR J2017-1614	PSR J2115+5448
Right Ascension (RA, J2000)	$15^{h}\ 13^{m}\ 23\overset{s}{.}32059(6)$	$20^{h}\ 17^{m}\ 46\overset{s}{.}1478(8)$	$21^{h}\ 15^{m}\ 11\overset{s}{.}7678(1)$
Declination (DEC, J2000)	$-25^{\circ}\ 50'\ 31\overset{''}{.}285(3)$	$-16^{\circ}\ 14'\ 15\overset{''}{.}51(5)$	$54^{\circ}\ 48'\ 45\overset{''}{.}154(2)$
Galactic Longitude, l (°)	338.82	27.31	95.04
Galactic Latitude, b (°)	26.96	-26.22	4.11
Spin Period (ms)	2.1190675651177(1)	2.3142872649224(4)	2.602876738872(2)
Period Derivative, $\dot{P}_{obs}$ (10^{-21})	21.61(2)	2.45(5)	74.9(1)
Reference Epoch (MJD)	56989.781	57024.0	56761.16
Dispersion Measure ($pc\,cm^{-3}$)	46.86(7)	25.4380(4)	77.4059(2)
Flux Density at 820 MHz (mJy)	2.3(3)	0.27(8)	1.2(4)
Binary Model	ELL1	ELL1	ELL1
Projected Semi-Major Axis (lt-s)	0.0408132(7)	0.043655(5)	0.044846(1)
Orbital Period, P_b (days)	0.1786354505(8)	0.0978252578(4)	0.135322188(3)
Orbital Period Derivative, $\dot{P}_b$ (10^{-12}) ...	...	...	$6(2)\times10^{1}$
Epoch of Ascending Node (MJD)	56728.4539340(6)	56704.756314(2)	56725.6077844(6)
$\epsilon_1, e\cos(\omega)(10^{-6})$	∼154.2	∼840.1	∼244.7
Span of Timing Data (MJD)	56728 – 57251	56704 – 57342	56704 – 57251
Number of radio TOAs	232	72	97
RMS radio TOA Residual (μs)	4.02	16.99	9.58
Derived Parameters			
Galactic potential effect, $\dot{P}_{gal}$ (10^{-21}) ...	0.5(1)	0.26(6)	1.3(5)
Intrinsic Period Derivative, $\dot{P}_{int}$ (10^{-21}) *	21.1(1)	2.18(8)	73.6(5)
Mass Function ($M_{\odot}$)	$2.2874(1)\times10^{-6}$	$9.334(3)\times10^{-6}$	$5.2882(4)\times10^{-6}$
Minimum Companion Mass ($M_{\odot}$)	≥0.02	≥0.03	≥0.02
DM-derived Distance (kpc)	2.0	1.1	3.4
Surface Magnetic Field (10^{8} G)	2.1	0.7	4.4
Characteristic Age (Gyr)	1.6	16.8	0.6
Spin-down Luminosity, $\dot{E}$ (10^{34} ergs s^{-1})	8.77	0.7	16.48

Table 5.8—Continued

Parameter	PSR J1513-2550	PSR J2017-1614	PSR J2115+5448
γ-ray Spectral Fit Parameters			
Fermi 5-Year Source (3FGL)	3FGL J1513.4-2549	3FGL J2017.6-1616	3FGL J2114.9+5448

$^{*}\dot{P}_{int} = \dot{P}_{obs} - \dot{P}_{shk} - \dot{P}_{gal}$ when $\dot{P}_{shk}$ is available

Note. — Numbers in parentheses represent 1-σ uncertainties in the last digit for the timing parameters. Minimum companion masses were calculated assuming a pulsar mass of $1.4\,M_{\odot}$. The DM-distances were derived according to the NE2001 Galactic electron density model (Cordes & Lazio 2002) and likely have $\sim$20% uncertainties. The contribution in period derivative from the Shklovskii effect are included for the pulsar with significant measurement of proper motion.

Table 5.9. Best-fit Parameters for the MSP J1622-0315 with BTX binary model

Parameter	PSR J1622-0315
Right Ascension (RA, J2000)	$16^{\rm h}\ 22^{\rm m}\ 59\overset{\rm s}{.}6285(3)$
Declination (DEC, J2000)	$-03^\circ\ 15'\ 37\overset{''}{.}328(7)$
Galactic Longitude, l (°)	10.71
Galactic Latitude, b (°)	30.68
Spin Period (ms)	3.845429067931(3)
Period Derivative, $\dot{P}_{obs}$ (10^{-21})	11.6(1)
Reference Epoch (MJD)	56769.0
Dispersion Measure ($pc\,cm^{-3}$)	21.4
Flux Density at 820 MHz (mJy)	1(2)
Binary Model	BTX
Projected Semi-Major Axis (lt-s)	0.219258(5)
Orbital Period, P_b (days)	0.1617006798(6)
Orbital Period Derivative, $\dot{P}_b$ (10^{-12})	-4.1(2)$\times10^{-9}$
Orbital Frequency, F_b (Hz)	7.15771516(3)$\times10^{-5}$
Orbital Frequency Derivative, $\dot{F}_b$ (Hz s^{-1})	1.57(7)$\times10^{-19}$
Epoch of Periastron (MJD)	56733.668703(1)
Span of Timing Data (MJD)	56733 – 57549
Number of radio TOAs	268
RMS radio TOA Residual (μs)	17.21
Derived Parameters	
Proper Motion in RA (mas yr^{-1})	-15.4(1.7)
Proper Motion in DEC (mas yr^{-1})	37.5(5.1)
Transverse velocity, V_T (km s^{-1})	2.1(5)$\times10^2$
Shklovskii effect, $\dot{P}_{shk}$ (10^{-21})	17(5)
Galactic potential effect, $\dot{P}_{gal}$ (10^{-21})	0.4(1)
Intrinsic Period Derivative, $\dot{P}_{int}$ (10^{-21}) *.	11.1(1)
Mass Function ($M_\odot$)	0.00043284(3)
Minimum Companion Mass ($M_\odot$)	$\geq$0.1
DM-derived Distance (kpc)	1.1
Surface Magnetic Field (10^8 G)	2.1
Characteristic Age (Gyr)	5.5

Table 5.9—Continued

Parameter	PSR J1622-0315
Spin-down Luminosity, $\dot{E}$ ($10^{34}\,\mathrm{ergs\,s^{-1}}$)	0.77
γ-ray Spectral Fit Parameters	
Fermi 5-Year Source (3FGL).....	3FGL J1622.9-0312

$^{*}\dot{P}_{int} = \dot{P}_{obs} - \dot{P}_{shk} - \dot{P}_{gal}$ when $\dot{P}_{shk}$ is available

Note. — Numbers in parentheses represent 1-σ uncertainties in the last digit for the timing parameters. Minimum companion masses were calculated assuming a pulsar mass of $1.4\,M_{\odot}$. The DM-distances were derived according to the NE2001 Galactic electron density model (Cordes & Lazio 2002) and likely have $\sim$20% uncertainties. The contribution in period derivative from the Shklovskii effect are included for the pulsar with significant measurement of proper motion.

References

Abbott, B. P., Abbott, R., Abbott, T. D., Abernathy, M. R., Acernese, F., Ackley, K., Adams, C., Adams, T., Addesso, P., Adhikari, R. X., & et al. 2016a, Physical Review Letters, 116, 241103

—. 2016b, Physical Review Letters, 116, 061102

Abdo, A. A., Ackermann, M., Ajello, M., Allafort, A., Antolini, E., Atwood, W. B., Axelsson, M., Baldini, L., Ballet, J., Barbiellini, G., & et al. 2010a, ApJS, 188, 405

Abdo, A. A., Ackermann, M., Ajello, M., Anderson, B., Atwood, W. B., Axelsson, M., Baldini, L., Ballet, J., Barbiellini, G., Baring, M. G., Bastieri, D., Baughman, B. M., Bechtol, K., Bellazzini, R., Berenji, B., Bignami, G. F., Blandford, R. D., Bloom, E. D., Bonamente, E., Borgland, A. W., Bregeon, J., Brez, A., Brigida, M., Bruel, P., Burnett, T. H., Caliandro, G. A., Cameron, R. A., Caraveo, P. A., Casandjian, J. M., Cecchi, C., Çelik, Ö., Chekhtman, A., Cheung, C. C., Chiang, J., Ciprini, S., Claus, R., Cohen-Tanugi, J., Conrad, J., Cutini, S., Dermer, C. D., de Angelis, A., de Luca, A., de Palma, F., Digel, S. W., Dormody, M., do Couto e Silva, E., Drell, P. S., Dubois, R., Dumora, D., Farnier, C., Favuzzi, C., Fegan, S. J., Fukazawa, Y., Funk, S., Fusco, P., Gargano, F., Gasparrini, D., Gehrels, N., Germani, S., Giebels, B., Giglietto, N., Giommi, P., Giordano, F., Glanzman, T., Godfrey, G., Grenier, I. A., Grondin, M.-H., Grove, J. E., Guillemot, L., Guiriec,

S., Gwon, C., Hanabata, Y., Harding, A. K., Hayashida, M., Hays, E., Hughes, R. E., Jóhannesson, G., Johnson, R. P., Johnson, T. J., Johnson, W. N., Kamae, T., Katagiri, H., Kataoka, J., Kawai, N., Kerr, M., Knödlseder, J., Kocian, M. L., Kuss, M., Lande, J., Latronico, L., Lemoine-Goumard, M., Longo, F., Loparco, F., Lott, B., Lovellette, M. N., Lubrano, P., Madejski, G. M., Makeev, A., Marelli, M., Mazziotta, M. N., McConville, W., McEnery, J. E., Meurer, C., Michelson, P. F., Mitthumsiri, W., Mizuno, T., Monte, C., Monzani, M. E., Morselli, A., Moskalenko, I. V., Murgia, S., Nolan, P. L., Norris, J. P., Nuss, E., Ohsugi, T., Omodei, N., Orlando, E., Ormes, J. F., Paneque, D., Parent, D., Pelassa, V., Pepe, M., Pesce-Rollins, M., Pierbattista, M., Piron, F., Porter, T. A., Primack, J. R., Rainò, S., Rando, R., Ray, P. S., Razzano, M., Rea, N., Reimer, A., Reimer, O., Reposeur, T., Ritz, S., Rochester, L. S., Rodriguez, A. Y., Romani, R. W., Ryde, F., Sadrozinski, H. F.-W., Sanchez, D., Sander, A., Parkinson, P. M. S., Scargle, J. D., Sgrò, C., Siskind, E. J., Smith, D. A., Smith, P. D., Spandre, G., Spinelli, P., Starck, J.-L., Strickman, M. S., Suson, D. J., Tajima, H., Takahashi, H., Takahashi, T., Tanaka, T., Thayer, J. G., Thompson, D. J., Tibaldo, L., Tibolla, O., Torres, D. F., Tosti, G., Tramacere, A., Uchiyama, Y., Usher, T. L., Van Etten, A., Vasileiou, V., Vilchez, N., Vitale, V., Waite, A. P., Wang, P., Watters, K., Winer, B. L., Wolff, M. T., Wood, K. S., Ylinen, T., Ziegler, M., & Fermi LAT Collaboration. 2009a, Science, 325, 840

Abdo, A. A., Ackermann, M., Ajello, M., Atwood, W. B., Axelsson, M., Baldini, L., Ballet, J., Band, D. L., Barbiellini, G., Bastieri, D., & et al. 2009b, ApJS, 183, 46

Abdo, A. A., Ackermann, M., Ajello, M., Atwood, W. B., Axelsson, M., Baldini, L., Ballet, J., Barbiellini, G., Baring, M. G., Bastieri, D., & et al. 2010b, ApJS, 187, 460

Abdo, A. A., Ackermann, M., Atwood, W. B., Baldini, L., Ballet, J., Barbiellini, G., Baring, M. G., Bastieri, D., & others. 2009c, Astroparticle Physics, 32, 193

Abdo, A. A., Ajello, M., Allafort, A., Baldini, L., Ballet, J., Barbiellini, G., Baring, M. G., Bastieri, D., Belfiore, A., Bellazzini, R., & et al. 2013, ApJS, 208, 17

Acero, F., Ackermann, M., Ajello, M., Albert, A., Atwood, W. B., Axelsson, M., Baldini, L., Ballet, J., Barbiellini, G., Bastieri, D., Belfiore, A., Bellazzini, R., Bissaldi, E., Blandford, R. D., Bloom, E. D., Bogart, J. R., Bonino, R., Bottacini, E., Bregeon, J., Britto, R. J., Bruel, P., Buehler, R., Burnett, T. H., Buson, S., Caliandro, G. A., Cameron, R. A., Caputo, R., Caragiulo, M., Caraveo, P. A., Casandjian, J. M., Cavazzuti, E., Charles, E., Chaves, R. C. G., Chekhtman, A., Cheung, C. C., Chiang, J., Chiaro, G., Ciprini, S., Claus, R., Cohen-Tanugi, J., Cominsky, L. R., Conrad, J., Cutini, S., D'Ammando, F., de Angelis, A., DeKlotz, M., de Palma, F., Desiante, R., Digel, S. W., Di Venere, L., Drell, P. S., Dubois, R., Dumora, D., Favuzzi, C., Fegan, S. J., Ferrara, E. C., Finke, J., Franckowiak, A., Fukazawa, Y., Funk, S., Fusco, P., Gargano, F., Gasparrini, D., Giebels, B., Giglietto, N., Giommi, P., Giordano, F., Giroletti, M., Glanzman, T., Godfrey, G., Grenier, I. A., Grondin, M.-H., Grove, J. E., Guillemot, L., Guiriec, S., Hadasch, D., Harding, A. K., Hays, E., Hewitt, J. W., Hill, A. B., Horan, D., Iafrate, G., Jogler, T., Jóhannesson, G., Johnson, R. P., Johnson, A. S., Johnson, T. J., Johnson, W. N., Kamae, T., Kataoka, J., Katsuta, J., Kuss, M., La Mura, G., Landriu, D., Larsson, S., Latronico, L., Lemoine-Goumard, M., Li, J., Li, L., Longo, F., Loparco, F., Lott, B., Lovellette, M. N., Lubrano, P., Madejski, G. M., Massaro, F., Mayer, M., Mazziotta, M. N., McEnery, J. E., Michelson, P. F., Mirabal, N., Mizuno, T., Moiseev, A. A., Mongelli, M., Monzani, M. E., Morselli, A., Moskalenko, I. V., Murgia, S., Nuss, E., Ohno, M., Ohsugi, T., Omodei, N., Orienti, M., Orlando, E.,

Ormes, J. F., Paneque, D., Panetta, J. H., Perkins, J. S., Pesce-Rollins, M., Piron, F., Pivato, G., Porter, T. A., Racusin, J. L., Rando, R., Razzano, M., Razzaque, S., Reimer, A., Reimer, O., Reposeur, T., Rochester, L. S., Romani, R. W., Salvetti, D., Sánchez-Conde, M., Saz Parkinson, P. M., Schulz, A., Siskind, E. J., Smith, D. A., Spada, F., Spandre, G., Spinelli, P., Stephens, T. E., Strong, A. W., Suson, D. J., Takahashi, H., Takahashi, T., Tanaka, Y., Thayer, J. G., Thayer, J. B., Thompson, D. J., Tibaldo, L., Tibolla, O., Torres, D. F., Torresi, E., Tosti, G., Troja, E., Van Klaveren, B., Vianello, G., Winer, B. L., Wood, K. S., Wood, M., Zimmer, S., & Fermi-LAT Collaboration. 2015, ApJS, 218, 23

Ackermann, M., Ajello, M., Albert, A., Allafort, A., Atwood, W. B., Axelsson, M., Baldini, L., et al. 2012, ApJS, 203, 4

Alpar, M. A., Cheng, A. F., Ruderman, M. A., & Shaham, J. 1982, Nature, 300, 728

Archibald, A. M., Bogdanov, S., Patruno, A., Hessels, J. W. T., Deller, A. T., Bassa, C., Janssen, G. H., Kaspi, V. M., Lyne, A. G., Stappers, B. W., Tendulkar, S. P., D'Angelo, C. R., & Wijnands, R. 2015, ApJ, 807, 62

Archibald, A. M., Kaspi, V. M., Bogdanov, S., Hessels, J. W. T., Stairs, I. H., Ransom, S. M., & McLaughlin, M. A. 2010, ApJ, 722, 88

Archibald, A. M., Stairs, I. H., Ransom, S. M., Kaspi, V. M., Kondratiev, V. I., Lorimer, D. R., McLaughlin, M. A., Boyles, J., Hessels, J. W. T., Lynch, R., van Leeuwen, J., Roberts, M. S. E., Jenet, F., Champion, D. J., Rosen, R., Barlow, B. N., Dunlap, B. H., & Remillard, R. A. 2009, Science, 324, 1411

Atwood, W. B., Abdo, A. A., Ackermann, M., Althouse, W., Anderson, B., Axelsson,

M., Baldini, L., Ballet, J., Band, D. L., Barbiellini, G., & et al. 2009, ApJ, 697, 1071

Baade, W. & Zwicky, F. 1934, Proceedings of the National Academy of Science, 20, 259

Barr, E. D., Guillemot, L., Champion, D. J., Kramer, M., Eatough, R. P., Lee, K. J., Verbiest, J. P. W., et al. 2013, MNRAS, 429, 1633

Bates, S. D., Lorimer, D. R., & Verbiest, J. P. W. 2013, MNRAS, 431, 1352

Bellm, E. C., Kaplan, D. L., Breton, R. P., Phinney, E. S., Bhalerao, V. B., Camilo, F., Dahal, S., Djorgovski, S. G., Drake, A. J., Hessels, J. W. T., Laher, R. R., Levitan, D. B., Lewis, F., Mahabal, A. A., Ofek, E. O., Prince, T. A., Ransom, S. M., Roberts, M. S. E., Russell, D. M., Sesar, B., Surace, J. A., & Tang, S. 2016, ApJ, 816, 74

Benvenuto, O. G., De Vito, M. A., & Horvath, J. E. 2015, ApJ, 798, 44

Bhattacharyya, B., Roy, J., Ray, P. S., Gupta, Y., Bhattacharya, D., Romani, R. W., Ransom, S. M., et al. 2013, ApJ, 773, L12

Bochenek, C., Ransom, S., & Demorest, P. 2015, ApJ, 813, L4

Bregeon, J., Charles, E., & M. Wood for the Fermi-LAT collaboration. 2013, in Proceedings of the 4th Fermi Symposium, eConf C121028, (arXiv:1304.5456)

Burke-Spolaor, S., Johnston, S., Bailes, M., Bates, S. D., Bhat, N. D. R., Burgay, M., Champion, D. J., D'Amico, N., Keith, M. J., Kramer, M., Levin, L., Milia, S., Possenti, A., Stappers, B., & van Straten, W. 2012, MNRAS, 423, 1351

Camilo, F., Kerr, M., Ray, P. S., Ransom, S. M., Sarkissian, J., Cromartie, H. T., Johnston, S., Reynolds, J. E., Wolff, M. T., Freire, P. C. C., Bhattacharyya, B., Ferrara, E. C., Keith, M., Michelson, P. F., Saz Parkinson, P. M., & Wood, K. S. 2015, ArXiv e-prints, 1507.04451

Chakrabarty, D. & Morgan, E. H. 1998, Nature, 394, 346

Champion, D. J., McLaughlin, M. A., & Lorimer, D. R. 2005, MNRAS, 364, 1011

Chen, H.-L., Chen, X., Tauris, T. M., & Han, Z. 2013, ApJ, 775, 27

Cheng, K. S., Ho, C., & Ruderman, M. 1986, ApJ, 300, 500

Cognard, I., Guillemot, L., Johnson, T. J., Smith, D. A., Venter, C., Harding, A. K., Wolff, M. T., et al. 2011, ApJ, 732, 47

Cordes, J. M. & Lazio, T. J. W. 2002, ArXiv Astrophysics e-prints, astro-ph/0207156

Crawford, F., Roberts, M. S. E., Hessels, J. W. T., Ransom, S. M., Livingstone, M., Tam, C. R., & Kaspi, V. M. 2006, ApJ, 652, 1499

Cromartie, H. T., Camilo, F., Kerr, M., Deneva, J. S., Ransom, S. M., Ray, P. S., Ferrara, E. C., Michelson, P. F., & Wood, K. S. 2016, ApJ, 819, 34

Damour, T. & Deruelle, N. 1986, Ann. Inst. Henri Poincaré Phys. Théor., Vol. 44, No. 3, p. 263 - 292, 44, 263

Demorest, P. B., Pennucci, T., Ransom, S. M., Roberts, M. S. E., & Hessels, J. W. T. 2010, Nature, 467, 1081

Deneva, J. S., Cordes, J. M., McLaughlin, M. A., Nice, D. J., Lorimer, D. R., Crawford, F., Bhat, N. D. R., et al. 2009, ApJ, 703, 2259

Dubus, G. 2015, Comptes Rendus Physique, 16, 661

DuPlain, R., Ransom, S., Demorest, P., Brandt, P., Ford, J., & Shelton, A. L. 2008, in Society of Photo-Optical Instrumentation Engineers (SPIE) Conference Series, Vol. 7019, Society of Photo-Optical Instrumentation Engineers (SPIE) Conference Series, 1

Foreman-Mackey, D., Hogg, D. W., Lang, D., & Goodman, J. 2013, PASP, 125, 306

Freire, P. C. C., Abdo, A. A., Ajello, M., Allafort, A., Ballet, J., Barbiellini, G., Bastieri, D., et al. 2011, Science, 334, 1107

Fruchter, A. S., Stinebring, D. R., & Taylor, J. H. 1988, Nature, 333, 237

Grenier, I. A. & Harding, A. K. 2015, Comptes Rendus Physique, 16, 641

Guillemot, L., Johnson, T. J., Venter, C., Kerr, M., Pancrazi, B., Livingstone, M., Janssen, G. H., et al. 2012, ApJ, 744, 33

Guillemot, L. & Tauris, T. M. 2014, MNRAS, 439, 2033

Hessels, J. W. T., Ransom, S. M., Stairs, I. H., Kaspi, V. M., & Freire, P. C. C. 2007, ApJ, 670, 363

Hewish, A., Bell, S. J., Pilkington, J. D. H., Scott, P. F., & Collins, R. A. 1968, Nature, 217, 709

Hobbs, G., Archibald, A., Arzoumanian, Z., Backer, D., Bailes, M., Bhat, N. D. R., Burgay, M., Burke-Spolaor, S., Champion, D., Cognard, I., Coles, W., Cordes, J., Demorest, P., Desvignes, G., Ferdman, R. D., Finn, L., Freire, P., Gonzalez, M., Hessels, J., Hotan, A., Janssen, G., Jenet, F., Jessner, A., Jordan, C., Kaspi, V., Kramer, M., Kondratiev, V., Lazio, J., Lazaridis, K., Lee, K. J., Levin, Y.,

Lommen, A., Lorimer, D., Lynch, R., Lyne, A., Manchester, R., McLaughlin, M., Nice, D., Oslowski, S., Pilia, M., Possenti, A., Purver, M., Ransom, S., Reynolds, J., Sanidas, S., Sarkissian, J., Sesana, A., Shannon, R., Siemens, X., Stairs, I., Stappers, B., Stinebring, D., Theureau, G., van Haasteren, R., van Straten, W., Verbiest, J. P. W., Yardley, D. R. B., & You, X. P. 2010, Classical and Quantum Gravity, 27, 084013

Hobbs, G. B., Edwards, R. T., & Manchester, R. N. 2006, MNRAS, 369, 655

Huang, R. H. H., Kong, A. K. H., Takata, J., Hui, C. Y., Lin, L. C. C., & Cheng, K. S. 2012, ApJ, 760, 92

Jacoby, B. A., Hotan, A., Bailes, M., Ord, S., & Kulkarni, S. R. 2005, ApJ, 629, L113

Johnson, T. J., Venter, C., Harding, A. K., Guillemot, L., Smith, D. A., Kramer, M., Çelik, Ö., den Hartog, P. R., Ferrara, E. C., Hou, X., Lande, J., & Ray, P. S. 2014, ApJS, 213, 6

Johnston, S., Manchester, R. N., Lyne, A. G., Bailes, M., Kaspi, V. M., Qiao, G., & D'Amico, N. 1992, ApJ, 387, L37

Johnston, S. & Romani, R. W. 2003, ApJ, 590, L95

Joss, P. C., Rappaport, S., & Lewis, W. 1987, ApJ, 319, 180

Kaplan, D. L., van Kerkwijk, M. H., Koester, D., Stairs, I. H., Ransom, S. M., Archibald, A. M., Hessels, J. W. T., & Boyles, J. 2014, ApJ, 783, L23

Keith, M. J., Johnston, S., Kramer, M., Weltevrede, P., Watters, K. P., & Stappers, B. W. 2008, MNRAS, 389, 1881

Keith, M. J., Johnston, S., Ray, P. S., Ferrara, E. C., Saz Parkinson, P. M., Çelik, Ö., Belfiore, A., et al. 2011, MNRAS, 414, 1292

Kerr, M. 2011, ApJ, 732, 38

Kerr, M., Camilo, F., Johnson, T. J., Ferrara, E. C., Guillemot, L., Harding, A. K., Hessels, J., et al. 2012, ApJ, 748, L2

Knight, H. S. 2006, Chinese Journal of Astronomy and Astrophysics Supplement, 6, 41

Kramer, M., Lange, C., Lorimer, D. R., Backer, D. C., Xilouris, K. M., Jessner, A., & Wielebinski, R. 1999, ApJ, 526, 957

Kramer, M., Stairs, I. H., Manchester, R. N., McLaughlin, M. A., Lyne, A. G., Ferdman, R. D., Burgay, M., Lorimer, D. R., Possenti, A., D'Amico, N., Sarkissian, J. M., Hobbs, G. B., Reynolds, J. E., Freire, P. C. C., & Camilo, F. 2006, Science, 314, 97

Kramer, M., Xilouris, K. M., Lorimer, D. R., Doroshenko, O., Jessner, A., Wielebinski, R., Wolszczan, A., & Camilo, F. 1998, ApJ, 501, 270

Lange, C., Camilo, F., Wex, N., Kramer, M., Backer, D. C., Lyne, A. G., & Doroshenko, O. 2001, MNRAS, 326, 274

Lawson, K. D., Mayer, C. J., Osborne, J. L., & Parkinson, M. L. 1987, MNRAS, 225, 307

Li, M., Halpern, J. P., & Thorstensen, J. R. 2014, ApJ, 795, 115

Lorimer, D. & Kramer, M. 2005, Cambridge Observing Handbooks for Research Astronomers, Vol. 4, Handbook of Pulsar Astronomy, 1st edn. (Cambridge, U.K.; New York, U.S.A: Cambridge University Press)

Lundgren, S. C., Zepka, A. F., & Cordes, J. M. 1995, ApJ, 453, 419

Lynch, R. S. & Bank North Celestial Cap Survey Collaborations. 2013, in IAU Symposium, Vol. 291, Neutron Stars and Pulsars: Challenges and Opportunities after 80 years, ed. J. van Leeuwen, 41–46

Lyutikov, M., Otte, N., & McCann, A. 2012, ApJ, 754, 33

Magro, A., Karastergiou, A., Salvini, S., Mort, B., Dulwich, F., & Zarb Adami, K. 2011, MNRAS, 417, 2642

Manchester, R. N., Hobbs, G. B., Teoh, A., & Hobbs, M. 2005, VizieR Online Data Catalog, 7245, 0

McLaughlin, M. A., Lyne, A. G., Lorimer, D. R., Kramer, M., Faulkner, A. J., Manchester, R. N., Cordes, J. M., Camilo, F., Possenti, A., Stairs, I. H., Hobbs, G., D'Amico, N., Burgay, M., & O'Brien, J. T. 2006, Nature, 439, 817

Muslimov, A. G. & Harding, A. K. 2004, ApJ, 606, 1143

Nolan, P. L., Abdo, A. A., Ackermann, M., Ajello, M., Allafort, A., Antolini, E., Atwood, W. B., Axelsson, M., Baldini, L., Ballet, J., & et al. 2012, ApJS, 199, 31

Özel, F., Psaltis, D., Narayan, R., & Santos Villarreal, A. 2012, ApJ, 757, 55

Papitto, A., Ferrigno, C., Bozzo, E., Rea, N., Pavan, L., Burderi, L., Burgay, M., Campana, S., di Salvo, T., Falanga, M., Filipović, M. D., Freire, P. C. C., Hessels, J. W. T., Possenti, A., Ransom, S. M., Riggio, A., Romano, P., Sarkissian, J. M.,

Stairs, I. H., Stella, L., Torres, D. F., Wieringa, M. H., & Wong, G. F. 2013, Nature, 501, 517

Pétri, J. 2012, in Astronomical Society of the Pacific Conference Series, Vol. 466, Electromagnetic Radiation from Pulsars and Magnetars, ed. W. Lewandowski, O. Maron, & J. Kijak, 21

Pletsch, H. J. & Clark, C. J. 2015, ApJ, 807, 18

Pletsch, H. J., Guillemot, L., Allen, B., Kramer, M., Aulbert, C., Fehrmann, H., Ray, P. S., Barr, E. D., Belfiore, A., Camilo, F., Caraveo, P. A., Çelik, Ö., Champion, D. J., Dormody, M., Eatough, R. P., Ferrara, E. C., Freire, P. C. C., Hessels, J. W. T., Keith, M., Kerr, M., de Luca, A., Lyne, A. G., Marelli, M., McLaughlin, M. A., Parent, D., Ransom, S. M., Razzano, M., Reich, W., Saz Parkinson, P. M., Stappers, B. W., & Wolff, M. T. 2012a, ApJ, 744, 105

Pletsch, H. J., Guillemot, L., Fehrmann, H., Allen, B., Kramer, M., Aulbert, C., Ackermann, M., Ajello, M., de Angelis, A., Atwood, W. B., Baldini, L., Ballet, J., Barbiellini, G., Bastieri, D., Bechtol, K., Bellazzini, R., Borgland, A. W., Bottacini, E., Brandt, T. J., Bregeon, J., Brigida, M., Bruel, P., Buehler, R., Buson, S., Caliandro, G. A., Cameron, R. A., Caraveo, P. A., Casandjian, J. M., Cecchi, C., Çelik, Ö., Charles, E., Chaves, R. C. G., Cheung, C. C., Chiang, J., Ciprini, S., Claus, R., Cohen-Tanugi, J., Conrad, J., Cutini, S., D'Ammando, F., Dermer, C. D., Digel, S. W., Drell, P. S., Drlica-Wagner, A., Dubois, R., Dumora, D., Favuzzi, C., Ferrara, E. C., Franckowiak, A., Fukazawa, Y., Fusco, P., Gargano, F., Gehrels, N., Germani, S., Giglietto, N., Giordano, F., Giroletti, M., Godfrey, G., Grenier, I. A., Grondin, M.-H., Grove, J. E., Guiriec, S., Hadasch, D., Hanabata, Y., Harding, A. K., den Hartog, P. R., Hayashida, M., Hays, E., Hill, A. B., Hou, X., Hughes,

R. E., Jóhannesson, G., Jackson, M. S., Jogler, T., Johnson, A. S., Johnson, W. N., Kataoka, J., Kerr, M., Knödlseder, J., Kuss, M., Lande, J., Larsson, S., Latronico, L., Lemoine-Goumard, M., Longo, F., Loparco, F., Lovellette, M. N., Lubrano, P., Massaro, F., Mayer, M., Mazziotta, M. N., McEnery, J. E., Mehault, J., Michelson, P. F., Mitthumsiri, W., Mizuno, T., Monzani, M. E., Morselli, A., Moskalenko, I. V., Murgia, S., Nakamori, T., Nemmen, R., Nuss, E., Ohno, M., Ohsugi, T., Omodei, N., Orienti, M., Orlando, E., de Palma, F., Paneque, D., Perkins, J. S., Piron, F., Pivato, G., Porter, T. A., Rainò, S., Rando, R., Ray, P. S., Razzano, M., Reimer, A., Reimer, O., Reposeur, T., Ritz, S., Romani, R. W., Romoli, C., Sanchez, D. A., Parkinson, P. M. S., Schulz, A., Sgrò, C., do Couto e Silva, E., Siskind, E. J., Smith, D. A., Spandre, G., Spinelli, P., Suson, D. J., Takahashi, H., Tanaka, T., Thayer, J. B., Thayer, J. G., Thompson, D. J., Tibaldo, L., Tinivella, M., Troja, E., Usher, T. L., Vandenbroucke, J., Vasileiou, V., Vianello, G., Vitale, V., Waite, A. P., Winer, B. L., Wood, K. S., Wood, M., Yang, Z., & Zimmer, S. 2012b, Science, 338, 1314

Ransom, S. M. 2001, PhD thesis, Harvard University

Ransom, S. M., Eikenberry, S. S., & Middleditch, J. 2002, AJ, 124, 1788

Ransom, S. M., Greenhill, L. J., Herrnstein, J. R., Manchester, R. N., Camilo, F., Eikenberry, S. S., & Lyne, A. G. 2001, ApJ, 546, L25

Ransom, S. M., Hessels, J. W. T., Stairs, I. H., Freire, P. C. C., Camilo, F., Kaspi, V. M., & Kaplan, D. L. 2005, Science, 307, 892

Ransom, S. M., Ray, P. S., Camilo, F., Roberts, M. S. E., Çelik, Ö., Wolff, M. T., Cheung, C. C., et al. 2011, ApJ, 727, L16

Ransom, S. M., Stairs, I. H., Archibald, A. M., Hessels, J. W. T., Kaplan, D. L., van Kerkwijk, M. H., Boyles, J., Deller, A. T., Chatterjee, S., Schechtman-Rook, A., Berndsen, A., Lynch, R. S., Lorimer, D. R., Karako-Argaman, C., Kaspi, V. M., Kondratiev, V. I., McLaughlin, M. A., van Leeuwen, J., Rosen, R., Roberts, M. S. E., & Stovall, K. 2014, Nature, 505, 520

Rappaport, S., Podsiadlowski, P., Joss, P. C., Di Stefano, R., & Han, Z. 1995, MNRAS, 273, 731

Ray, P. S., Abdo, A. A., Parent, D., Bhattacharya, D., Bhattacharyya, B., Camilo, F., Cognard, I., et al. 2012, ArXiv e-prints, 1205.3089

Ray, P. S., Kerr, M., Parent, D., Abdo, A. A., Guillemot, L., Ransom, S. M., Rea, N., et al. 2011, ApJS, 194, 17

Reid, M. J., Menten, K. M., Zheng, X. W., Brunthaler, A., Moscadelli, L., Xu, Y., Zhang, B., Sato, M., Honma, M., Hirota, T., Hachisuka, K., Choi, Y. K., Moellenbrock, G. A., & Bartkiewicz, A. 2009, ApJ, 700, 137

Roberts, M. S. E. 2002, ArXiv Astrophysics e-prints, astro-ph/0212080

Roberts, M. S. E. 2013, in IAU Symposium, Vol. 291, IAU Symposium, ed. J. van Leeuwen, 127–132

Roberts, M. S. E., McLaughlin, M. A., Gentile, P. A., Ray, P. S., Ransom, S. M., & Hessels, J. W. T. 2015, ArXiv e-prints, 1502.07208

Saz Parkinson, P. M., Dormody, M., Ziegler, M., Ray, P. S., Abdo, A. A., Ballet, J., Baring, M. G., Belfiore, A., Burnett, T. H., Caliandro, G. A., Camilo, F., Caraveo, P. A., de Luca, A., Ferrara, E. C., Freire, P. C. C., Grove, J. E., Gwon,

C., Harding, A. K., Johnson, R. P., Johnson, T. J., Johnston, S., Keith, M., Kerr, M., Knödlseder, J., Makeev, A., Marelli, M., Michelson, P. F., Parent, D., Ransom, S. M., Reimer, O., Romani, R. W., Smith, D. A., Thompson, D. J., Watters, K., Weltevrede, P., Wolff, M. T., & Wood, K. S. 2010, ApJ, 725, 571

Shklovskii, I. S. 1970, Soviet Ast., 13, 562

Smedley, S. L., Tout, C. A., Ferrario, L., & Wickramasinghe, D. T. 2014, MNRAS, 437, 2217

Stairs, I. H., Faulkner, A. J., Lyne, A. G., Kramer, M., Lorimer, D. R., McLaughlin, M. A., Manchester, R. N., Hobbs, G. B., Camilo, F., Possenti, A., Burgay, M., D'Amico, N., Freire, P. C., & Gregory, P. C. 2005, ApJ, 632, 1060

Stappers, B. W., Archibald, A. M., Hessels, J. W. T., Bassa, C. G., Bogdanov, S., Janssen, G. H., Kaspi, V. M., Lyne, A. G., Patruno, A., Tendulkar, S., Hill, A. B., & Glanzman, T. 2014, ApJ, 790, 39

Stappers, B. W., Bailes, M., Lyne, A. G., Manchester, R. N., D'Amico, N., Tauris, T. M., Lorimer, D. R., Johnston, S., & Sandhu, J. S. 1996, ApJ, 465, L119

Tauris, T. M. & Savonije, G. J. 1999, A&A, 350, 928

Tauris, T. M. & van den Heuvel, E. P. J. 2014, ApJ, 781, L13

The NANOGrav Collaboration, Arzoumanian, Z., Brazier, A., Burke-Spolaor, S., Chamberlin, S., Chatterjee, S., Christy, B., Cordes, J. M., Cornish, N., Crowter, K., Demorest, P. B., Dolch, T., Ellis, J. A., Ferdman, R. D., Fonseca, E., Garver-Daniels, N., Gonzalez, M. E., Jenet, F. A., Jones, G., Jones, M. L., Kaspi, V. M., Koop, M., Lam, M. T., Lazio, T. J. W., Levin, L., Lommen, A. N., Lorimer, D. R.,

Luo, J., Lynch, R. S., Madison, D., McLaughlin, M. A., McWilliams, S. T., Nice, D. J., Palliyaguru, N., Pennucci, T. T., Ransom, S. M., Siemens, X., Stairs, I. H., Stinebring, D. R., Stovall, K., Swiggum, J. K., Vallisneri, M., van Haasteren, R., Wang, Y., & Zhu, W. 2015, ApJ, 813, 65

Thompson, C., Blandford, R., Evans, C., & Phinney, E. 1994, The Astrophysical Journal, 422, 304

Thompson, D. J. 2008, Reports on Progress in Physics, 71, 116901

van Kerkwijk, M. H., Bassa, C. G., Jacoby, B. A., & Jonker, P. G. 2005, in Astronomical Society of the Pacific Conference Series, Vol. 328, Binary Radio Pulsars, ed. F. A. Rasio & I. H. Stairs, 357

Venter, C., Harding, A. K., & Guillemot, L. 2009, ApJ, 707, 800

Venter, C., Johnson, T. J., & Harding, A. K. 2012, ApJ, 744, 34

Verbiest, J. P. W., Bailes, M., van Straten, W., Hobbs, G. B., Edwards, R. T., Manchester, R. N., Bhat, N. D. R., et al. 2008, ApJ, 679, 675

Viganò, D., Torres, D. F., Hirotani, K., & Pessah, M. E. 2015, MNRAS, 447, 2649

Webbink, R. F., Rappaport, S., & Savonije, G. J. 1983, ApJ, 270, 678

Weisberg, J. M. & Taylor, J. H. 2005, in Astronomical Society of the Pacific Conference Series, Vol. 328, Binary Radio Pulsars, ed. F. A. Rasio & I. H. Stairs, 25

Wolszczan, A. & Frail, D. A. 1992, Nature, 355, 145

Xing, Y. & Wang, Z. 2015, ApJ, 804, L33